Inter/intra Molecular Dynamics in Gases and Liquids Studied by Terahertz Time-domain Spectroscopy

By

Xuying Xin

A dissertation submitted to the Graduate Faculty in Engineering in partial fulfillment of the requirements for the degree of Doctor of Philosophy,
The City University of New York
2007

UMI Number: 3245076

ProQuest Information and Learning Company
300 North Zeeb Road
P.O. Box 1346
Ann Arbor, MI 48106-1346

This manuscript has been read and accepted for the Graduate Faculty in Engineering in satisfaction of the dissertation requirement for the degree of Doctor of Philosophy

Professor Robert R. Alfano

_____ _____

Date Chair of Examining Committee

Professor Mumtaz K. Kassir

_____ _____

Date Executive Officer

Supervisory Committee:

Professor Anshel Gorokhovsky -Physics Department in College of Staten Island

Professor Roger Dorsinville -Electrical Engineering Department in the City College

Professor Ping-Pei Ho -Electrical Engineering Department in the City College

Professor Swapan Gayen -Physics Department in the City College

Professor Vladimir Petricevic -Physics Department in the City College

Dr. Hakan Altan -The Institute for Ultrafast Spectroscopy and Lasers-IUSL, the City College

THE CITY UNIVERSITY OF NEW YORK

Abstract

Inter/intra Molecular Dynamics in Gases and Liquids Studied by Terahertz Time-domain Spectroscopy

by

Xuying Xin

Advisor: Professor Robert R. Alfano

This thesis presents a description of the low-frequency terahertz (THz) absorption spectrum of a variety of materials that are of interest to many biological and chemical processes. The work described here encompasses the development of time-domain THz spectrometers, based on amplified Ti: Sapphire lasers systems as well as mode-locked Erbium doped fiber lasers as the driving source. These systems were applied to characterize the absorption spectrum of liquid water and water vapor, heavy water vapor, methanol vapor and tryptophan in the 0.2-2.2THz frequency range. The absorption profiles observed are closely related to the intermolecular or intramolecular motions in the materials of interest. In liquid water, the absorption profile shows evidence for modes due to large-scale structure amongst individual water molecules. The effects on the overall absorption profile are further deduced by the addition of various solutes which can enhance or break the formation of molecule networks. Various solutions are examined such as KCl in liquid water. Ions can change the strength of hydrogen bond in liquid water in the similar way as temperature does. Both K^+ and Cl^- are considered to be strong "structure breakers" in terms of their functions

as softening the strength of hydrogen bond in liquid water. Theoretically, this will cause a red shift of some mode frequencies, reducing the absorption intensity at those frequencies and, at the same time, increasing the absorption at non-mode frequencies toward the vicinity of the low frequencies. For liquid water, the vapor phase was also examined, where for varying concentrations (humidity) Beer's Law does not hold to explain the observed absorption profiles. Again the reduced absorption of certain modes is explained by interactions between water monomers and their nature due to hydrogen spins. There are two species of water molecules in terms of the nuclear spin effect of hydrogen atoms in water molecule, *ortho*-water and *para*-water. The two types of water molecules present significantly different properties, e.g. different surface adsorption on metals. The effects of *para*-water and *ortho*-water on the THz absorption profile are discussed. Finally, I discuss the absorption profile of methanol vapor and tryptophan. In methanol vapor we observe coherent echoes after absorption by a THz transient and attribute it to the relaxation of the molecule due to the regularly spaced rotational manifold. In tryptophan two distinct absorption modes are observed due to torsional modes. These "soft-modes" are calculated and attributed to intra-molecular motions between various atoms. The results of this body of work are discussed in the context of applications ranging from medicine, pharmaceuticals and the cosmetics industries.

Acknowledgements

A journey is easier when you travel together. Interdependence is certainly more valuable than independence. This thesis is the result of four and half years of work whereby I have been accompanied and supported by many people. It is a pleasant aspect that I have now the opportunity to express my gratitude for all of them.

The first person I would like to thank is my direct supervisor Professor Robert R. Alfano, I am grateful to him for introducing me to THz-spectroscopy and his academic guidance on my study in this area during the past four years. I have been in his group since 2002 when I started my Ph.D. study. During these years I have known Robert R. Alfano as a sympathetic and principle-centered person. After entering the Ph.D. program I have been part of a cheerful and scientifically inspiring group headed by Professor Alfano, to whom it is important to create the possibility for his students to work independently; his overly enthusiasm and integral view on research has made a deep impression on me. I always benefit from what I have learned from him during my study in IUSL.

I would like to give special thanks to Dr. Hakan Altan who guided me through my thesis studies.

Also, I would like to thank the other members of my Ph.D. committee who took the effort in reading and providing me with valuable comments on earlier versions of this thesis: Professor Anshel Gorokhovsky, Professor Swapan Gayen,

Professor Vladimir Petricevic, Professor Ping-Pei Ho and Professor Roger Dorsinville. I thank you all.

All the researchers in the group, especially my co-authors of the papers we have published in the context of this dissertation, Professor Robert R. Alfano, Dr. Hakan Altan, Dr. Baolong Yu and Mr. David Matten, have been great importance for me. Especially the strict and extensive comments and the many discussions and the interactions with Professor Robert R. Alfano had a direct impact on the final form and quality of this thesis. The discussions with and friendly advises and tips from Hakan Altan helped me a lot in staying at the right track in the work. David Matten made the program that I implemented for our detection system to obtain experimental data in chapter 2.

I also thank Dr. Wubao Wang, Dr. Guicheng Tang, Dr. Wei Cai and Dr. Shengkun Zhang for their helpful discussions and suggestions during my studies. Furthermore, it has been a pleasure to cooperate with Mr. Yuri Budansky and Mr. Jingcheng Luo regarding technical matters due to electronics and mechanics of our experimental set-ups. During the most recent work on KCl solutions and water vapor preparations, I have had a pleasant cooperation with Dr. Vladimir Kartazayev who was very helpful and Ms. Angela Saint for helping me on the preparation of KCl solutions and humidity measurements. I have had the pleasure of spending time with other researchers in our group, Mrs. Chenghui Liu and Mrs. Xiangchun Liang, who each in their own way helped me on both my education and personal matters. There

has always being a helping hand whenever I needed one! Finally, my beloved husband, Professor Xiantao Li, has always been there whenever I need to discuss things in the ways of science or get my mind off science.

During the preparation of this thesis I have received valuable help and advice from Dr. Hakan Altan, Manuel E. Zevallos L., Kestutis Sutkus and Masood Siddique. Thank you all.

Table of Content

List of Tables

List of Figures

Thesis Statement

The intermolecular and intramolecular modes of a variety of materials are characterized using Time-Domain Terahertz techniques. Emphasis is given to water, in both liquid and vapor forms. The main focus of the study is the hydrogen bonding dynamics in water vapor, liquid water, salt solutions, tryptophan as well as methanol gases. The terahertz light is sensitive to the low energy interactions that occur among water monomers in both liquid and gas states, and it was found that lower order and higher order hydrogen bonding networks can be clearly distinguished in terahertz spectra of various liquids. There are two commonly used models for the description of the structures in liquid water, they are continuum and mixture. Mixture models usually relate distinct spectral features to structures differing in the extent of *hydrogen bonding*, whereas continuum models treat water in terms of a continuous distribution of *hydrogen bonding* that are presumed to be spectroscopically similar. For liquid water, the mixture model is adopted since previous research favors this model. In one experiment for THz absorption of liquid water at room temperature, an absorption mode at 53cm^{-1} was observed which was attributed to the hydrogen bond bending motions in the 5-molecule tetrahedral structure. Clear differences between the absorption levels in neat liquid water, heavy water and KCl-water solutions are seen at room temperature due to the fractional distribution of water structures, e.g. dimer, trimer. Similar interactions were responsible for the observed violation of Beer's Law for water vapor as the concentration of water monomers were increased (humidity)

along the terahertz beam path. The main observation was that as the concentration of the water vapor increases, c, the absorption intensity, $\alpha(\nu)$, of some absorption modes increases, while the absorption intensity of other absorption modes decreases. This is due to the two types of water molecules in terms of nuclear spin of hydrogen atoms in water molecules: *para-water and ortho-water*.

During the course of these investigations, additional materials such as tryptophan and methanol vapors were characterized as well using time-domain terahertz spectroscopy. The two observed absorption modes in tryptophan (an amino acid essential for living functions of a variety of organisms) reflect the vibrational torsions among the ring and chain structures of the molecule. This assignment is based on a theoretical Molecular Dynamics simulation. In methanol gas, a series of equidistant micro-radiations are observed after the main terahertz pulse. This experimental result well verifies the characteristics of equidistant rotational energy levels in methanol molecule.

Introduction

Water is essential for the function of all cycles inherent to life as we know it. On a macroscopic level and microscopic level we understand the dynamics of water molecules and how they interact with other chemicals, however, little is known experimentally about the interactions of the molecules amongst themselves whether in liquid, solid or vapor phase.

In liquid form, water molecules interact through hydrogen bonding[1], and it has been shown that different types of solutes such as salt and sugar affect this bonding. In vapor form, similar interactions can lead to dimerization and clustering under the right environmental conditions[2] THz spectroscopy is an effective tool in exploring the inter/intra-molecular dynamics since the energies it carries match the difference between some rotational energy levels of molecules By using Terahertz Time-Domain Spectroscopy (THz-TDS) the absorptive effects of water in the far-infrared for different environmental conditions can be characterized since terahertz waves are highly absorbed by water molecules whether in liquid, solid or vapor phase.

Liquid Water

In liquid state, an important well-known feature of water molecule is its *polar* nature, which causes water molecules to be attracted to each other and form *hydrogen-bonding* network[3]. The enhancement or de-enhancement of the hydrogen-bonding network can be resolved with the absorption of the terahertz pulse train upon transmission through a water layer with or without some type of solute. Previous

studies show that in liquid water the absorption in the terahertz frequency range is primarily due to the intermolecular vibrational band, i.e. hydrogen bending band, which is caused by the induced transient dipole moments inside the hydrogen bond network[4,5].

To describe the structures of liquid water, numerous models have been proposed, of which, the two generally used classes of models are often designated as by continuum[6] and mixture[7]. Mixture models usually relate unique spectral features to structures differing in the extent of *hydrogen bonding*, whereas continuum models treat water in terms of a continuous distribution of interactions that are assumed to be spectroscopically indistinguishable. In liquid water, the mixture model is more appropriate since previous laser Raman investigations[8,71] as well as results from nonlinear optical techniques such as stimulated Raman scattering and inelastic harmonic light scattering strongly favor mixture models[9,10]. Previous experiments[11] of THz absorption in liquid water at room temperature show the presence of an absorption mode at $53cm^{-1}$ which has been attributed to the hydrogen bond bending motions in the 5-molecule tetrahedral structure ("cage") that exist between water molecules. By adding solutes such as KCl into liquid water, the absorptive effects due to the hydrogen bonding network can be better understood and can be explained based on the idea of coexistence of 5-molecule, fully hydrogen-bonded structure and partially hydrogen-bonded structure in liquid water. The effect of salts in liquid water structure had also been shown in the previous work[12]. In that research, the addition of

Zn^{2+} and K^{+} cations in pure liquid water significantly enhanced the *supercontinuum* generation compared to the neat liquid water.

Water Vapor

In vapor form, by adjusting the concentration of water monomers in the path of the THz pulse train, clustering effects can be discerned. The absorption is primarily due to the large net dipole moment associated with each water monomer, which in turn causes rotational transitions.[24] Using the THz Time-Domain spectroscopy, the absorption modes in water and heavy water in vapor phase have been obtained at room temperature[13] and are attributed to pure rotational motions of water molecules. These studies always examined the water vapor for fixed humidity (concentrations), and the effect of concentration on the absorbance of the vapor had not been investigated. The absorption coefficient for many materials can be modeled using Beer-Lambert law, which states that the absorption coefficient is inversely dependant on the concentration of the absorbing species. The absorbance was monitored for various humilities[14]. The main observation of the experiments were that as the concentration of the water monomers increases, c, the absorption intensity, $\alpha(\nu)$, of some absorption modes increases, while the absorption intensity of other absorption modes decreases. This effect was explained by the presence of two species of water molecules in terms of nuclear spin of hydrogen atoms: *para-water and ortho-water.*[15]

Methanol Vapor and Tryptophan

The energies associated with THz waves are ideal for studying a variety of low energy phenomena such as low frequency modes ("soft modes") in biological materials as well as rotational modes as was discussed previously for water vapor. In the spirit of characterizing various materials that are important in biological systems, tryptophan and methanol vapor were analyzed using THz-TDS techniques developed at the Institute for Ultrafast Spectroscopy and Lasers at The City College of The City University of New York.

Tryptophan

Tryptophan is an essential amino acid for the functionality of living creatures. It is found in plants and meats and its detection is important from both a biological perspective as well as a sanitary one. For tryptophan molecules, two absorption modes were observed, which are in good agreement with calculations using Molecular Dynamics (MD) simulation. By looking for these two absorption features one can detect the presence of this molecule in various environments. Also the effect if any of interactions in biological processes that involve tryptophan can be discerned by examining these modes.

Methanol Vapor

Methanol, also known as methyl alcohol, wood alcohol or wood spirits, is an chemical compound with chemical formula CH_3OH. It is the simplest alcohol, and is a light,

volatile, colorless, flammable, poisonous liquid with a distinctive odor that is somewhat milder and sweeter than ethanol (ethyl alcohol), and its detection is important from two perspectives: as a harmful agent for living creatures and as an agent that is a marker for the presence of life.

In methanol gas, interestingly, a series of commensurate re-radiations are observed corresponding to the equidistant energy gaps in methanol molecules. From this experiment, the delay times between coherent pulses of ~ 21ps, ~22ps and ~26ps are measured for the CH_3OH, CH_3OD, and CD_3OD corresponding to the inverse of rotational energy spacing for $\Delta J = \pm 1$ transitions, respectively. This observation helped us better understand the properties of methanol gas in the molecular level.

Chapter 1- Terahertz Time-domain spectroscopy

After their advent in the mid-1960s[16], there has been a rapid progress in ultra fast lasers[17] over the last four decades. Together with the successes in semiconductor technology and non-linear optics it has lead in 1970s to the birth of a new area of applied physics known as *photonics*. One of the most fascinating photonic spectroscopic applications is Terahertz Time-Domain Spectroscopy (THz-TDS). It appeared in mid 80s in the pioneering works of D. H. Auston[18] D. Grischkowsk[19], X. C. Zhang and B. B. Hu[20] and has become a technique applicable to materials research in early 1990s. [21,22] Now, it is a rapidly developing measurement technique constantly finding new applications in various areas such as physics, chemistry and biology materials science[23,24]. Far infrared imaging based on THz-TDS is currently an extremely promising non-destructive method for testing samples from packaged goods to artworks[25].

As shown in Figure1.1, terahertz region of the electromagnetic spectrum spans the frequency range between the mid-infrared and the microwave region. Terahertz frequencies may vary from 0.1-10THz (1THz ~ 1ps ~300um ~ 33cm^{-1} ~4.1eV ~ 47.6 °K). Due to its large wavelength, while terahertz beams are less scattered passing through various media, unlike microwaves many materials still show unique spectra in this region. By implementing terahertz time-domain spectroscopy we are able to study molecular dynamics that is of a particular interest for materials science.

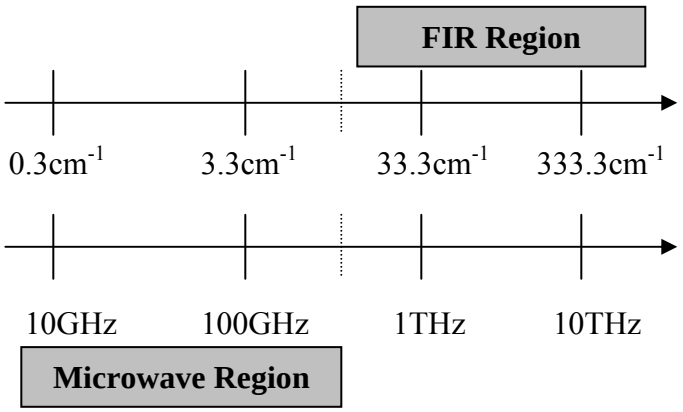

Figure1.1Overview of frequency regions in electromagnetic spectrum

In addition to studying liquid water mixtures and water vapor, we have applied this technique to investigate the dielectric relaxation properties of the liquid CS_2, [26] the vibration-torsion modes in tryptophan[27], the absorption spectrum of liquid water and heavy water vapor, as well as the coherent rotational excitation and dephasing of methanol gas and its isotopes[28]. Details of these works are given in the later chapters.

1.1 The Principles of Terahertz Time-domain Spectroscopy (THz-TDS)

Common optical spectroscopy techniques only measure the intensity of light beams at specific frequencies. In the THz-TDS technique we can directly measure the temporal profiles of terahertz beams, including both amplitude and phase information of the electric field. Therefore, the real and imaginary parts of the dielectric constant can be obtained directly from the measurement without using the Kramers-Kronig relations to calculate these values. However, in instances where you have layered materials, with

varying index of refraction, Kramers-Kronig based transmission or reflection models are necessary to accurately characterize each layer.[29]

The basic principle behind implementing THz time-domain spectroscopy can be described in the following way: a subpicosecond-picosecond pulse of electromagnetic radiation transmits through the material of interest. These materials modify the time-domain profile of THz pulse by reducing the amplitude and introducing a phase shift as well as ringing due to dispersion and absorption with respect to the reference profile, for which the measurement is taken in a nitrogen purged environment without a sample in the pathway. After applying a computer aided algorithm, a Fast Fourier Transform (FFT) and using the Beer's Law in the frequency domain when appropriate (it has been shown that Beer's law is invalid for large intensities as well as large concentrations of absorbing species where non-linear effects have to be considered) [30], the refractive index and power absorption coefficient of the sample material can be extracted.

Figure 1.2a shows the time-domain THz profile through water vapor (sample) at a measured humidity of 68%, and nitrogen purged environment (reference, Figure 1.2b). Both absorption and dispersion features from water vapor are seen in the time-domain profile of the transmission through the water vapor. Figure 1.2b shows the corresponding Fast Fourier Transform (done by using Origin software) of the time domain THz signals, the absorption features are shown as dips in frequency domain. The phase information can also be shown at the same time when necessary. To obtain

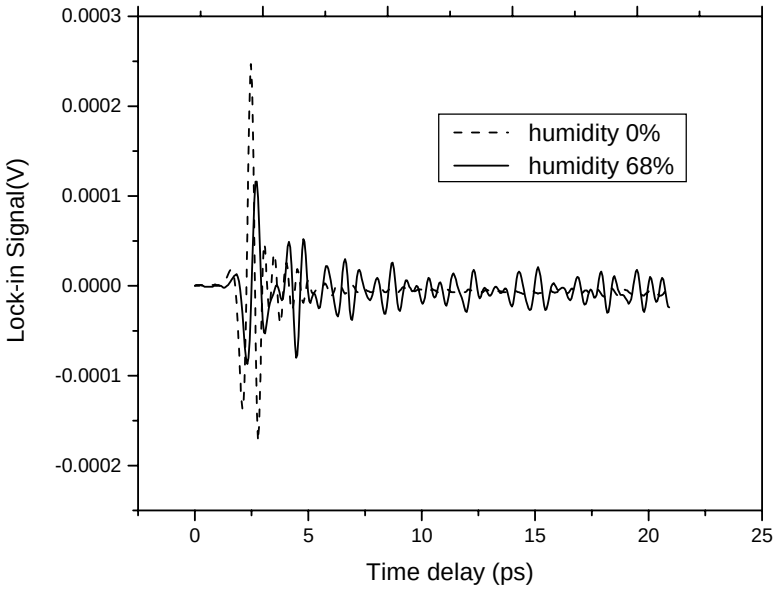

Figure1.2 (a) The time-domain profiles of THz signals in empty cell (dashed line) and water vapor (solid line).

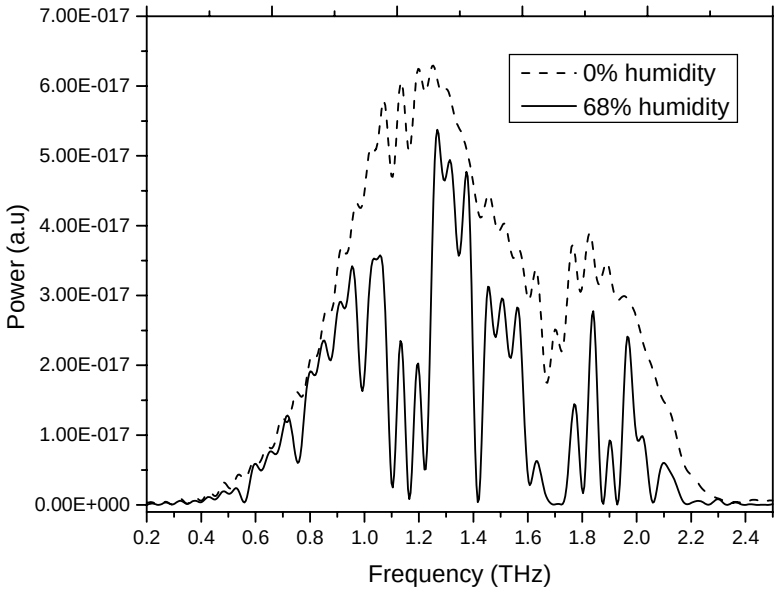

Figure1.2 (b) The power absorption of reference (dashed line) and water vapor (solid line).

the absorption coefficient in the frequency domain one can use Beer's Law (Equation 1.1):

$$\alpha(\nu) = -1/d \times \ln(\frac{I_t}{I_0}) \qquad \textbf{(1.1)}$$

where I_t and I_0 are the measured powers of transmitted and reference time domain signals respectively. The nonlinear optical processes invoked by especially intense light source can cause a variance to the Beer's Law. Our measurements were done with two THz-TDS systems. The THz power from the IMRA system (See Fig. 2.7a) is on the order of 1000 times less than that from the Ti-Sapphire laser pumped system (See Fig. 2.7b). Absorption coefficients measured with the two systems are the same. In addition, in both cases the THz pulse energy is less than a few picojulses, so that we can safely ignore the nonlinear effects in our experiments.

The index of refraction can be extracted from the measured phase shift between the reference and sample THz signals:

$$n(\nu) = [\frac{\Delta\phi(\nu) \times c}{d \times 2\pi\nu}] \qquad \textbf{(1.2)}$$

where $\Delta\phi(\upsilon)$ is the phase shift between the two signals, ν is the frequency and c is the speed of light in vacuum, and when the reference is taken in air or nitrogen environment, the index of refraction is described as: $n(\nu) = [\frac{\Delta\phi(\nu) \times c}{d \times 2\pi\nu}] + 1$.

Furthermore, the dielectric constant $\hat{\varepsilon}(\omega)$ can be obtained from:

$$\hat{\varepsilon}(\omega) = \varepsilon'(\omega) - i\varepsilon''(\omega) \quad \textbf{(1.3)}$$

which is related to the complex index of refraction:

$$\hat{n}(\omega) = n(\omega) - i\kappa(\omega) \quad \textbf{(1.4)}$$

through the relations:

$$\varepsilon'(\omega) = n^2(\omega) - \kappa^2(\omega) \quad \textbf{(1.5)}$$

and

$$\varepsilon''(\omega) = 2n(\omega)\kappa(\omega) \quad \textbf{(1.6)}$$

Where $\omega = 2\pi\nu$, and $\kappa(\omega) = \lambda\alpha(\omega)/4\pi = c\alpha(\omega)/2\omega$ with λ being the vacuum wavelength and c the speed of light in vacuum. Conversely, given the $\varepsilon'(\omega)$ and $\varepsilon''(\omega)$; $n(\nu)$ and $\alpha(\nu)$ are seen to be:[31]

$$n(\nu) = \left(\frac{\sqrt{\varepsilon'(2\pi\nu)^2 + \varepsilon''(2\pi\nu)^2} + \varepsilon'(2\pi\nu)}{2}\right)^{1/2} \quad \textbf{(1.7)}$$

$$\alpha(\nu) = \frac{4\pi\nu}{c}\left(\frac{\sqrt{\varepsilon'(2\pi\nu)^2 + \varepsilon''(2\pi\nu)^2} - \varepsilon'(2\pi\nu)}{2}\right)^{1/2} \quad \textbf{(1.8)}$$

For the optical spectroscopy techniques which are not phase sensitive and the index of refraction can not be measured directly as in THz-TDS technique, where both the absorption coefficient and index of refraction can be extracted at the same time from one measurement, the Kramers-Kronig relation has to be used. This is the advantage of THz-TDS technique.

Due to the fact that water vapor has a lot of absorptions in THz frequency range, we blow nitrogen gas into the terahertz spectrometer cage to drive away water vapor. In time domain profile, the 0*ps* point is attributed to be the point where the terahertz pulse overlaps with the gating optical beam. At that moment the peak of THz signal is expected to appear. The more data points taken in time domain, the better resolution will be obtained in frequency domain provided that it is still within the moving resolution limit of the translation stage used for delaying of the optical gating beam. Usually “zero padding” (inserting zeros to the end of the data set measured in time domain) is to used in order to reveal the spectral features in frequency domain. The added zeros will insure the Fourier Transform appears smoother and the frequency-domain features are better resolved.

Chapter 2-THz Pulse Generation and Detection

Starting from the mid- 80s, a variety of materials were reported to emit subpicosecond THz pulses. Two rather distinct mechanisms have been used most widely for the generation of such pulses: optical rectification in crystals with large second order nonlinearity, like ZnTe[32], LiTaO3[33], DAST[34] or GaSe[35] and transient photo-conductivity in semiconductors such as LTG-GaAs[36] and GaAs.[37] For the detection mechanisms, the free space Electro-optic sampling (FSEOS) and photoconductive antennas are used frequently.[38]

2.1 Terahertz Generation by Optical Rectification

2.1.1 Optical Rectification

Two THz-TDS systems were developed in our lab to characterize various materials in transmission mode only. In these systems optical rectification is used as a means to generate the THz beam. In both systems, the terahertz pulses are generated through a <110> oriented ZnTe crystal. The first system uses a Ti: Sapphire oscillator which is subsequently amplified, delivering pulses centered at λ~800*nm*, and duration τ~70*fs* at a repetition rate of 250 *KHz*, with an average power of ~1*W*. The second system is more compact and uses an Erbium doped mode-lock fiber laser, which has a center wavelength of ~810*nm*, and pulse duration of ~120*fs* at a repetition rate of 75 *MHz*, with an average power of ~100*mW*. At the wavelength of ~800*nm* the phase matching conditions reading as V_{group}*(optical)* = V_{phase}*(THz)* is met well in ZnTe, such that the energy conversion efficiency from optical pulse to THz pulse is the most efficient.

Optical rectification[39] can be described as difference frequency mixing and occurs in media with large second order susceptibility, $\chi^{(2)}(\omega_3=\omega_2-\omega_1, \omega_2, \omega_1)$. It is analogous to sum-frequency mixing $\chi^{(2)}(\omega_3=\omega_2+\omega_1, \omega_2, \omega_1)$. As wave interacts in a nonlinear medium, it generates waves at sum and difference frequencies.[40] The physical meaning of the sum-frequency generation is: the laser beams at ω_1 and ω_3 interact in a nonlinear crystal and generate a polarization at frequency ω_3 :

$$P^{(2)}(\omega_3 = \omega_2 + \omega_1) = \chi^{(2)}(\omega_3 = \omega_2 + \omega_1) : E(\omega_1)E^*(\omega_2) \qquad \textbf{(2.1)}$$

where $\chi^{(2)}$ is the second-order susceptibility tensor assumed to be frequency independent, $P^{(2)}(\omega_3 = \omega_2 + \omega_1)$ is a collection of oscillating dipoles acting as the radiation source. For effective energy transfer from pumping waves at ω_2, ω_1 to the generated waves at ω_3, in the sum-frequency generation shown as in Figure 2.1, the conservation law of energy and momentum must be satisfied. The energy conservation

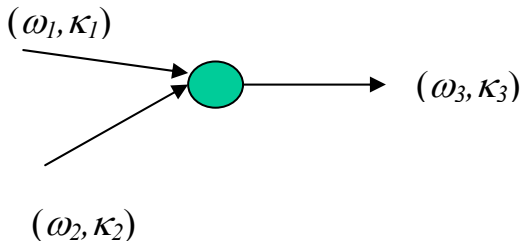

Figure 2.1 Scheme of sum-frequency generation

requires $\omega_3=\omega_2+\omega_1$, while the momentum conservation requires: $\kappa_3=\kappa_2+\kappa_1$, indicating that the most effective sum-frequency generation is under phase matching conditions.

For difference-frequency generation, the scheme is the same as one for the sum-frequency generation except that the two frequencies are differenced to each other instead of summing. Here, the induced polarization in the crystal oscillates at the difference of the individual frequencies:

$$P^{(2)}(\omega_3 = \omega_2 - \omega_1) = \chi^{(2)}(\omega_3 = \omega_2 - \omega_1) : E(\omega_1)E^*(\omega_2) \qquad \textbf{(2.2)}$$

If the two mixed frequencies from the laser beams are ω_1, ω_2, *with* $\omega_2=\omega_1-\omega$ and $E_1(\omega) = \xi_1(r)\exp(ik_1 z - i\omega_1 t)$ with $E_2(\omega) = \xi_2(r)\exp(ik_2 z - i\omega_2 t)$, the nonlinear polarization induced at the difference frequency is given by:

$$P^{(2)}{}_{THz}(\omega) = \chi^{(2)} : E(\omega_1)E^*(\omega_1 - \omega) \qquad \textbf{(2.3)}$$

In both sum-frequency generation and difference-frequency generation, the induced polarization is proportional to the intensity of input optical beam:

$$P^{(2)}(\omega) \propto \chi^{(2)}(\omega) I_{pump}(\omega) \qquad \textbf{(2.4)}$$

The coupled wave equation relation between the generated field amplitude $E_{THz}(z,t)$ and the generating waves as propagating forward can be expressed as following under the infinite plane-wave approximation with pump intensities being approximated as constant

$$(\frac{\partial}{\partial z}+\frac{1}{v_{g1}}\frac{\partial}{\partial t})E_{\Omega_{THz}}(z,t)=-\frac{2\pi}{ikc^2}\frac{\partial^2}{\partial t^2}P^{NL}(\Omega_{THz},z,t)e^{i[\Omega_{THz}t-k(\Omega_{THz})z]}$$

(2.5)

Where, v_{g1} is the group velocity of $E_{\Omega_{THz}}(z,t)$: $\left(dk/d\omega\right)^{-1}$

$E_L(z,t)$ is the pumping laser pulse propagation expressed as:

$$E_L(z,t)=E_{L0}e^{-i(\omega t-kz)}$$

$P^{NL}(\Omega_{THz},z,t)$ is the nonlinear polarization induced by the two pumping laser pulses in the crystal, which can be described as:

$$\begin{aligned}P^{NL}(\Omega_{THz},z,t)&=\chi^2(\Omega_{THz}=\omega_1-\omega_2):E_{L1}E_{L2}{}^*\\&=\chi^2:E_{L0}{}^2(t)e^{-i(\omega_1 t-k_1 z)}e^{i(\omega_2 t-k_2 z)}\end{aligned}$$

(2.6)

χ^2 is the second order nonlinear coefficient.

Let $\omega_1=\omega_0+\Omega_{THz},\omega_2=\omega_0$, then

$$P^{NL}(\Omega_{THz},z,t)=\chi^2(\Omega_{THz}=\omega_1-\omega_2):E_{L0}{}^2(t)e^{-i[\omega_0 t+\Omega_{THz}t-k(\omega_0+\Omega_{THz})z]}e^{i[\omega_0 t-k(\omega_0)z]}$$

$$(\frac{\partial}{\partial z}+\frac{1}{v_{g1}}\frac{\partial}{\partial t})E_{\Omega_{THz}}(z,t)=-\frac{2\pi}{ikc^2}\frac{\partial^2}{\partial t^2}P^{NL}e^{i[\Omega_{THz}t-k(\Omega_{THz})z]}$$

$$=-\frac{2\pi\chi^2}{ikc^2}\frac{\partial^2}{\partial t^2}\{E_{L0}{}^2(t)e^{-i[\omega_0 t+\Omega_{THz}t-k(\omega_0+\Omega_{THz})z]}e^{i[\omega_0 t-k(\omega_0)z]}\}e^{i[\Omega_{THz}t-k(\Omega_{THz})z]}$$

(2.7)

Under the infinite plane-wave approximation, taking $E_{L0}{}^2(t)$ as a constant, the above equation becomes:

$$(\frac{\partial}{\partial z}+\frac{1}{v_{g1}}\frac{\partial}{\partial t})E_{\Omega_{THz}}(z,t)=-\frac{2\pi}{ikc^2}\frac{\partial^2}{\partial t^2}P^{NL}(\Omega_{THz},z,t)e^{i[\Omega_{THz}t-k(\Omega_{THz})z]}$$

$$=-\frac{2\pi\chi^2{E_{L0}}^2}{ikc^2}\frac{\partial^2}{\partial t^2}\{e^{-i[\omega_0 t+\Omega_{THz}t-k(\omega_0+\Omega_{THz})z]}e^{i[\omega_0 t-k(\omega_0)z]}\}e^{i[\Omega_{THz}t-k(\Omega_{THz})z]}$$

$$=-\frac{2\pi\chi^2{E_{L0}}^2}{ikc^2}\frac{\partial^2}{\partial t^2}\{e^{i[-\Omega_{THz}t+k(\omega_0+\Omega_{THz})z-k(\omega_0)z]}\}e^{i[\Omega_{THz}t-k(\Omega_{THz})z]}$$

(2.8)

Let z'=z, τ= t-z/v_{g1}

Let:

$$\frac{\partial}{\partial z}=\frac{\partial z'}{\partial z}\frac{\partial}{\partial z'}+\frac{\partial\tau}{\partial z}\frac{\partial}{\partial\tau}=1\times\frac{\partial}{\partial z'}+(-\frac{1}{v_{g1}})\frac{\partial}{\partial\tau}=\frac{\partial}{\partial z'}-\frac{1}{v_{g1}}\frac{\partial}{\partial\tau}$$

$$\frac{\partial}{\partial t}=\frac{\partial\tau}{\partial t}\frac{\partial}{\partial\tau}+\frac{\partial z'}{\partial t}\frac{\partial}{\partial z'}=1\times\frac{\partial}{\partial\tau}+0\times=\frac{\partial}{\partial\tau}$$

$$\frac{\partial}{\partial z'}E_{\Omega_{THz}}(z',t)=-\frac{2\pi}{ikc^2}\frac{\partial^2}{\partial\tau^2}P^{NL}e^{i[\Omega_{THz}(\tau+z'/v_{g1})-k(\Omega_{THz})z']}$$

$$=-\frac{2\pi\chi^2{E_{L0}}^2}{ikc^2}\frac{\partial^2}{\partial\tau^2}\{e^{-i[\Omega_{THz}\tau+\Omega_{THz}z'/v_{g1}-k(\omega_0+\Omega_{THz})z'+k(\omega_0)z']}\}e^{i[\Omega_{THz}(\tau+z'/v_{g1})-k(\Omega_{THz})z']}$$

$$=-\frac{2\pi\chi^2{E_{L0}}^2}{ikc^2}\frac{\partial^2}{\partial\tau^2}\{e^{i[-\Omega_{THz}(\tau+z'/v_{g1})+k(\omega_0+\Omega_{THz})z'-k(\omega_0)z']}\}e^{i[\Omega_{THz}(\tau+z'/v_{g1})-k(\Omega_{THz})z']}$$

(2.9)

Then,

$$-\Omega_{THz}(\tau + z'/v_{g1}) + k(\omega_0 + \Omega_{THz})z' - k(\omega_0)z' = \alpha \quad ,$$

$$\Omega_{THz}(\tau + z'/v_{g1}) - k(\Omega_{THz})z' = \beta \quad ,$$

The above equation will be:

$$\frac{\partial}{\partial z'}E_{\Omega_{THz}}(z',t) =$$

$$-\frac{2\pi\chi^2 {E_{L0}}^2}{ikc^2}\frac{\partial^2}{\partial\tau^2}\{e^{i[-\Omega_{THz}(\tau+z'/v_{g1})+k(\omega_0+\Omega_{THz})z'-k(\omega_0)z']}\}e^{i[\Omega_{THz}(\tau+z'/v_{g1})-k(\Omega_{THz})z']}$$

$$=-\frac{2\pi\chi^2 {E_{L0}}^2}{ikc^2}\{\frac{\partial^2}{\partial\tau^2}[\cos\alpha + i\sin\alpha]\}[\cos\beta + i\sin\beta]$$

$$=-\frac{2\pi\chi^2 {E_{L0}}^2}{ikc^2}\{-{\Omega_{THz}}^2[\cos\alpha + i\sin\alpha]\}[\cos\beta + i\sin\beta]$$

$$=-\frac{2\pi\chi^2 {E_{L0}}^2(-{\Omega_{THz}}^2)}{ikc^2}[\cos(\alpha+\beta) + i\sin(\alpha+\beta)]$$

(2.10)

Since $\alpha + \beta = k(\omega_0 + \Omega_{THz})z' - k(\omega_0)z' - k(\Omega_{THz})z' = \Delta kz'$, the above equation becomes:

$$\frac{\partial}{\partial z'}E_{\Omega_{THz}}(z',t) = -\frac{2\pi\chi^2 {E_{L0}}^2(-{\Omega_{THz}}^2)}{ikc^2}[\cos(\alpha+\beta) + i\sin(\alpha+\beta)]$$

$$= \frac{2\pi\chi^2 {E_{L0}}^2{\Omega_{THz}}^2}{ikc^2}[\cos(\Delta kz') + i\sin(\Delta kz')]$$

$$= -\frac{2\pi\chi^2 {E_{L0}}^2{\Omega_{THz}}^2}{kc^2}[i\cos(\Delta kz') - \sin(\Delta kz')]$$

(2.11)

By integration on z' from 0 to length L, we have the generated electrical field at location L since Δk is independent of z':

$$E_{\Omega_{THz}}(z',t) = \int_0^L -\frac{2\pi\chi^2 {E_{L0}}^2 {\Omega_{THz}}^2}{kc^2}[i\cos(\Delta kz') - \sin(\Delta kz')]dz'$$

$$= -\frac{2\pi\chi^2 {E_{L0}}^2 {\Omega_{THz}}^2}{kc^2}\int_0^L [i\cos(\Delta kz') - \sin(\Delta kz')]dz'$$

$$= -\frac{2\pi\chi^2 {E_{L0}}^2 {\Omega_{THz}}^2}{kc^2}\{\frac{i}{\Delta k}\sin(\Delta kL) + \frac{1}{\Delta k}[\cos(\Delta kL - 1)]\}$$

$$E_{\Omega_{THz}}(z',t) = -\frac{2\pi\chi^2 {E_{L0}}^2 {\Omega_{THz}}^2}{kc^2}\frac{1}{\Delta k}\{i\sin(\Delta kL) + [\cos(\Delta kL - 1)]\}$$

(2.12)

And:

$$\left|E_{\Omega_{THz}}(z',t)\right| = \frac{2\pi\chi^2 {E_{L0}}^2 {\Omega_{THz}}^2}{kc^2}\frac{1}{\Delta k}\sqrt{\{[\sin(\Delta kL)]^2 + [\cos(\Delta kL - 1)]^2\}}$$

$$= \frac{2\pi\chi^2 {E_{L0}}^2 {\Omega_{THz}}^2}{kc^2}\frac{1}{\Delta k}2\sin(\Delta kL/2)$$

$$= \frac{4\pi\chi^2 {E_{L0}}^2 {\Omega_{THz}}^2}{kc^2\Delta k}\sin(\Delta kL/2)$$

$$= \frac{4\pi\chi^2 {E_{L0}}^2 {\Omega_{THz}}^2}{kc^2}\frac{\sin(\Delta kL/2)}{\Delta kL/2}\frac{L}{2}$$

$$= \frac{2\pi\chi^2 {E_{L0}}^2 {\Omega_{THz}}^2 L}{kc^2}\frac{\sin(\Delta kL/2)}{\Delta kL/2}$$

(2.13)

The intensity of the generated electrical field is:

$$
\begin{aligned}
I_{\Omega_{THz}}(z',t) &= \left| E_{\Omega_{THz}}(z',t) \right|^2 \\
&= [\frac{4\pi\chi^2 {E_{L0}}^2 {\Omega_{THz}}^2}{kc^2\Delta k}]^2 \sin^2(\Delta kL/2) \\
&= \frac{[4\pi\chi^2 {E_{L0}}^2 {\Omega_{THz}}^2]^2}{[kc^2]^2} \frac{\sin^2(\Delta kL/2)}{\Delta k^2 L^2/2^2} \frac{1}{4} L^2 \\
&= \frac{4[\pi\chi^2 {E_{L0}}^2 {\Omega_{THz}}^2]^2}{[kc^2]^2} \frac{\sin^2(\Delta kL/2)}{[\Delta kL/2]^2} L^2
\end{aligned}
$$

(2.14)

When phase match $\Delta k -> 0, I_{\Omega_{THz}}(z',t) -> I_{Max} = \frac{4[\pi\chi^2 {E_{L0}}^2 {\Omega_{THz}}^2]^2}{[kc^2]^2} L^2.$

With $k = \Omega_{THz}\sqrt{\varepsilon(\Omega_{THz})}/c,, I_{Max} = \frac{4[\pi\chi^2 {E_{L0}}^2 {\Omega_{THz}}^2]^2}{[kc^2]^2} L^2 = \frac{[2\pi\chi^2 {E_{L0}}^2 \Omega_{THz} L]^2}{c^2}$

The above equation is only for generated discrete frequencies; we can integrate the entire frequency range to have an expression for a terahertz bandwidth.

The predicted terahertz pulse shape in the time domain would be the derivative of the visible pulse envelope at the phase-matching condition: $n_{VIS} = n_{THz}$

$$E_{THz}(t) \propto \frac{\partial^2 P(t)}{\partial^2 t} = \chi^{(2)} \frac{\partial^2 I(t)}{\partial^2 t} \qquad \textbf{(2.15)}$$

where $E_{THz}(t)$ is the induced THz electrical field, *I(t)* the optical field intensity profile, showing the phenomenon of optical rectification.

Another requirement is that generated difference frequencies in the optical domain occur only if extreme spectral components within the single-pulse spectrum are sufficiently apart. But all the spectral components have to be in-phase. For ultrashort laser pulses that have large bandwidth the frequency components are differenced with each other to produce bandwidth from 0 to several THz. Broadband THz signals up to 40THz has been generated by using ultra thin ZnTe (30*um*) crystals through optical rectification[41]. In Figure 2.2, an ultrafast laser pulse in the nonlinear crystal <110> oriented ZnTe creates a beating polarization, which is a transient dipole moment. At normal incidence the terahertz radiation from this crystal is purely due to optical rectification. There are radiations on both directions: forward and backward. However, when considering the convenience of detection and multiple reflections from the crystal surfaces, the forward THz radiation is often preferred. The green fluorescence accompanying with the THz radiation is from two-photon absorption of the input laser beam in the generating ZnTe crystal. At high laser intensities, the two-photon absorption results in the generation of free carriers thus increasing the absorption of terahertz radiations in the crystals. In addition, the two-photon absorption leads to a reduction of the intensity of the laser pulse propagating in the crystal. Both effects reduce the THz generation efficiency in ZnTe crystal at high laser intensities [42]. At moderate laser intensities, the nonlinear absorption cannot result in strong decrease of THz power by strengthening the focus of optical radiation or by the divergence of the THz radiation since it is only slightly changed when the beam waist is inside the crystal[43]. We used the tight focusing in our Erbium doped mode locked

fiber laser based THz spectrometer (IMRA F-100), where the input laser power is not so intense.

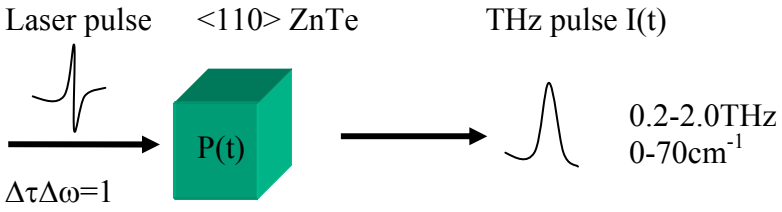

Figure 2.2 Illustration of terahertz generation by optical rectification

This can be qualitatively better understood by considering a crystal whose symmetry is very low to provide a preferred internal direction, so that the polarization induced by an applied electric field does not reverse when the electric field is reversed. If the applied electric field varies sinusoidally in time, then a net time average polarization will be developed, in analogy with the dc currents[44].

2.1.2 Kerr Effect Used in THz Detection Process

The Kerr effect or the quadratic electro-optic effect (QEO effect) is a change in the refractive index of a material in response to an electric field. It is different when compared to the Pockels effect in that the induced index change is directly proportional to the *square* of the electric field instead of to the magnitude of the field. All materials show a Kerr effect, but some liquids display the effect more strongly than other materials do. At the Institute for Ultrafast Spectroscopy and Lasers, Robert

R. Alfano and P. P. Ho had done extensive work of optical Kerr Effect in liquids since 1979. [45, **Error! Bookmark not defined.**]

During the construction of the compact THz-TDS setup based on the Er: doped mode locked fiber laser, a CS_2 Kerr cell was used to assist in locating the overlapping area between the pumping and probing laser beams. The CS_2 liquid is put in a 1*cm* quartz cell to form a CS_2 Kerr Cell, and then placed in the intersection area of the two beams.

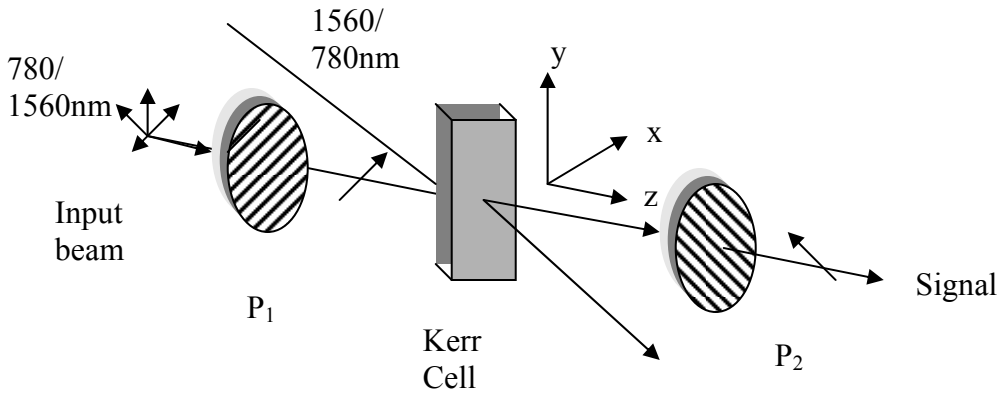

Figure 2.3 Schematic diagram of the optical Kerr gate, the polarization axes of the polarizers are labeled by P_1 and P_2.

By adjusting the delay between the pumping and the probing beams, the Kerr signal, otherwise the overlapping point was found, which occurs at about 5*ps* after the scanning (Fig.2.4). The Kerr setup is very similar to the one used by P. P. Ho and R. R. Alfano.[45] In Fig.2.3, the two polarizers are perpendicular to each other. After passing through the first polarizer P_1, the natural polarizations of the probing beam

become parallel to x-axis. When pumping pulse is not present in the Kerr cell, the polarization of the probing beam stays parallel to x-axis so that none of the probing beam transmits through the second polarizer P_2. There is no signal detected. When the pump beam pulse is present and overlaps with the probing pulse in the Kerr cell, it introduces a transient birefringence, inducing a difference between the indices of the refraction parallel and perpendicular to the laser field. The polarization of the probing beam then rotates such that it transmits through the second polarizer. Subsequently the signal is detected. The observed Kerr signals are shown in Figure 2.4. The three curves show different Kerr Effect signals under pump-probe scheme of (1) 1560nm-780nm, (2) 780nm-780nm, and (3) 1560nm-780nm. The laser source (IMRA AMERICA INC.-CP 25) gives dual beams centered at 1560nm and 780nm respectively. This laser is very similar to the higher power, IMRA AMERICA INC., F-100 series laser used

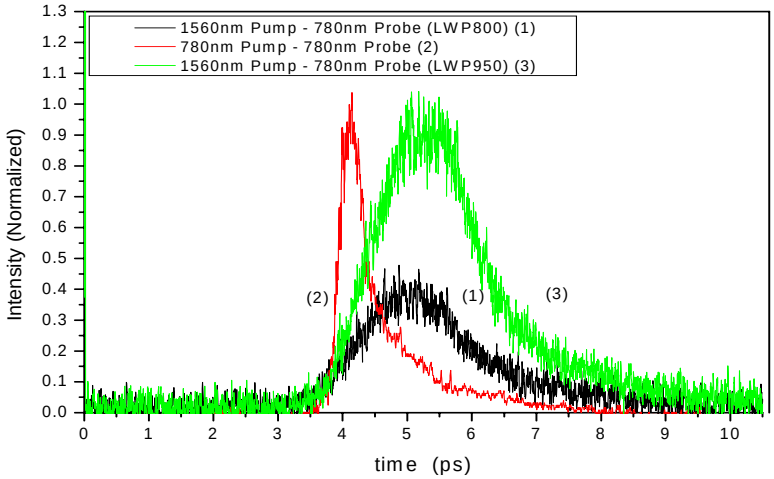

Figure 2.4 Kerr Effect in liquid CS_2 at different pump, probe wavelengths.

for THz generation, which emits dual beams centered at a wavelength of 1620nm and 810nm respectively. Long-pass wave plates were used to pick one of the beams as either the pumping or probing source. The difference among three profiles, which is measured from the same liquid CS_2 cell, indicates that the Kerr Effect depends on wavelengths. [45]

2.2 Electro-optic Sampling in ZnTe Crystal for THz Detection

2.2.1 Introduction

The Electro-optic sampling is used to exploit the linear electro-optic effect. The ultra short optical pulses used in the electro-optic detecting allow a small time interval where the electric field can influence the optical beam. The influence is a change of polarization in the probing beam. The electric field can then be extracted by slowly varying the arrival time of the probe pulse. For each relative time delay, the signal can be obtained by averaging many pulses using a mechanical chopper and lock-in amplifier, so that the noise averages out and a very high sensitivity is achieved.

The electro-optic sampling (EOS) [46] is a powerful method for the detection of THz pulses.[47,48] It is based on the electric field of a THz pulse by inducing a small birefringence in an electro-optic crystal. By passing through such a crystal, the initially linearly polarized optical probe beam gains small elliptical polarization when the terahertz field is present. In Figure 2.5, the $\lambda/4$ plate after the ZnTe detecting crystal adds a $\pi/2$ dephasing to the optical probing beam, making its linear polarization into circular polarization when no THz electric field is present in the

ZnTe crystal. When the THz field is present in the ZnTe crystal the linear polarization is converted into elliptical polarization and remains elliptical as it passes through the quarter-wave plate. Subsequent analysis by a Wollaston polarizer gives the intensities of the two components of the resultant elliptically polarized light. The balanced photodiodes select the difference between the two intensities, which is measured with a lock-in amplifier referenced to the modulation of the THz field at certain frequency (3.5 KHz for the IMRA F-100 laser system and 400 Hz for the amplified Ti-sapphire laser system) by using a mechanical chopper on the generating optical beam.

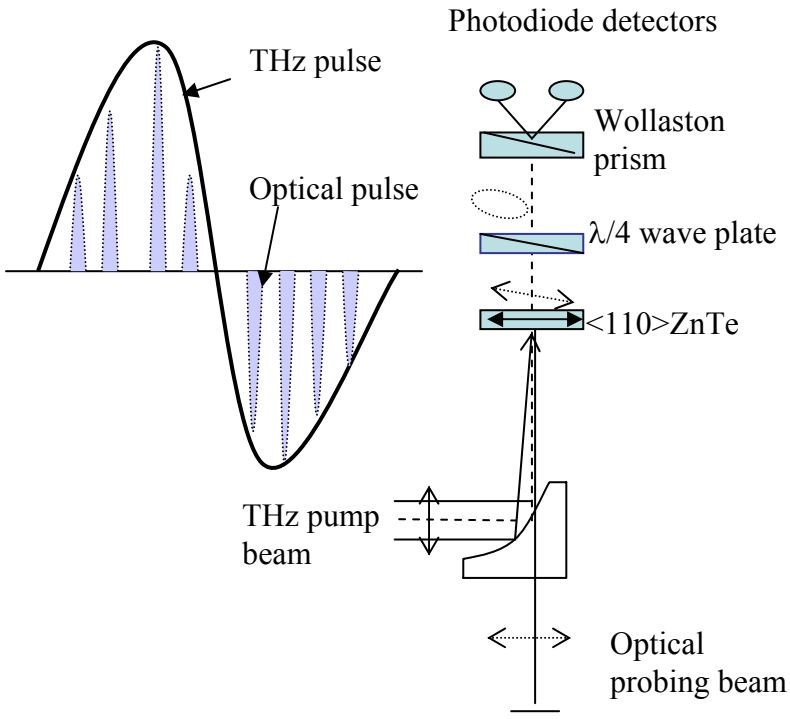

Figure 2.5 Simplified view of electro-optic sampling in between THz pulses and optical probing pulses.

The THz pulse is much longer than the laser pulse (several *p*s vs. tens of *fs*), thus by the variation of the delay between THz and optical probe pulse the whole time profile of the THz pulse are traced. Approximately, the induced ellipticity is proportional to the THz electric field applied to the crystal in every moment of time.

2.2.2 Pockels Effect in <110> ZnTe Crystal

As EOS active medium, ZnTe is a II-IV group compound semiconductor, it has a cubic crystal lattice and is optically isotropic when no electric field is applied owing to its high degree of symmetry ($4\bar{3}m$).[49] The permeability tensor of ZnTe crystal $\hat{\eta}$ is symmetric, hence the nonlinear coefficient tensor $r_{ijk}=r_{jik}$. After replacing the first two indices *i, j* of the tensor ***r*** using a single index by convention, the EO coefficient of ZnTe crystal is:

$(1,1) \sim 1$	$r_{11k} \sim r_{1k=0}$
$(2,2) \sim 2$	$r_{22k} \sim r_{2k=0}$
$(3,3) \sim 3$	$r_{33k} \sim r_{3k=0}$
$(2,3) \sim 4$	$r_{23k} = r_{32k} \sim r_{4k}$
$(1,3) \sim 5$	$r_{13k} = r_{31k} \sim r_{5k}$
$(1,2) \sim 6$	$r_{12k} = r_{21k} \sim r_{6k}$

Figure 2.6 (a) Relative orientation of the THz electrical field $E_{x'}$ and the polarization of the laser probe with respect to the ZnTe crystal. The *x', y', z'* coordinates are set along the main ZnTe crystallographic directions; the THz and the optical probe beams propagation (z′), the THz and the probe beam (x′) polarization directions. (b) the projection of the ellipsoid on the surface of the crystal without THz field present (c) the projection of the ellipsoid on the surface of the crystal with THz field present, the double primed axes correspond to the orientation of the main axes of the distorted index ellipsoid.

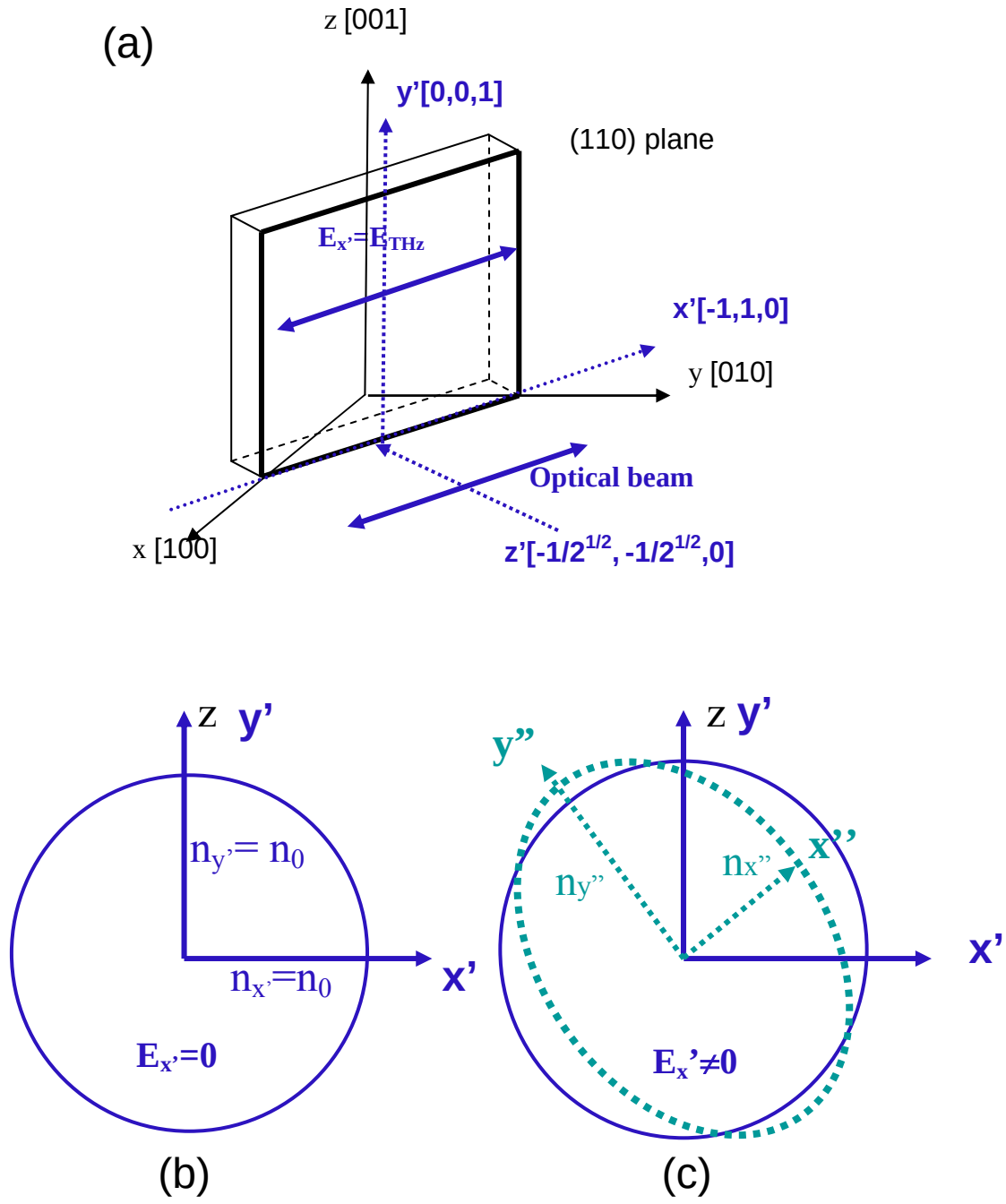

Figure 2.6 (a), (b), (c).

The ZnTe crystal has the same index of refraction in all directions at zero electric fields, i.e. $n_1=n_2=n_3=n_0$, n is the index of refraction in the principle x', y', z' coordinates of the crystal. In ZnTe crystal, the tensor $\boldsymbol{r}$ contains only one independent element: $r_{41}= r_{52}= r_{63} = 4.0\cdot10^{-12}$ m/V. Without electric field applied, the material is the same in all directions so that the refractive-index ellipsoid is simply a sphere (Fig. 2.6b); in this case the coordinate system, x', y', and z', is set along the main crystallographic directions of ZnTe. Under this condition, the equation of the refractive index ellipsoid takes the following form: [50]

$$\frac{x^2}{n_{x'}^2}+\frac{y^2}{n_{y'}^2}+\frac{z^2}{n_{z'}^2}=1 \qquad \textbf{(2.16)}$$

An applied electric field causes changes in optical properties of the crystal. This can be seen as distortions of the refractive-index ellipsoid:

$$\begin{aligned}&(\frac{1}{n^2})_1 x'^2+(\frac{1}{n^2})_2 y'^2+(\frac{1}{n^2})_3 z'^2+\\&2(\frac{1}{n^2})_4 y'z'+2(\frac{1}{n^2})_5 x'z'+2(\frac{1}{n^2})_6 x'y'=1\end{aligned} \qquad \textbf{(2.17)}$$

The linear change for the above coefficient is: $\Delta(\frac{1}{n^2})_i=\sum_1^3 r_{ij}E_j$ and $i=1, 2, 3 \ldots 6$, $j=1$, 2, 3, E_j is a component of the applied electric field and r_{ij} is the electro-optic tensor describing the first order non-linearity. The higher order non-linearities are usually

very small at the field strength typical for THz pulses: $E < 4$ *KV/cm* and can be ignored.

In Figure 2.6a, the polarization of the THz beam and optical beam are parallel to the [-1, 1, 0] crystal direction, the beams travel along the *z'* = [-1,-1, 0]/$\sqrt{2}$ direction. The orientation of the crystal with respect to the propagation direction and polarization of the THz- and the optical probe beam shown corresponds to the strongest induced Pockels effect. Under the influence of the applied THz field the index sphere in Fig.2.6b turns to an ellipsoid with the main axes oriented along *x"*, *y"*, and *z"* directions shown in Fig. 2.6c.

After performing a principle-axis transformation, the modified indices of refraction are:

$$\begin{aligned} n_{z}" &= n_0 \\ n_{y"} &= n_0 + \frac{1}{2} r_{41} \times n_0^3 E_{x'} \\ n_{x"} &= n_0 - \frac{1}{2} r_{41} \times n_0^3 E_{x'} \end{aligned} \qquad \textbf{(2.18)}$$

with approximation of: $r_{41} \times E_{x'} \ll 1/n_0^2$.

Having passed through such crystal, the *y"*- and *x"*-components of the electric field of the incident optical wave acquire a phase shift:

$$\Delta\phi = \phi_{y"} - \phi_{x"} = \frac{L\omega}{c} E_{x'} \left[n_{y"} - n_{x"} \right] \qquad \textbf{(2.19)}$$

after using Equation (2.18), it takes:

$$\Delta\phi = \frac{L\omega}{c} \times n_0^3 \times r_{41} E_{x'} \qquad \textbf{(2.20)}$$

where L is the thickness of the crystal, ω the angular frequency of the laser light. The generated signal is proportional to the THz electric field $E_{x'}$.

2.2.3 The Balanced Detection

The propagation of the polarized probing beam through the induced train of birefringence layers are conveniently described using Jones calculus.[51] As shown in Fig. 2.5, a quarter wave plate, whose main axes are oriented at ±45° with respect to the horizontal direction, is placed behind the electro-optic crystal to make the initially linear polarization of the probe beam (at $E_{THz} = 0$) circular. A Wollaston prism, rotated by 45°, separates the two polarization components, *y"*, *x"* and guides them to the two diodes of the balanced detector, which is connected to the input of a lock-in amplifier. With no THz pulse present, the components have equal intensity and the signal is zero. When the THz field is applied, a non-zero phase shift causes a difference of the two components. As can be seen in Equation (2.20) it is proportional not only to the magnitude of the applied field but also to its sign, which is why this detection method is called phase-sensitive.

If one applies Jones calculus on the optical electric field based on the induced phase shift by THz electric field, the laser amplitude seen in diode 1 and diode 2 are:

$$A_1 = E_{x'} \frac{1}{\sqrt{2}} (\cos(\Delta\phi/2) - \sin(\Delta\phi/2)) \quad \textbf{(2.21)}$$

$$A_2 = -E_{x'} \frac{i}{\sqrt{2}} (\cos(\Delta\phi/2) + \sin(\Delta\phi/2)) \quad \textbf{(2.22)}$$

The difference signal is:

$$|A_1|^2 - |A_2|^2 = E_{x'}{}^2 \sin(\Delta\phi) \quad \textbf{(2.23)}$$

where $\Delta\phi = \frac{\omega \times L}{c} n_0{}^3 r_{41} E_{x'}$ is the induced phase retardation along the two optical axes inside of the ZnTe crystal.

A phase sensitive detection technique, *lock-in detection*, is used to amplify the weak optical signal detected from photodiodes. It is based on the idea of modulating the THz beam at some fixed frequency and detecting the averaged terahertz signal at this slower modulation with respect to the terahertz repetition rate. In both THz-TDS systems, the THz beams are modulated by a mechanical chopper (Stanford Research System, Inc., model SR540), the chopping frequency is 3.5 *KHz* for the system employing the mode-locked Erbium doped fiber laser source, and 400*Hz* for the system using the amplified Ti: Sapphire oscillator as the laser source. In Fig.2.5, output from individual photodiodes can be directly connected to the differential input of the lock-in amplifier (LIA SR530 for the amplified laser driven THz-TDS set-up and LIA SR830 for the Er:doped mode locked fiber laser driven the terahertz set-up), or by using a special balanced photo detector (New Focus, Inc., Model 2307) the signal can be monitored directly through single inputs. The delay stage (Aerotech,

Inc., Model ATS302), a dc-motor actuator is driven by a motion controller and can be moved either continuously or stepwise with adjustable waiting time between steps.

The actual time resolution of a THz system is defined by a convolution of a laser pulse envelope and a response function of the THz detector and is about few tens of *fs*. The highest SNR reached in our spectrometers with EOS is at least 5000:1 for the THz-TDS system based on the amplified laser source when referencing the THz peak signal amplitude to the noise floor for when no signal is present and approximately 300:1 for the THz-TDS system using the Er: doped fiber laser source when referencing the THz peak signal amplitude to fluctuations in peak as observed through the lock-in amplifier.

The following Fig. 2.7a and Fig. 2.7b show the two terahertz time-domain systems we have in our lab. Notably, in Figure 2.7a, the thickness of the ZnTe crystal limited the scans to about $20\,ps$ after the main pulse in the time-domain due to the back reflection, resulting in a resolution in the frequency domain of $0.05 THz$. The overall usable bandwidth limited the measurements to frequencies from 0.4 to $2.4 THz$. All the experiments discussed in chapter 3-6 are based on either of the two systems.

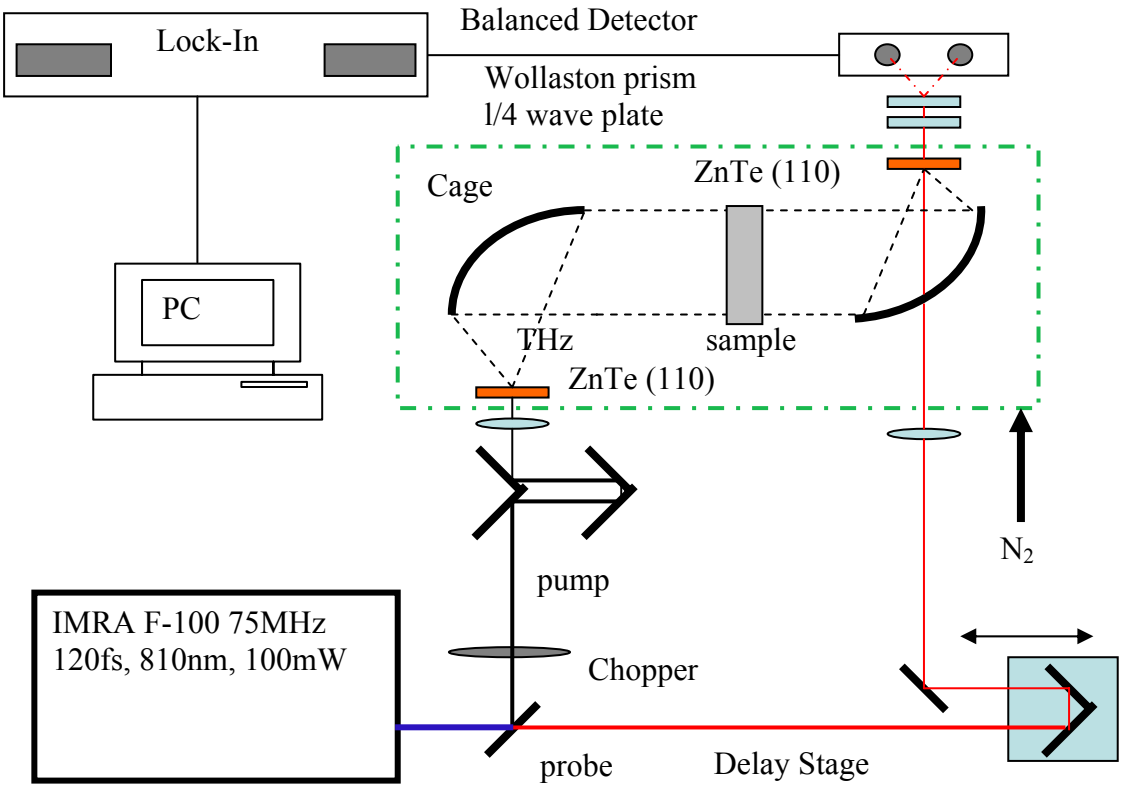

Figure 2.7a An Er: doped mode-lock fiber laser (IMRA Inc. F-100) is used as the source of the terahertz generation. The central wavelength is 810*nm*. A 1.5*mm* thick <110> ZnTe crystal is used for generating THz through optical rectification. [52,53,54,55] The THz beam is collected by two parabolic reflectors and focused collinearly with the probing beam on a second <110> 2*mm* thick ZnTe crystal. The terahertz electrical field is detected using electro-optic detection technique, where differential changes in the intensity between the orthogonal polarizations of the gating beam are detected with a balanced photo detector. The signal is measured with a lock-in amplifier referenced to a mechanical chopping frequency of 3.5 *KHz*. The THz beam path is enclosed in a cage to be nitrogen-purged to drive away water vapor for a reference signal.

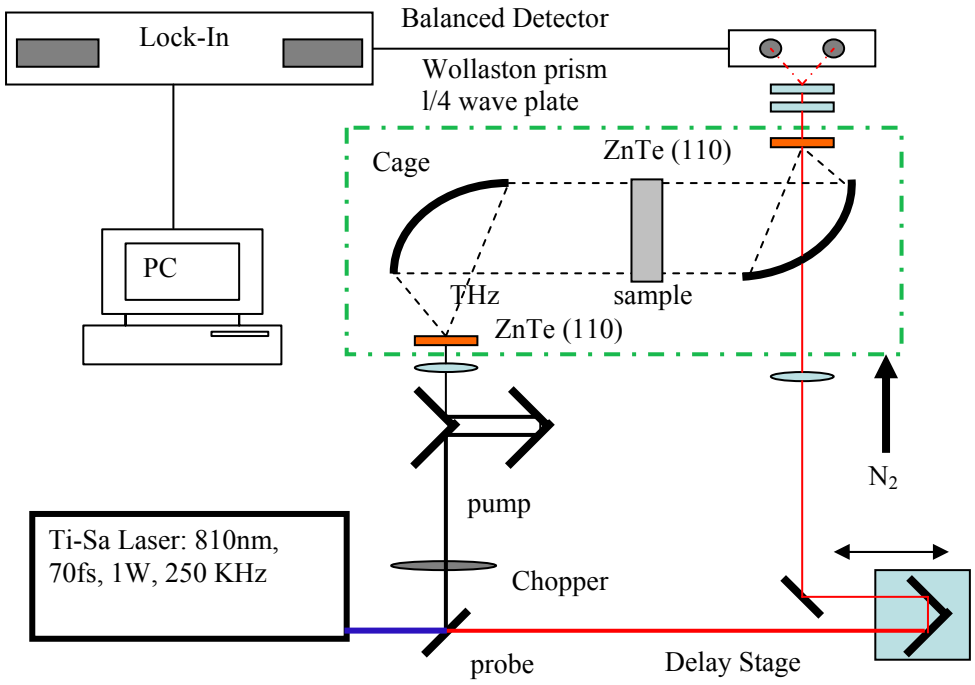

Figure 2.7b The Ti-Sapphire based THz laser spectrometer: ninety two percent of the power is used as a pump beam to generate the THz pulses via optical rectification in a ZnTe crystal. The remaining power was used to probe the THz signal with free-space electro-optic sampling. The emitter and sensor were 2.0-*mm*-thick <110> ZnTe crystals. A small hole (3*mm*-diameter) was drilled into the off-axis parabolic mirror, which allows for the collinear arrival of the probe and the THz pulse upon the sensor. The polarizations of the THz beam and optical probe beam were parallel to [1, -1, 0] crystal direction. The dynamic range is 8000:1. The optics was placed in an enclosure and purged with N_2 gas. In order to avoid complications from multiple reflections from the windows of the cell, the maximum recorded delay was limited to 46*ps* corresponding to 6912 data points by a scanning translation stage. This scan time gives a spectral resolution of about ±7 *GHz*.

Chapter-3 Liquid water and KCl solution at room temperature

3.1 Introduction

Water is one of the most important substances for the living things since it both supports and serves as an intermediary medium for biochemical reactions. Its isotopes possess unique properties, for example, the maximum density temperature for liquid water is 277.2*K*, for liquid heavy water it is 284.4*K*. [56] The structure of liquid water is always a complicated topic due to the presence of hydrogen bond. A water molecule can form up to four hydrogen bonds to other water molecules thereby creating the possibility for a local tetrahedral structure around the molecule. The intermolecular contribution to the IR absorption and Raman spectra is found in 0 -1000cm^{-1}. [57] This can be divided as libation region between 1000cm^{-1} and 300cm^{-1}, and as hindered translational bands below 300cm^{-1}. There is a strong absorption at ~180cm^{-1}, which are observed strongly in both Raman and FIR spectra. This band has been assigned to H-bond stretching/restricted translation. [58] Another band has been suggested at ~ 60cm^{-1}, which is weak in absorption and more easily observed in Raman spectroscopy [58] It has been assigned to H-bond bending/restricted translation. In previous studies,[59] two relaxation processes of liquid water are observed, one as 8*ps*, another one as 0.8*ps*, indicating two components of hydrogen bonds: strong hydrogen bond and relatively weak hydrogen bond that both exist in liquid water. The distribution in the two types of hydrogen bonds changes when the temperature changes. Studies also show that some ions act in similar function to temperature.[60] In point of this view, ions like Li^+,

F^- are considered to be structure makers; while others like K^+, Cl^- are considered to be structure breakers. Details on these arguments will be given in section 3.3.

3.2 Pure Liquid Water

In this experiment, we present the direct experimental determination of the torsional mode of liquid H_2O using THz-TDS in the frequency range 0.4 to 2.0*THz*. A torsional vibrational mode at 1.56 *THz* (~ $53cm^{-1}$) originating from the bending motion of the intermolecular hydrogen-bond coordinate was observed in the absorption spectrum. The low frequency mode may be the key mode to transfer information among and within cells in the body. Using the double Debye model,[61] the dielectric relaxation times were also determined in this study.

The THz-TDS system was used to obtain direct information about the low-frequency torsional modes. Details of the THz spectroscopy system were described in chapter 2 (Fig. 2.7b). The entire setup is placed in an airtight enclosure purged with dry nitrogen. A layer of water was adsorbed on the surface of a plastic plate (5-*cm*-diameter disc), then covered by another plastic plate to form a sandwich structure with a thin space of ~14μm. The terahertz beam passed perpendicularly through the sample.

To obtain the absorption coefficient of water, transmission measurements were performed. Figure 3.1 shows the time profiles of the THz pulses transmitted through the two pure plastic discs without H_2O (reference) and with the 14μm H_2O film between them. With this result the delay caused by the absorbed water is obtained as $\Delta t = 0.06 \pm 0.008ps$. The equivalent water layer thickness can be calculated as $L = c\Delta t$

$/ (n_b\text{-}1) = 14 \pm 2\ \mu m$, where c is the speed of light in vacuum and $n_b = 2.27$ is the index of refraction of bulk water at 1.0THz[31,62] This distance agrees well with the spacer used in the experiment.

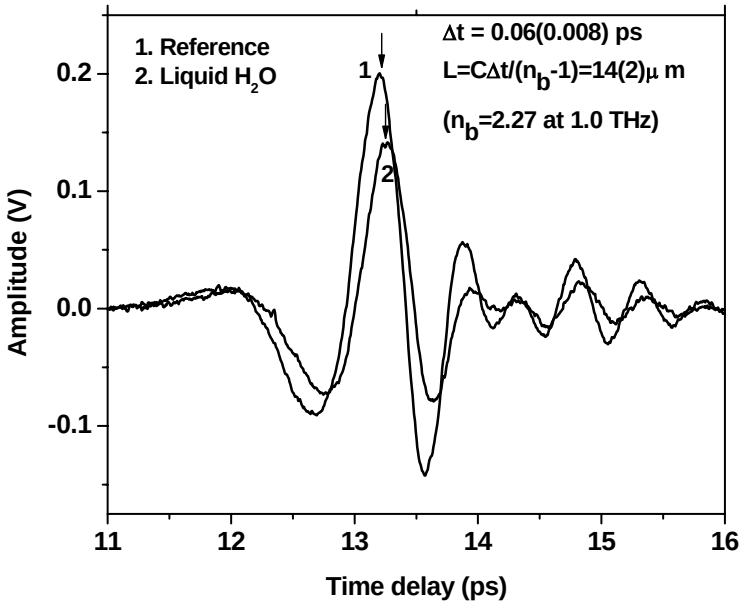

Figure 3.1 Time profiles of the THz pulses transmitted through the liquid H_2O sample and the empty cell.

Previous studies[63,64] showed that the frequency-dependent dielectric function of water $\hat{\varepsilon}(\omega)$ is characterized by a Double Debye model with a slow relaxation mode (τ_1) associated with the liquid structure and a fast relaxation mode (τ_2) associated with the water molecule orientations. The dielectric function can be described by the following relationship:

$$\hat{\varepsilon}(\omega) = \varepsilon_\infty + \frac{\varepsilon_s - \varepsilon_2}{1 + i\omega\tau_1} + \frac{\varepsilon_2 - \varepsilon_\infty}{1 + i\omega\tau_2} \quad \textbf{(3.1)}$$

where ε_S is the static dielectric constant, ε_∞ is the limiting value at high frequency, and ε_2 is an intermediate frequency limit. The relaxation strengths for the slow process is $(\tau_1) \propto (\varepsilon_S\text{-}\varepsilon_2)$ and for the fast process $(\tau_2) \propto (\varepsilon_2\text{-}\varepsilon_\infty)$. These relaxations involve translational and rotational diffusion, hydrogen bond rearrangement, and structural rearrangement processes. The processes are associated with different activation energies and may have significant temperature dependence. Water molecules form a network of tetrahedral structures (a water "cage"). Using THz pulses, the cage dynamics can be probed for water molecule reorientation rates. In a slow process, four hydrogen bonds break in the approximate time τ_1. Afterward, in a fast process, a single water molecule reorients and moves in time τ_2 to form a new tetrahedral site.[65]

The frequency-dependent dielectric response $\hat{\varepsilon}(\omega)$ can be described by the general relationship:

$$\hat{\varepsilon}(\omega) = \varepsilon'(\omega) + i\varepsilon''(\omega) = [n(\omega) - ik(\omega)]^2 \quad \textbf{(3.2)}$$

where $k(\omega) = c\alpha(\omega) / 2\omega$, $\varepsilon'(\omega)$ and $\varepsilon''(\omega)$ are the real and imaginary parts of the dielectric constant respectively, and $\alpha(\omega)$ is the power absorption coefficient. Given the measured index data and the power absorption spectrum shown in Fig.3.2 (b), the

real part ε' and the imaginary part $\varepsilon''$of the dielectric constant as a function of frequency can be obtained using Eq. (3.2). For value of ε_S ~78.4, ε_2 ~ 4.2, and ε_∞~3.5, we fitted Eq. (3.1) to the data using the least-squares method. This yields the double Debye parameters as τ_1~ 9*ps* and τ_2~ 0.2*ps*, respectively. These parameters are in good agreement with the published documents on this.

Figures 3.2a and 3.2b show the refractive index and the power absorption spectrum of liquid H_2O in the frequency range from 0.4 to 2.0*THz* (13.3 to 66.7cm^{-1}). Some known refractive indices of liquid H_2O are also plotted in Fig.3.2a for comparison. An absorption peak associated with torsional motion of liquid water molecules was observed at 1.56 *THz* (53 cm^{-1}).

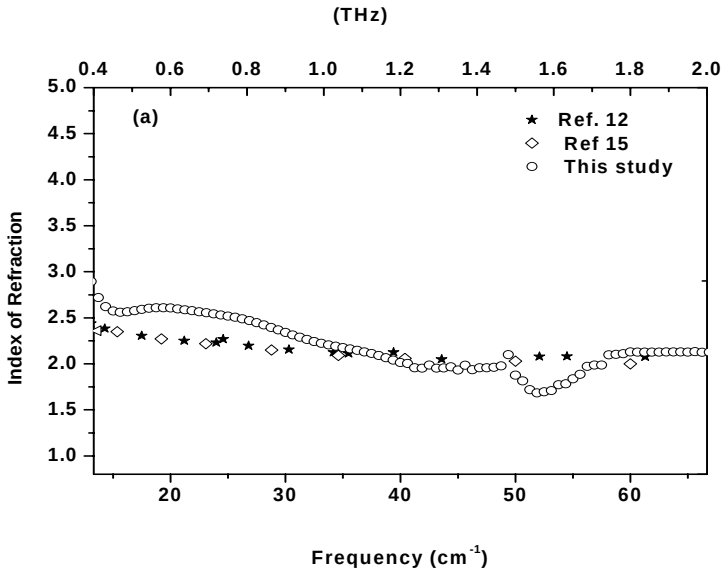

Figure 3.2 (a) Index of refraction of the liquid H_2O in THz region

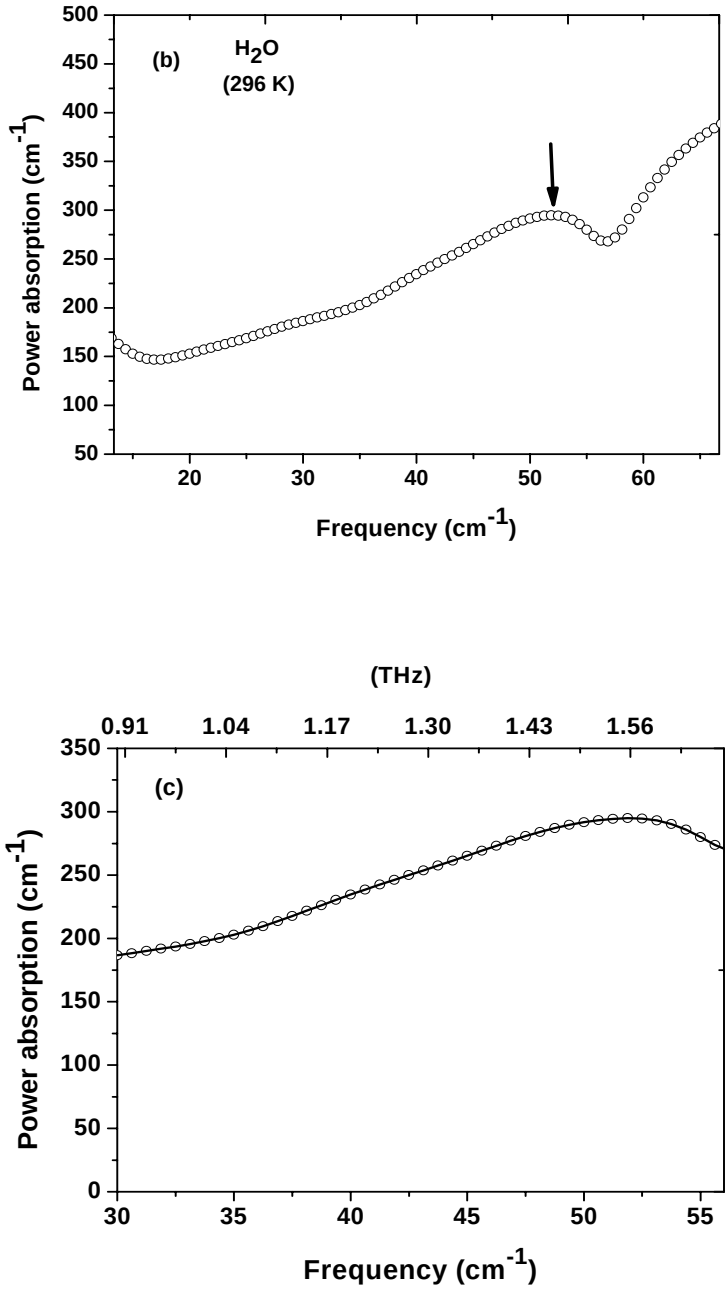

Figure 3.2-Continued (b) Power absorption vs. frequency (ν) of liquid H_2O in the THz region. Arrow denotes the location of the low frequency mode. (c) Fit (solid) to experimental data (dots) of the torsional mode at 1.56 *THz* ($53cm^{-1}$)

This mode has been previously observed using tunable FIR laser spectroscopy[66] and Fourier transform spectroscopy[67] which correlates with Raman measurements (~ 60 cm^{-1}). The size of the absorption coefficient is in agreement with that reported in Ref. 58 at 50cm^{-1}. As can be seen in Fig. 3.2(b), there is a small bump at ~45cm^{-1}. Due to the fluctuations in the THz time domain profile as a result of laser fluctuations between sample and reference scans, there may be small oscillations which appear in the frequency spectrum such as this feature at ~45cm^{-1}. We can only rule out absorption features that are clearly distinguishable from these small oscillations. The continuous curve shown in Fig.3.2 (c) represents the best fit to the data for this mode (53 cm^{-1}) using the following Gaussian oscillator:

$$\alpha(\nu) = \alpha_{CC}(\nu) + C_S \exp[-(\nu - \nu_S)^2 / \gamma_S^2] \qquad \textbf{(3.3)}$$

where $\alpha_{CC}(\nu)$ is the *Cole-Cole* factor, ν_S is the oscillator frequency, γ_S is the damping term, and C_S the oscillator strength. The best-fit values to data for these parameters were ν_S=1.56THz (~ 53 cm^{-1}), γ_S = 0.43THz (14.3cm^{-1}), α_{CC} = 187cm^{-1}, and C_S =114 cm^{-1}.

For a fully tetrahedral hydrogen bond structure of water, there are nine intermolecular vibrations; six refer to restricted translations and three to restricted rotations.[68] Two of the six restricted translations are equivalent to the hydrogen bond bending motion. The O–H···O bending vibrations ν_3A_1 and ν_4A_1 occur at ~60cm^{-1}.

These modes correspond to the $53cm^{-1}$ mode shown in Fig. 3.2 (b). The O-H···O stretching vibrations $\nu_1 A_1$, $\nu_2 A_1$, $\nu_7 B_1$, and $\nu_9 B_2$ at ~$170cm^{-1}$ are beyond our frequency detection range.

In summary, the far-infrared absorption properties of liquid H_2O using THz-TDS were measured. An absorption peak was observed at $1.56THz$ ($53cm^{-1}$), which is attributed to the torsional hydrogen bond bending motion in the liquid H_2O cage. The absorption and index of refraction curves are described by the double Debye dielectric model to yield the low-frequency dielectric ($0.4 – 2.0THz$) relaxation time of ~ $0.2ps$ (fast) and ~ $9ps$ (slow). This study has important implications for the potential of THz-TDS spectroscopy to provide information on how low frequency modes may transfer energy among hydrogen bonds in biological molecules.

3.2 The Effect of K^+, Cl^- Ions on the Hydrogen Bond Network in Liquid Water at Room Temperature

3.2.1 The Mixture Model for Hydrogen Bond Network in Liquid Water

When a photon of energy $h\nu$ (e.g. THz frequency) equivalent to the difference of two rotational energy levels in a molecule is absorbed, the molecular energy state, also described as certain vibration or rotational motions, will change; afterward, the energy is released and some low energy photons (i.e. microwaves) are reradiated. As for the dipole moments, the dipole relaxation after the original electric field causes the reradiated electric field out of phase from the original electric field due to the collisions, this verifies as different oscillation tails (ringing) after the main pulse.

In liquid water, which has permanent dipole moment, the THz absorption is mainly caused by the induced intermolecular dipole moments due to the existence of hydrogen bond in liquid water. Basically, there are two species of water molecules in liquid water, strongly hydrogen bonded and weakly hydrogen bonded molecules: structured and non/less-structured molecules. For example, the broad, weak absorption band at $60cm^{-1}$ is due to the hydrogen bond bending motions (restricted translational region, another one is around $170cm^{-1}$, stretching motion) in the five-molecule structure treatment. (for ice, this occurs in the vicinity of $65cm^{-1}$). When temperature elevates, corresponding to the hydrogen bond lengthening or softening, there is a structural breakdown and the band intensity decreases accompanying with the red shift of the band. Recently, a $70cm^{-1}$ mode has been found in Raman experiments. The origin of this mode has been attributed to a secondary, weaker hydrogen-bonding environment that exists in liquid water, which differs from the tetrahedral bonding arrangement. It has been suggested that this mode increases in strength with temperature. In addition, VRT (vibrational rotational tunneling) spectroscopy measurements have identified some low frequency torsional motions involving the flipping of free hydrogen atoms in separated water clusters. [69,70] This also suggests that in liquid water weaker hydrogen bonded structure exists thus a large percent of ring like structures: dimer, trimer, and quadromer may contribute to the absorption in bulk water.

This also agrees with the *mixture model* of hydrogen bond network in liquid water proposed by earlier researchers: there is equilibrium between two or more types

of water molecules corresponding roughly to a transition from a hydrogen-bonded species to a non-hydrogen-bonded one as temperature is increased.

The broadband absorption is affected by mode frequencies, which are composed of strong tetrahedral structure, and non-mode/weak frequencies connected to the weak structures, such as monomers, dimmers, trimers, quadromers, etc., (Fig.3.3). The distribution among structured and non/weak-structured water molecules will change when temperature change or certain ions are added since the hydrogen bond is weakened as temperature increases or 'structure breaker' ions are added, and the mode frequencies will shift to the lower frequencies with less absorption intensity

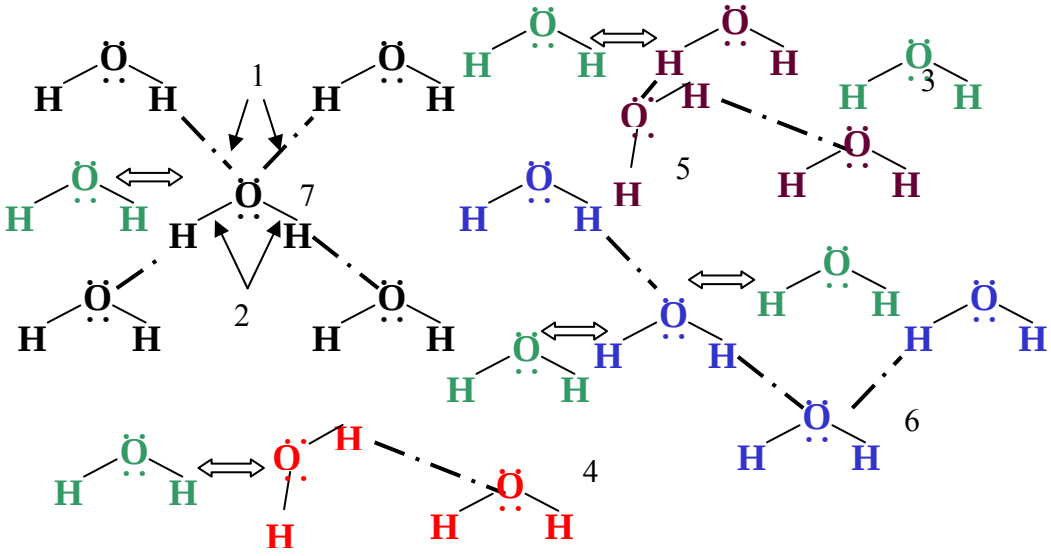

1- Hydrogen bonds 2-Covalent bonds 3-Monomer 4- dimer 5- trimer
6-quadromer 7-tetrahedral structure

Figure 3.3 The diagram of *mixture model* for hydrogen bond network in liquid water, the water molecules constantly exchange within neighboring area.

due to the breakdown of the structure. On the other hand more non/weak-structured water molecules will be available to contribute to the non-band parts of the broadband absorption, elevating the absorption levels at these frequencies.

For qualitative understanding of this scheme, we give a simple mathematic model as:

$$\mathrm{H}(T) = \sum_{i=1}^{n} h_i(T) \tag{3.4}$$

with n = 1, 2, 3, 4, 5…representing water monomer, dimer, trimer, quadromer and tetrahedral structure etc.; $h_i(T)$ represents the change of amount of *ith* structrue of water molecules as a function of temperature. To demonstrate the significance of certain structure of water molecules, the following formula helps:

$$\mathrm{M}_i(T) = \frac{h_i(T)}{\mathrm{H}(T)} \tag{3.5}$$

with $M_i(T)$ indicating the significance of *ith* species water molecules, and $H(T)$ representing all the water molecules. As for the absorption mode observed, i.e. at $60cm^{-1}$, the fraction of molecules involved in 5-molecule structure must be larger than the rest such that this mode is prevalent over others.

As temperature increases, some intermolecular bands deflate into a slight bump in the room temperature absorption spectrum and some even completely disappear. At room temperature, the ~$55cm^{-1}$ mode found at 269K is slightly red shifted to lower frequency and appears at ~$49cm^{-1}$. [71] Similar to the above situation of increasing the temperature, when some “structure breaker” ions are added to the liquid water, one will obtain a similar result. This is because the band will be red shifted, reducing

absorption intensity, and a corresponding increase in absorption in the rest region of frequency region, due to the increased amount of the free/weak structured water molecules.

Due to the observed similarities in the effect of temperature and addition of some solutes upon the absorption band of water, it is possible for the ions to be classified as "structure breakers" or "structure makers".[72] The far-infrared work of Draegert and Williams[73] suggest that Li^+ and F^- should be taken as structure makers while Na+ and K^+ are structure breakers. Cl^- is considered to be a strong structure breaker. In addition, Frank *et al* have postulated a model[74,75] for aqueous solutions in which there are three main regions about an ion: an innermost region of less mobile water molecules, an outer region containing water molecules with normal liquid structure, and an intermediate structure region where the normal tetrahedral structure-orienting competes with the influence of the bulk water. This concept helps researchers classify ions based on their capabilities of either improving structure ("structure makers") by enhancing the inner/outer regions, or breaking structure ("structure breakers") by establishing the intermediate region about the ion the more important. Here, for the "structure breakers", one can say the ions will make the structured water molecules more mobile. As for structure makers/breakers, the Equation (3.4), (3.5) can be used to describe the effect of ions on the structure of liquid water.

Structure makers affect the existing strong hydrogen bonded structure, e.g. 5-molecule structure by shifting the mode frequencies, at the same time increasing the

number of amount of the fractional structures: more “free” like molecules. Correspondingly, for example, a red shift of mode frequency will cause less absorption in non-mode frequencies or base level absorption. However, due to the broadband nature of the absorption from intermolecular interactions within h-bond network, it is difficult to tell the shift of the band location in our limited THz window (0.2-2.2THz) when ions are added.

Interestingly, at room temperature, D_2O behaves like some structure makers in terms of the strength of hydrogen bond.[76] The OH stretching vibration band shifts to lower frequency compared to that of H_2O, this means that the D-bonding in D_2O is stronger than that in H_2O since it is well known that OH stretching frequency decreases with increasing D-bonding strength.[77] In certain cases the changes in temperature and the addition of sugar to pure water cause similar spectral changes.

Experimental results from our recent measurements are presented in Fig. 3.4 and Fig. 3.5. In Fig. 3.4a, the absorption level from 0.5*M* KCl solutions is above that from pure liquid water. This is due to the fact that both K^+ and Cl^- are considered to be strong “structure breakers”. They affect the hydrogen bond network by breaking the bond to destroy the structure, making more “free” like water molecules available such that the absorption mode from the ring structures weaker or even disappear, while at the same time the absorption level increases. This measurement was done using the amplified Ti: Sapphire based THz-TDS system. It is important to note that the small bumps seen in Figure 3.4a and Figure 3.5b are due to the fluctuations in the laser source as was discussed earlier.

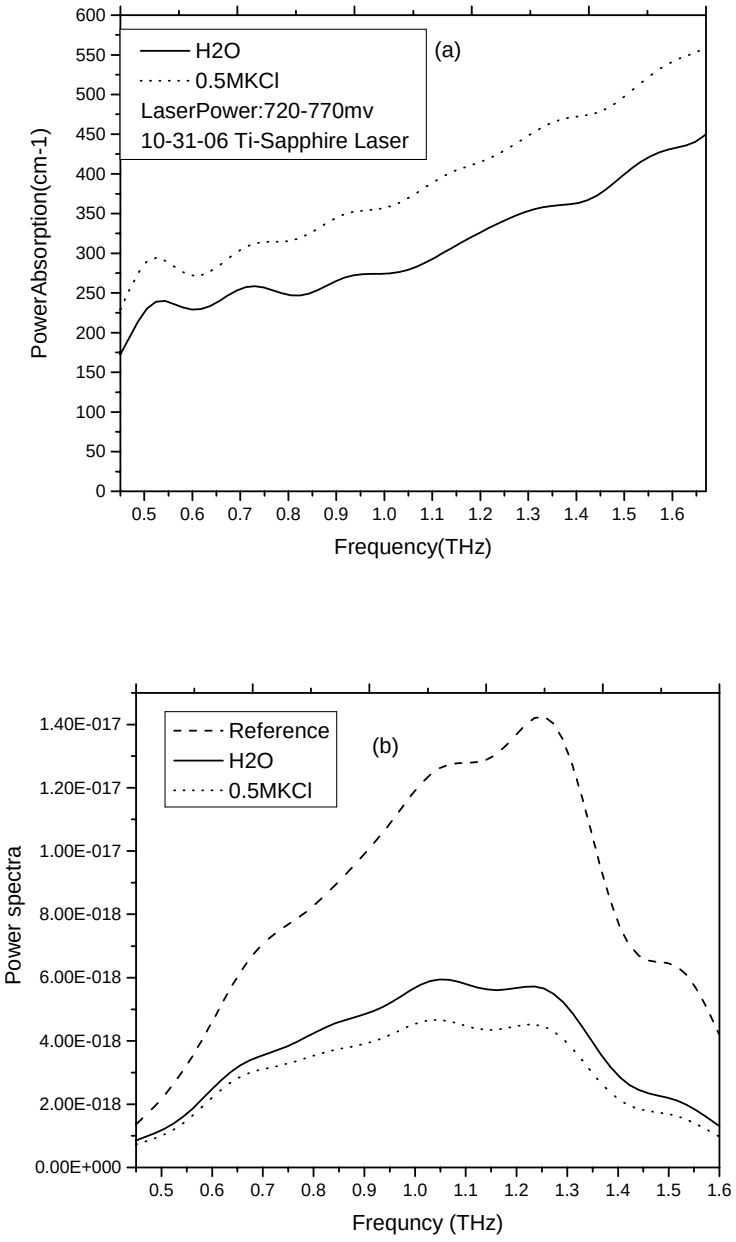

Figure 3.4 (a) The power absorption coefficient in pure liquid water and 0.5*M* KCl solution; (b)The power spectra of pure liquid water, 0.5*M* KCl solution and empty cell

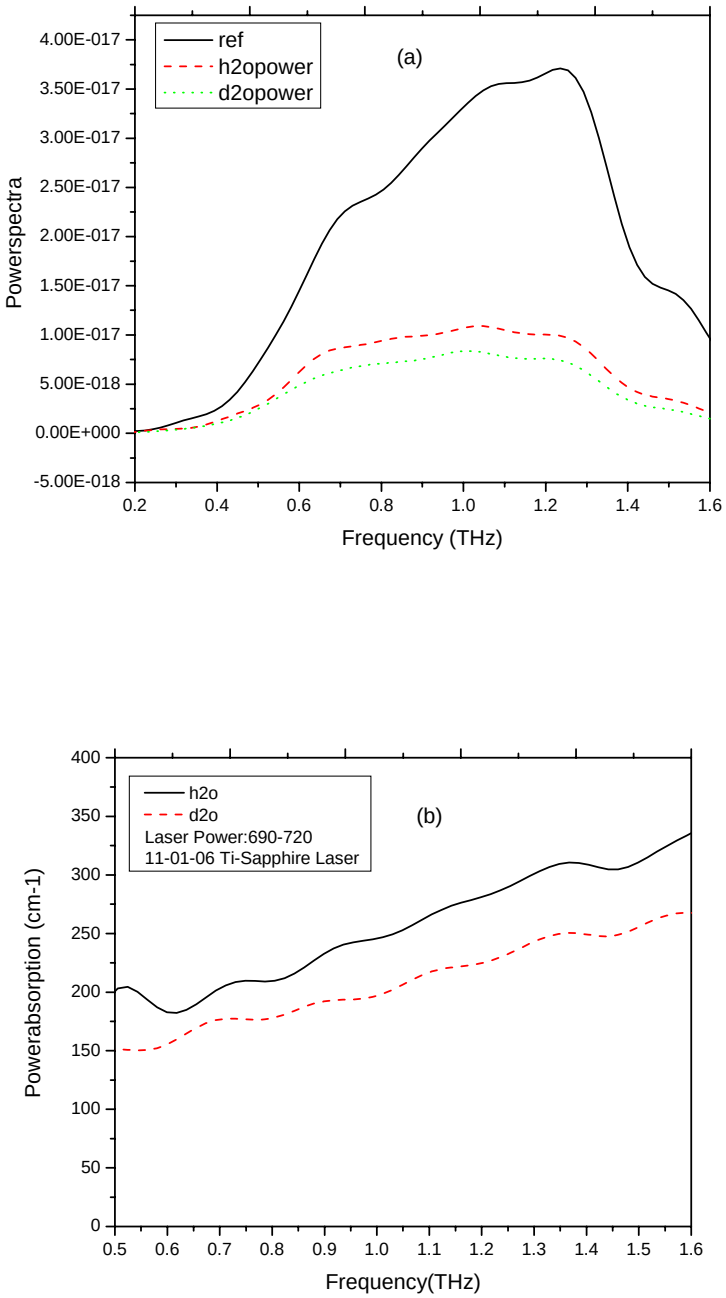

Figure 3.5 (a) The power spectra of pure liquid water, heavy water (D_2O) and empty cell (b) the power absorption coefficient in pure liquid water and heavy water (D_2O)

In Fig. 3.5a, the D_2O shows more overall absorption than H_2O. The explanation for this result is based on the idea given earlier in this section: D_2O behaves like "structure makers" due to its stronger hydrogen bond than that in H_2O since Deuterium (D) has twice mass as that Hydrogen (H) has. This measurement was taken with the compact THz system, which is driven by the Er: doped mode locked fiber laser. A $5\mu m$ quartz cell was used to hold the liquid samples.

3.2.2 Far Infrared Cells

Crystal quartz can be used in transmission measurements for wavelengths between 50 and $1000\mu m$, although some slight wedging of windows is necessary to reduce interference effects due to its high reflectivity. Polyethylene has some attractive features such as high transparency over a wide wavelength range and low cost; however, certain mechanical disadvantages and uncertainty in absorption characteristics as a function of temperature reduce its usefulness for quantitative analysis. The use of short path lengths in infrared studies contributes largely to the difficulty in obtaining quantitative information from absorption bands. Techniques have been developed for preparing thin cells of known thickness below $0.002mm$ and these provide some acceptable basis for quantitative studies.

In our study, we used $100\mu m$ quartz cells to measure the index of refraction of the liquids by using the Erbium doped fiber laser based terahertz spectrometer. According to the relationship $L=c\Delta t/(n-1)$, if the thickness of the liquid sample is known, its index of refraction can be calculated by measuring the relative shift

between the two time-domain THz signal profiles: empty cell and the cell filled with liquid sample. In Figure 3.6, the shift between the reference and liquid water, 0.5M KCl solution are

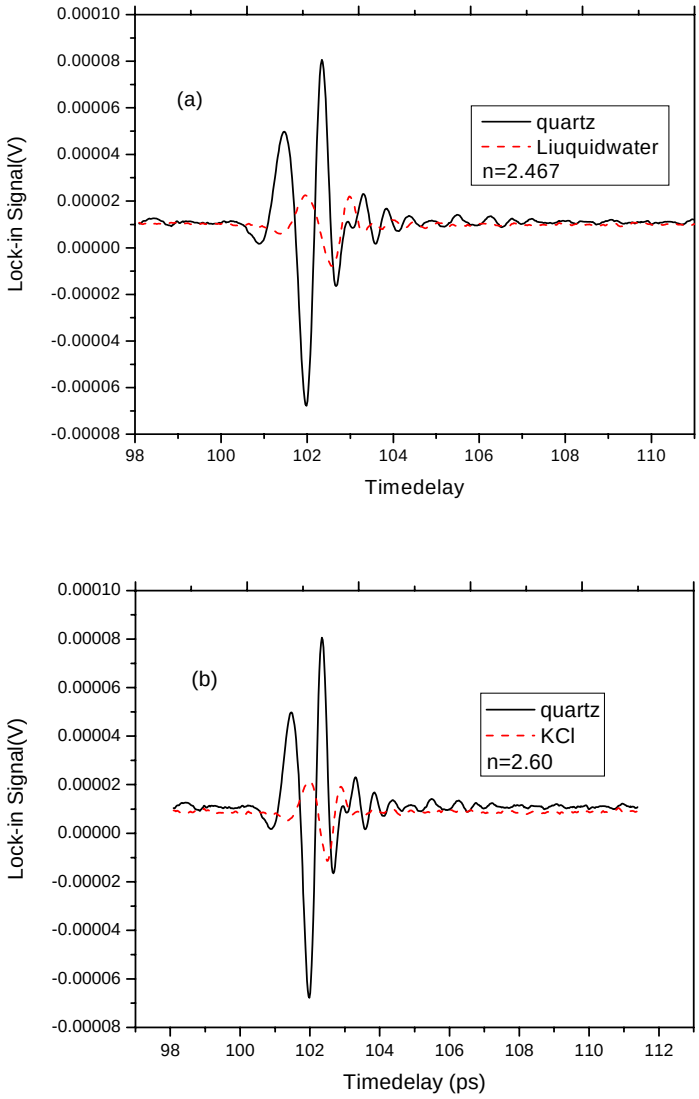

Figure 3.6 (a) The phase shift between the empty quartz cell (solid line) and the cell filled with liquid water (dashed line); (b) The phase shift between the empty quartz cell (solid line) and the cell filled with 0.5M KCl solution (dashed line)

~0.49ps and ~ 0.53ps respectively, such that the corresponding index of refraction for the two liquids are: 2.467 and 2.60 respectively.

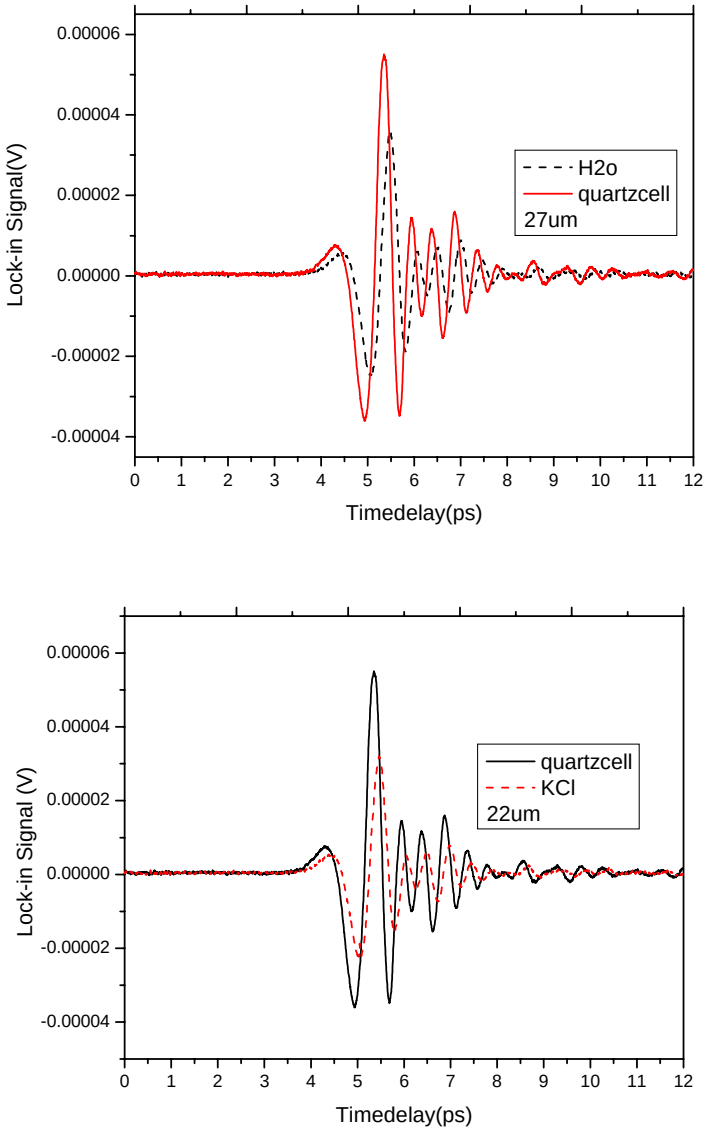

Figure 3.7 (a) The phase shift between the empty plastic cell (solid line) and the cell filled with liquid water (dashed line); (b) The phase shift between the empty plastic cell (solid line) and the cell filled with 0.5M KCl solution (dashed line)

The measurements were repeated with the Ti-sapphire based terahertz spectrometer, where a plastic cell is used to form thin liquid films because the polyethylene has similar index of refraction and better transmit terahertz beam than quartz. Using the relationship $L=c\Delta t/(n-1)$, with measured phase shift in time-domain as known values (~0.137ps and ~0.117ps for liquid water and 0.5M KCl solution respectively) and the measured index of refraction in Fig. 3.6, the thickness of the two liquid samples are calculated as: 27μm and 22μm (Fig. 3.7). Using this method, the measured index of refraction and thickness are: 2.60μm and 70μm for D_2O.

Chapter4- H_2O and D_2O vapors at room temperature

4.1 Terahertz Absorption Spectrum of *para* and *ortho* Water Vapors at Different Humidities at Room Temperature

Over the past two decades, the water vapor absorption spectrum in the low terahertz frequency range has been investigated at fixed relative humidity by using time-resolved THz spectroscopy.[13, 24] The observed absorption profile is primarily due to molecular rotational transitions in the vibrational ground or excited states. From the detailed study of individual rotational transitions, it is possible to extract various properties including parameters such as the molecular structure and rotational constants, these time-resolved terahertz studies often use sophisticated techniques to accurately measure each individual transition, which can be better observed using narrowband terahertz methods that have higher frequency resolution. The advantage of a broadband technique like time-resolved THz spectroscopy is that the entire spectrum of the absorbing species can be analyzed at once.

Traditionally, the absorption profile for water vapor is derived from Beer's Law, which states that the absorption cross-section per molecule is independent of intensity of the incident radiation or the concentration of the absorbing species. However, at high concentrations the absorption by a molecule is no longer independent of the surrounding molecules. For powerful sources, the absorption cross-section per molecule is not independent of the intensity due to the nonlinear effects. In contrast, the absorbance is linearly dependent on the concentration of the absorbing

species. Thus for increasing concentrations the absorption cross-section per molecule should remain constant while the absorbance should increase. Furthermore, the absorption cross-section for H_2O vapor depends non-linearly on pressure and temperature leading to an absorption profile that can skew from a Beer-Lambert model with respect to environmental conditions. The lifetime of the rotational transient of water molecules is related to the full width of half maximum linewidths, Δv, of the water absorption lines by: $\tau = 1/\Delta v \times \pi$. The lifetimes for the sixteen absorption modes of water vapor observed at room temperature are from ~94ps to ~160ps. [24] These lifetimes are longer than THz pulse of 1ps and shorter than the laser repetition rates of 75 MHz/ ~12ns for IMRA F-100 and 250KHz / ~ 4μs, indicating that it is proper to use THz pulse to investigate the rotational dynamics of water molecules.

The absorption for water vapor is further complicated since it is a mixture of two components, *para-H_2O* and *ortho-H_2O* when considering the nuclear spin effect of hydrogen atoms in water molecule, which results in an *ortho* to *para* ratio (OPR) of 3 : 1 Previous studies on water vapor have shown that due to the non-rotational ground state of *para* water, solid surfaces will have preferential adsorption of *para* water.[78] Consequently, the *ortho* to *para* monomer population ratio will not remain 3:1. Adsorptions of *para* water onto solid surfaces, as well as interactions amongst water monomers themselves (dimer formation and clustering) and with liquid water droplets for highly saturated environments have all been shown to decrease the absorption intensity[79]. In this work, the absorption profile of water vapor was

measured using THz time-domain spectroscopy in the frequency range from 0.4 to 2.4*THz* with increasing relative humidity. The unexpected decrease in absorption intensity for *ortho* rotational transitions with increasing concentration is attributed to the interactions between monomers, dimers and clusters in the terahertz beam path.

The design of the THz-TDS system used in our measurements has been discussed previously (Fig. 2.7a, b).

Various quantities of 99.5% pure, drinking water were evaporated inside the cage to reach desired humidity levels of 15%, 30%, 50%, 70% and 90% with an accuracy of ±5%. All measurements were performed at an ambient temperature of 296K ±2K. The humidity was measured by using a hygrometer with an accuracy of 0.1% in 0%-100% range.

All measurements were referenced to the dry nitrogen purged cage. We plot the water vapor absorption profile vs. frequency for different levels of humidity in Figure 4.1. The concentration independent absorption profile was calculated using the formula: $\alpha(\nu) = (-1/d) \times \log(I_t / I_0)$ where α is the absorption coefficient, d is the terahertz path length in the sample, I_t is the transmitted terahertz power and I_0 is the reference power. In Figure 4.1, as humidity increases from 15% to 90%, the absorption intensity of most *para* transitions increase, while most *ortho* transitions increase and then decrease. Figure 4.2 shows how the absorption of *para* transitions and *ortho* transition changes with increasing humidity from the measured absorption profiles.

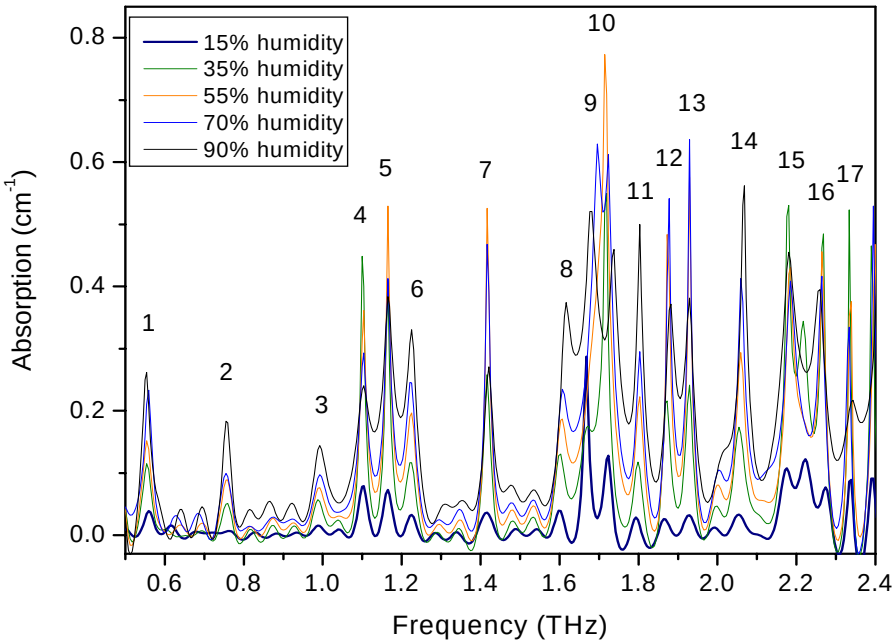

Figure 4.1 Water vapor absorption profiles at different humidity at room temperature.

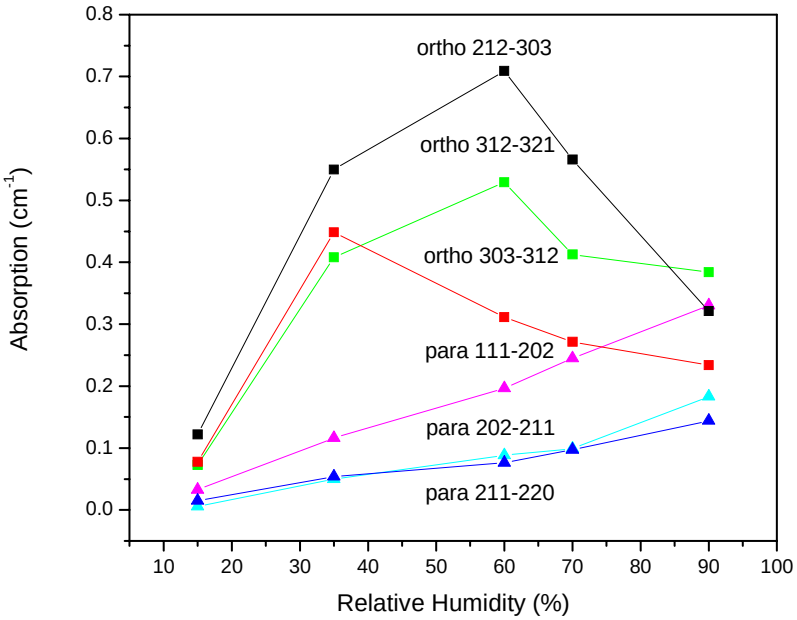

Figure 4.2 The peak intensity of three *Para* (triangles) and three *Ortho* (squares) rotational transitions for different humidity. While Para transitions increase, *Ortho* transitions increase and then decrease with increasing humidity.

The description for each rotational transition observed is given in Table 4.1.

Table 4.1 Rotational Transitions in H_2O vapor from 0.2-2.4 THz (Fig. 4.1)[1]

Number	Frequency (THz)	Low state	High state	$EB_{LB}(cmP^{-1P})$	Type of Transition
1	0.557	101	110	23.794	*Ortho*
2	0.753	202	211	70.091	*Para*
3	0.989	111	202	37.137	*Para*
4	1.098	303	312	136.76	*Ortho*
5	1.164	312	321	173.365	*Ortho*
6	1.2264	211	220	95.176	*Para*
7	1.4116	514	523	399.457	*Ortho*
8	1.603	404	413	222.052	*Para*
9	1.67107	101	212	23.794	*Ortho*
10	1.718	212	303	79.496	*Ortho*
11	1.7984	725	734	782.410	*Ortho*
12	1.869	523	532	446.511	*Ortho*
13	19207	313	322	142.278	*Para*
14	2.0759	322	413	206.301	*Para*
15	2.2644	414	423	224.838	*Ortho*
16	2.3459	716	725	704.214	*Ortho*
17	2.3932	313	404	142.278	*Para*

Water molecule, like H_2, has two orientations for the hydrogen atom nuclear spins-parallel (total spin I = 1, an *ortho* molecule) or antiparallel (I = 0, a *para*

[1] International Tables of Selected Constants 19- *Water vapor line parameters from microwave to medium infrared*, by J.-M.Flaud, C.Camy-Peyret and R.A. Toth.

molecule). Correspondingly, it has two different types of rotational energy levels in Figure 4.3.

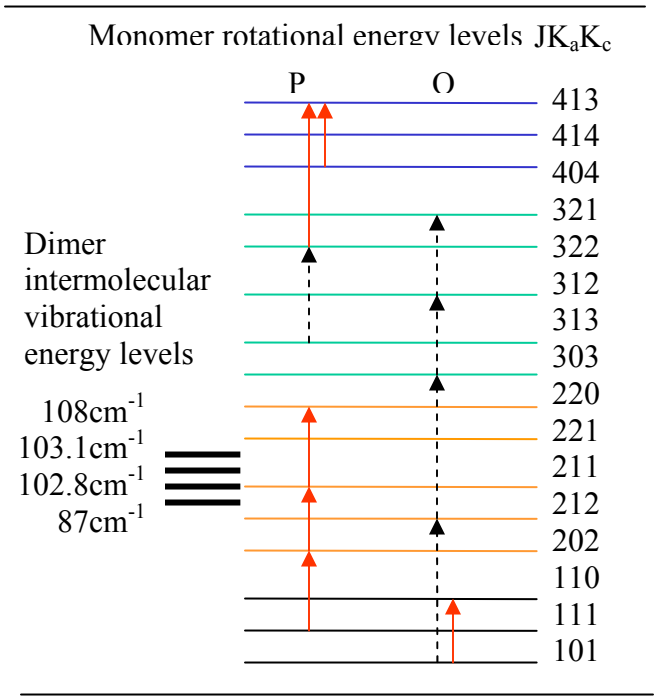

Figure 4.3 Water monomer energy level diagram depicting both *ortho* and *para* transitions. Also shown are the water dimer intermolecular vibrational energy levels. Interactions between dimers and monomers as well as monomers themselves can change their populations among the energy levels. Solid lines represent that the absorption increases as humidity increases. Dashed lines represent that the absorption increases and then decreases as humidity increases.

The difference in I brings in a nuclear spin statistical weight $2I+1$ of the *ortho* levels that is three times larger than that of the *para* levels. As a result, at the high temperature ($> 50K$), the equilibrium *ortho* to *para* ratio (OPR) is 3:1. The two types of water molecules are readily separable due to the fact that the mutual conversion upon collision of molecules and radiative transitions between them is forbidden by

quantum mechanics.[80] Only *para* water molecules can reach the ground rotational level with a zero-point rotational energy, which means that the molecule is not rotating. This makes the energy of interaction with solid surface maximal so that the molecule will be most likely adsorbed by solid surfaces. While all *ortho* molecules have non-zero rotational energies, for them, the energy of interaction with the surface is lower due to the rotation, so is the attraction.[81] Because the ground state is non-rotational, the *para* molecules have the most chance to be trapped by the solid surfaces e.g. aluminum surfaces of the mirrors we use in the setup. The result is that most of the molecules left in the pathway of terahertz beam are *ortho* water molecules.

The monomers in the predominantly *ortho* vapor undergo interactions with themselves either as in collisions or formation of hydrogen bonds with neighboring molecules. Two water monomers can interact to form one dimer molecule by hydrogen bonding as a result of the polarity of each molecule; the positive regions in one water molecule will attract the negatively charged regions of the neighboring molecules. Dimer formation is generally governed by the following rate equation:[82]

$$M + M + M \underset{k_R}{\overset{k_F}{\rightleftarrows}} D + M \qquad \textbf{(4.1)}$$

where, M stands for monomers and D for dimers formed. The rate of reaction is given by the forward rate constant (k_F). As humidity increases at room temperature, we expect more dimers to form due to the close proximity among molecules.[83,84,85] The study of thermal conductivity of water dimerization in water vapor shows that water dimer has binding energy of $-5.2 kcal/mol$.[86] The strength of this hydrogen bond is

strong enough to withstand room temperature, allowing for significant concentration of water dimers to exist (e.g. 10^{16} *dimers/cm*^{3} at $40°C$ and 100% humidity), and can contribute significantly to the absorption of sunlight and atmospheric reaction kinetics[87] From these investigations we predict that the maximum concentration of water dimer in our measurements is around 2.5% of the total monomer concentration at 90% relative humidity. At room temperature we expect a majority of the molecules to lie in states with rotational quantum number $J < 4$ with respect to the Boltzmann distribution. Near these energies, water dimers have well documented intermolecular vibrational modes,[88] which can be excited due to collisional energy exchanges between monomers in predominantly *ortho* levels. These levels are depicted in Figure 4.3. Collisions between monomers can also redistribute populations among monomer energy levels. From Table 4.1, the majority of the *ortho* level transitions, which decrease in absorption intensity, are between consecutive levels. Collisions will in turn excite the population to move up the ladder, thereby causing a decrease in the observed absorption intensity for *ortho* level transitions.

Both collisions between dimers and monomers and monomers themselves as well as dimer formation rates are insufficient to explain the observed decrease in the *ortho* rotational absorption strengths. To model the absorption strength decrease as seen in our measurements we assumed a bi-molecular interaction where the energy exchanges were governed by the *ortho* to *para* population ratio. Among *ortho* water molecules, over 40% of water monomers have to be involved in some sort of bi-molecular interaction such as dimer formation, far above the predicted concentration

of 2.5%, and much larger than can be expected assuming standard collision theories of molecules in a gas at room temperature.

For high water vapor concentrations condensation and nucleation can occur on all solid surfaces. In these highly saturated environments, the water molecules can form droplets surrounded by the vapor, whereby interactions between water molecules in the vapor and liquid states can lead to decrease in the observed absorption profile of water vapor. In these simulations the water molecules were classified into 'liquid', 'surface', or 'vapor' with respect to the number of neighbor molecules. Thus most of the vapor absorption dominated by *ortho* transitions will dramatically decrease once 'liquid' and 'surface' molecules are formed in or around the THz beam path. While bi-molecular interactions are an important factor, we believe that interactions between water monomers in the vapor phase with neighboring molecules in the liquid and surface states is the primary effect for our observation on the decrease of *ortho* transitions with increasing humidity.

In summary, the water vapor absorption in 0.2-2.4*THz* was measured at different humidities at room temperature by using time-domain terahertz spectroscopy. The experimental results show that water molecules that undergo *ortho* level rotational transitions increase then decrease in absorption strength with increasing humidity, while most *para* transitions simply increase as expected for higher concentrations in the THz beam path. In terms of nuclear spin statistics, the *ortho* levels possess populations three times larger than the *para* levels at room temperature due to the

presence of two symmetric hydrogen nuclei. Furthermore, *para-H_2O* adsorbs onto aluminum and silica surfaces preferentially due to its non-rotational ground state. The condensation of *para* molecules results in an abundance of *ortho-H_2O*. At higher humidity levels, *ortho* molecules are involved in interactions between neighboring molecules more so than *para* molecules. These interactions can be explained by dimerization and energy-coupling processes between dimers and monomers; however the dominant interaction that contributes to the decrease in absorption of *ortho* level transitions arises from interactions between molecules in the vapor phase which coalesce around liquid droplets either in the terahertz beam path or on surfaces. dimerization, energy coupling between dimers and monomers, collisional energy exchanges between consecutive energy levels of the same flavor and most importantly interactions between molecules in liquid and vapor phase can all contribute to the observed decrease in the absorption intensity of *ortho* level transitions.

4.2 D_2O Vapor

Heavy water (D_2O) is important for many applications in the nuclear field. Deuterium (D) is an isotope of hydrogen, which contains one proton and one neutron. D_2O is naturally present in water at a low concentration of about 1 part in 5,000. Heavy water is one of the two principal moderators, which allow a nuclear reactor to operate with natural uranium as its fuel. Studies with D_2O have shown large isotope effects with some properties, such as the temperature of maximum density occurring at ~277*K* for liquid H_2O and ~284.4*K* for liquid D_2O, while other properties, such as the static

dielectric constant, showing little difference for the two isotopes.[89,90,91,63] Liquid H_2O and D_2O are perhaps the most studied chemical systems using various experimental and theoretical methods in most of the electromagnetic spectral region from the UV to the far-infrared (FIR). The Debye relaxation time for both D_2O and H_2O liquids at $300K$ is ~ 7.5 ps. The main vibrational modes of D_2O are denoted by ν_1 (100), ν_2 (010) and ν_3 (001) modes. The infrared spectrum of D_2O molecule gives three strong bands at 2671.46, 1178.7, and 2788.05 cm^{-1}, which are associated with ν_1, ν_2 and ν_3, respectively[92] The absorption lines of D_2O in 700 to 7000 cm^{-1} have been assigned to the overtones of ν_1, ν_2, and ν_3.[93,94] Although the far-infrared absorption spectra of D_2O vapor have been studied by microwave techniques[95] and the Berkeley terahertz laser sideband spectrometer[96] the absorption properties and dynamics of D_2O vapor are still far from being completely understood on a molecular level in the THz region.

In this experiment, the absorption spectra, line-widths, and collision times of D_2O vapor associated with the rotational and vibrational modes in the frequency region 0.4 – 2.0 THz (13.3 to 66.7 cm^{-1}) are measured using the temporal THz-TDS technique and assigned to rotational transitions in ground vibrational state $\nu_0(000)$. To determine the collision-broadened linewidth, the lines were fit numerically to a Lorentzian profile convolved with a sinc function that was determined by the measurement window. The temperature dependence of $\Delta\nu$ at different temperatures was measured and fitted to $\sim T^{-a}$, where $a = 0.75 \pm 0.13$, which gives information on the collisional interaction between D_2O molecules.

Liquid D_2O (99.9% atom % D, Aldrich Chemical Company, Inc., WI) of 10*mg* weight was used without further purification and sealed in a gas cell at one atmosphere. The cell was made with 8-*cm*-diameter and 4-*mm*-thick polyethylene windows mounted at the two sides of a 12*cm* long glass cell. A heat tape was wrapped on the surface of the glass cell to vaporize liquid D_2O. The temperature of the heat tape was controlled by adjusting output voltage of oven. Before the infusing of D_2O vapor in the cell, the humidity of the residual water vapor is 10%. After all D_2O was vaporized, the humidity of D_2O vapor is 53%. The experimental temperatures were set about 296, 325, and 426 *K*. Figure 4.4 shows changes of the profiles of the transmitted pulse in the time-domain upon passing through D_2O vapor as compared with nitrogen (N_2) at room temperature (296*K*). The additional fast oscillations in Fig 4.4(b) for D_2O are caused by the combined action of the dispersion and absorption of the D_2O molecules. The uncertainty of measurement of delay time is ± 0.01*ps*. The power spectrum of the pulses ranging from 0.4 to 2.0*THz* upon transmission through D_2O vapor and the reference gas (N_2 molecules) are shown in Fig. 4.5. The ratio of the power spectral data of D_2O vapor divided by the spectrum of the reference pulse determines the power absorption coefficient $\alpha(\nu)$:

$$\alpha(\nu) = -\ln\left[P_s(\nu) / P_{ref}(\nu) \right] / 2L \qquad (4.2)$$

where L is the path length, $P_s(\nu)$ $(= E_s(\nu)^2)$ is the power spectrum of the THz beam propagated through the D_2O vapor, and $P_{ref}(\nu)$ is the reference power spectrum for N_2.

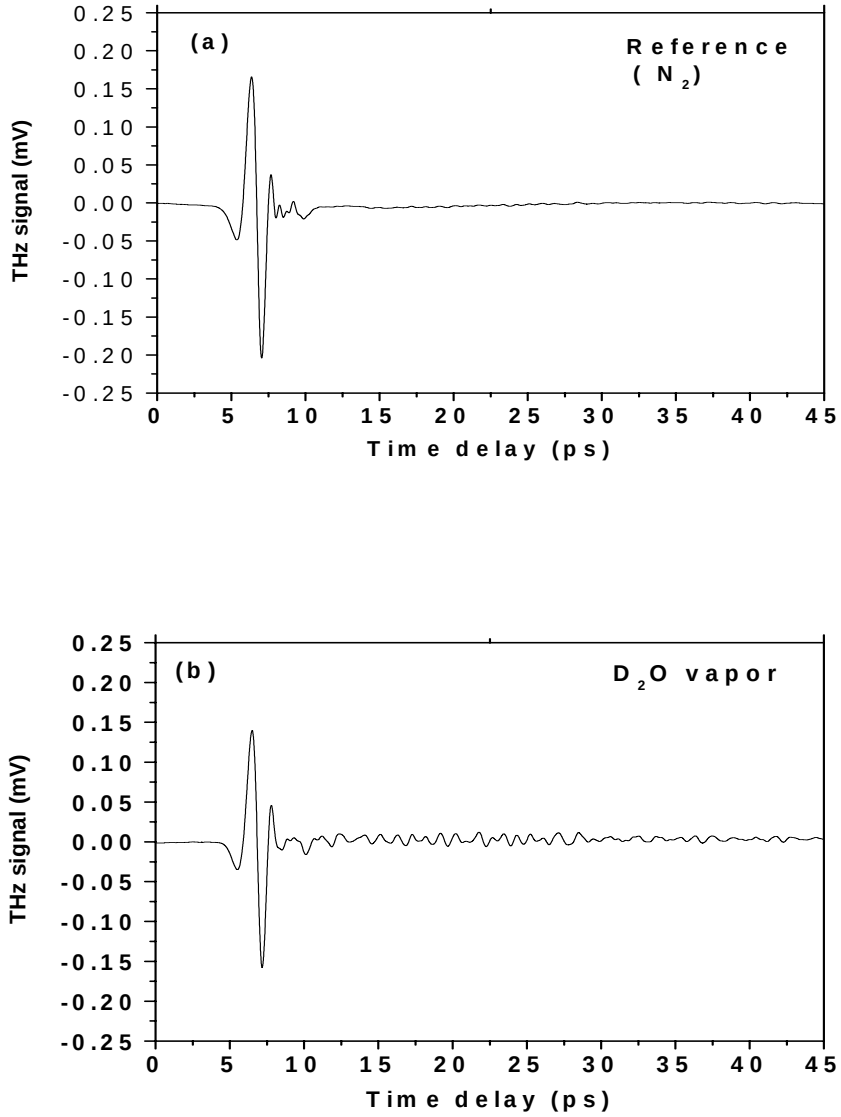

Figure 4.4 Transmission of the THz pulse in the time-domain for N_2 gas (a) and D_2O vapor (b) at room temperature (T=296*K*).

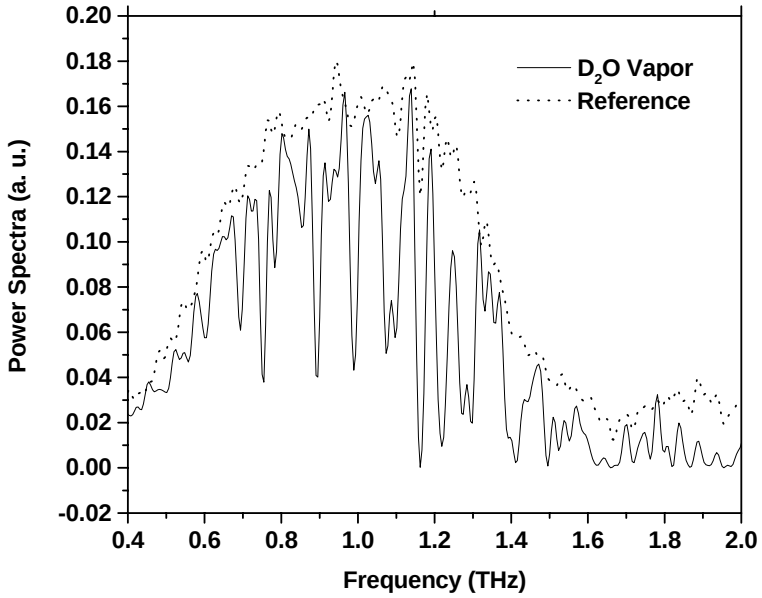

Figure 4.5 Power spectrum vs. frequency (ν) derived from the fast Fourier transform of the temporal data presented in Fig.4.5.

The absorption coefficients for the molecular modes for D_2O are displayed in Fig.4.6 (a). The fit to selected lines on an expanded frequency scale are shown in Fig.4.6 (b) to determine the linewidth $\Delta\nu$. Due to the measurements of transmitted THz field empty cell alone as the reference and the cell filled with D_2O vapor under the same conditions, the effect of residual water vapor on the absorption coefficient $\alpha(\nu)$ is eliminated completely using Eq. (4.2). A summary of the rotational absorption lines and assignments for D_2O vapor is listed in Table 4.2. The frequency values are in agreement with the microwave data from NASA.[97]

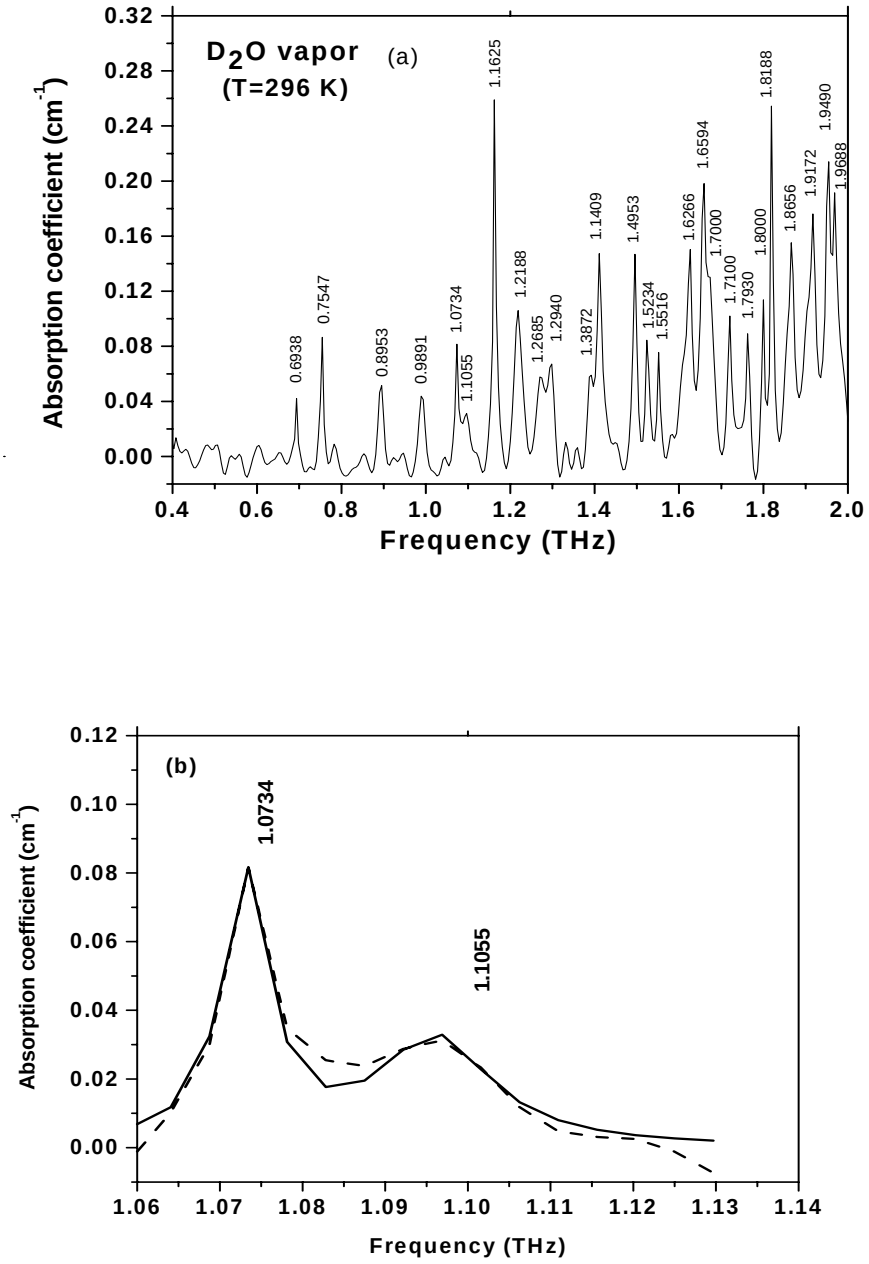

Figure 4.6 Absorption coefficient of D_2O vapor at 296*K* (a) Full spectrum from 0.4 to 2.0*THz*; (b, c, d) Selected lines from 1.0 to 1.6*THz*. Solid line: experimental data; Dashed line: fit from Eq. (4.2).

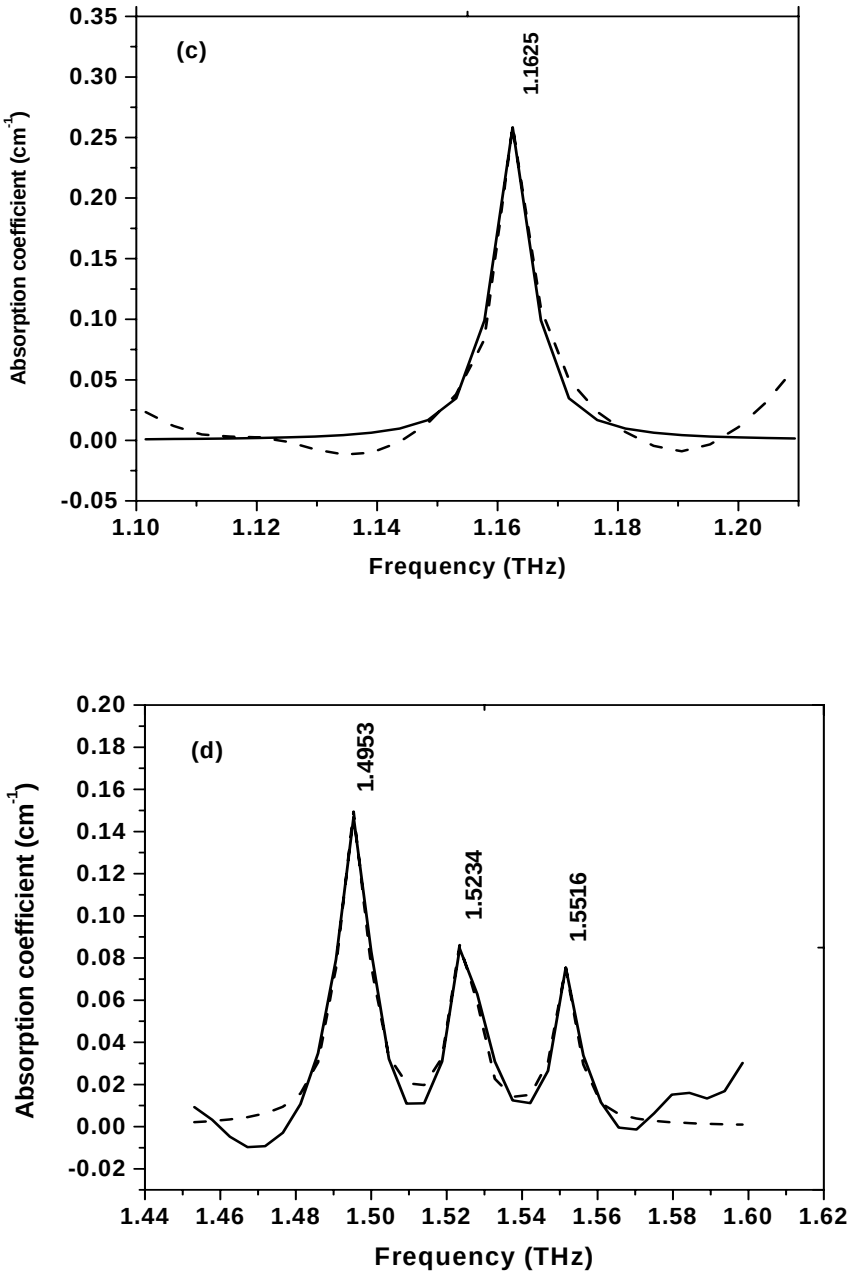

Figure 4.6 –Continued (c, d) Selected lines from 1.0 to 1.6*THz*. Solid line: experimental data; dashed line: fit from Eq. (4.2).

The lines were assigned using that data to transition among rotational quantum numbers, measured level widths and corresponding relaxation times. Twenty-five pure rotational transitions are found from transitions in the ground vibrational state ν_0 *(000)* in the frequency region of 0.4 – 2.0 THz (see Table 4.2). There are no rotational transition lines at room temperature from the ν_2 = (010) vibrational state, which lies above 1178.7cm^{-1}. The same experiment was performed for water (H_2O) vapor at 296*K* (RT) and 21% humidity (see Fig. 4.7), which was used for reference. The frequency numbers in brackets for H_2O vapor are from Grischkowsky and his coworkers. The fifteen absorption lines of H_2O vapor were observed in the frequency

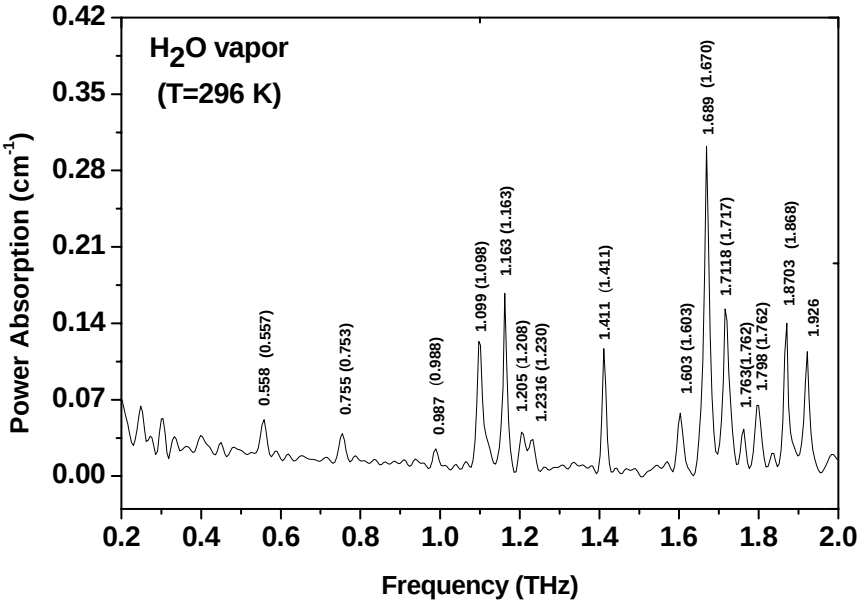

Figure 4.7 Absorption coefficient of H_2O vapor at 296*K* and 21% humidity. The numbers in brackets are from Ref. 75. The results are in good agreement with it

0.2 to 2.0 THz region. Their positions are in good agreement with the previous reports performed at high temperature (1490*K*). Due to the lack of significant population in ν_2 *(010)* vibrational state at room temperature, lines such as at 1.215, 1.592, and 1.644*THz* from this state cannot be detected in our experiment.

Table 4.2[2] Comparison of experimental results with assignments for transitions $\Delta J = 0, 1$ for D_2O vapor at 296K for ground vibrational state manifold.

Freq. (THz) (NASA)	Freq.(THz) (Exp.)	$\Delta\nu_{Exp.}$ (GHz)	$\tau_{Exp.}$ (ps)	Energy (cm^{-1})	Upper J	Upper K_{-1}	Upper K_{+1}	Lower J	Lower K_{-1}	Lower K_{+1}
0.6928	0.6938	12.7	25.1	141.087	4	2	2	4	1	3
0.7831	0.7547	11.3	28.2	114.987	4	1	3	4	0	4
0.8911	0.8953	15	21.2	279.565	6	2	4	6	1	5
1.0659	0.9891	14.9	21.4	74.506	3	2	2	3	1	1
1.0856	1.0734	11.6	27.5	30.265	6	3	3	3	1	3
1.1050	1.1055	13.2	24.1	169.040	4	3	2	5	0	5
1.1590	1.1625	13.8	23.1	35.878	3	1	3	2	0	2
1.2155	1.2188	17.4	18.3	74.506	4	0	4	3	1	3
1.2631	1.2685	13.6	23.4	164.178	4	3	1	4	2	2
1.2880	1.2940	10.0	31.9	783.270	10	4	7	9	5	4
1.3870	1.3872	11.5	27.7	790.821	10	4	6	10	3	7
1.3960	1.4109	9.0	35.0	110.034	3	3	1	3	2	2
1.4985	1.4953	10.1	31.5	217.586	5	3	3	5	2	4
1.5299	1.5234	13.7	23.3	22.684	2	2	1	1	1	0
1.5520	1.5516	9.1	35.0	117.313	5	0	5	4	1	4
1.6167	1.6266	13.1	24.3	20.259	2	2	0	1	1	1
1.6579	1.6594	14.0	22.8	114.987	5	1	5	4	0	4
1.7048	1.7000	12.2	26.1	436.060	7	4	8	7	3	4
1.7083	1.7100	10.4	30.6	877.116	7	2	5	6	3	4
1.7646	1.7930	10.2	31.2	345.447	6	4	2	6	3	3
1.7964	1.8000	11.9	26.8	341.389	7	2	5	6	3	4
1.8210	1.8188	11.5	27.7	49.340	3	2	2	2	1	1
1.8686	1.8656	12.0	26.5	170.243	6	0	6	5	1	5
1.9170	1.9172	10.8	29.5	341.389	6	4	3	6	3	4
1.9449	1.9490	10.9	29.31	427.199	7	4	4	7	3	5
1.9707	1.9688	-	-	-	-	-	-	-	-	-

[2] Http://spec.jpl.nasa.gov. $\tau_{Exp.} = \tau_2 = 1/\pi\Delta\nu$.

In this experiment, as the THz pulse propagates through D_2O and H_2O vapors it excites a coherent ensemble of molecules in the thermally populated rotational and vibrational states. The coherent ensemble has a macroscopic polarization in the direction of the THz electric field, which are time and space coherent. As the coherent ensemble of molecules rotates with rotational frequencies determined by the rotational and torsional vibrational quantum numbers, the ensemble emits THz radiation. This emission of THz radiation at frequencies that correspond to a thermal distribution of rotational transitions are seen as the oscillatory structure that follows the main THz pulse in Fig. 4.4(b) and structures in the spectrum in Fig.4.5. No coherent echoes were observed as the coherent emission observed in methanol gas.[94]

Collisions between the various molecules of the ensemble cause dephasing which is the physical cause of line broadening in the frequency domain and a corresponding complex decay of the emitted THz radiation. Collisional broadening determines the line shape, because Doppler broadening is less than 1% of the collisional linewidth at THz frequencies.[98] The measured profiles are fitted with a numerical convolution of the real part of a Lorentzian line shape with the real part of the window function. A resolution of less ±1.3 GHz was given previously. The complex Lorentzian line shape is given by:

$$\frac{\alpha(\omega)}{2} = A\frac{\Delta\nu}{(\nu-\nu_0)^2+(\Delta\nu/2)^2} * \frac{\sin(\omega T_\omega)}{\omega T_\omega} \qquad \textbf{(4.3)}$$

The asterisk represents the convolution operation and $\alpha(\omega) / 2$ is the field absorption coefficient. The measured complex amplitude spectrum is equal to the convolution of the complex Lorentzian line shape with that of the complex window function. The window $W(\omega)$ is given by:

$$W(\omega) = \frac{\sin(\omega T_w) + i[1 - \cos(\omega T_w)]}{\omega T_w} \qquad \textbf{(4.4)}$$

where ω is the frequency in radians per second. For a given temporal window T_W, the measured time-domain data is the electric field of the THz pulse transmitted through the gas $Es(t)$, multiplied by a square window function: $W(t) = 1$ for $0 < t < T_W$; $W(t) = 0$ for $t > T_W$. The measured signal in the frequency- domain is the convolution of the Fourier-transformed window function $W(\omega)$ and the complex amplitude spectrum of the THz pulse, $E_S(t)$. For narrow absorption features and a small absorption coefficient ($\alpha L < 4$), the measured absorption can be fitted well by a convolution of only the real parts of the line-shape and window function. This approximation is obviously valid for our experiments. The variable A, ν_0, and $\Delta\nu$ *(FWHM)* were allowed to float to obtain the best possible fit. Examples of fitting to various lines are shown in Fig.4.6 (b). The accuracy for the linewidth is ± 0.2 *GHz*. The linewidth of rotational absorption lines of D_2O molecules is attributed to two dominant collision-broadening mechanisms. These are collisions with other D_2O molecules and collisions with nitrogen. The total FWHM

linewidth is inversely related to the collisional dephasing time τ_2 by $\Delta\nu = 1/\pi\tau_2$ (see Table 4.2).

The line widths for rotational levels ($\Delta\nu$) depends on temperature through collision (or pressure) broadening which is given by a product of density, thermal velocity, and the collision interaction given by the optical cross section. The linewidth becomes:

$$\Delta\nu(\mathrm{T}) = \rho(\mathrm{T})\mathrm{v}\,(\mathrm{T})\;\sigma(\mathrm{T}) \sim \mathrm{T}^{-(n+1)\,/\,2\,(n-1)} \qquad \textbf{(4.5)}$$

The temperature dependence comes from thermal velocity ($v\,(T) \sim T^{1/2}$), gas density ($\rho\,(T) \sim T^{1}$), and the optical cross section ($\sigma\,(T) \sim T^{m}$), which depends on the force of interaction in a collision ($m = -\frac{1}{1-n}$). The dependence of the collision cross section on velocity for an intermolecular potential proportional to $1 / r^n$ can be obtained. The temperature dependence of the *FWHM* is contained in the value of the exponent n, which depends on the *J* and *K* values for the rotational states of the interacting molecules. For N_2-broadened low-J state in H_2O vapor, $n = 6$, for pure rotational bands. The temperature dependence of the linewidth gives information about the force law between colliding molecules with a $1 / r^6$ force. To gain additional information on characteristics of rotational absorption of D_2O molecules on temperature, the temporal profiles for D_2O at different temperatures were measured. This dependence leads to the observed absorption line decreases as the temperature increases. Fig.4.8 gives the

relationship of $\Delta\nu\,(T)$ versus T for 0.6938 THz at 296, 325, and 426 K. The higher the temperature, the smaller the linewidth becomes. The relaxation times τ_2 for these temperatures are 25.1, 26.3, and 29ps, respectively. In order to determine the temperature dependence exponent of linewidths for D_2O vapor, a plot of the set of points $ln(T_0 / T)$ vs. $ln[(\Delta\nu(T) / \Delta\nu(T_0)]$ for the line at 0.6938 THz at different temperatures is shown in Fig.4.4. The best fit to Eq. (4.4) yields $\Delta\nu\,(T) \sim T^{-0.75\pm0.13}$. The exponent 0.75±0.13 is comparable to the value for N_2-broadened low-J H_2O. This result of 0.75±0.13 shows the linewidth reduces with increasing temperatures arises from $1 / r^6$ intermolecular interactions.

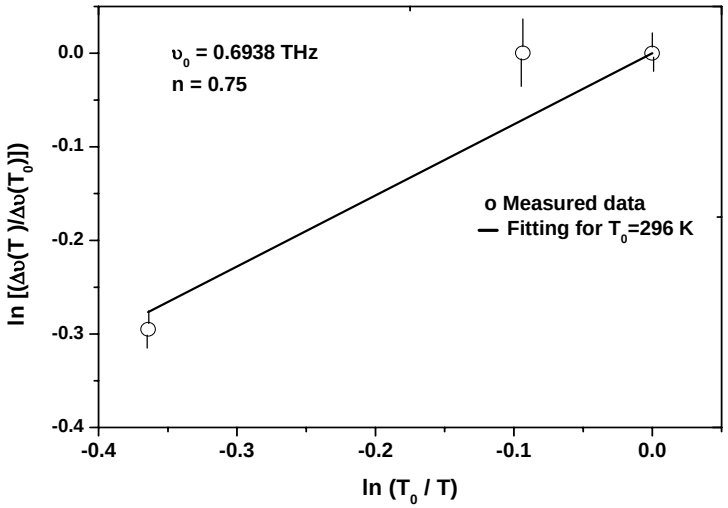

Figure 4.8 Ratio of absorption linewidths measured in D_2O vapor vs. temperature. Each error bar corresponds to the average of three points.

Chapter 5- Methanol Gases

5.1 Coherent Rotational Transients after the Passage of THz Beam in Methanol Gases - Periodic Rephasing and Dephasing

Pulse propagation in resonant media can create interesting optical and physical phenomena. Most of them originate from the transient response of a medium to coherent radiation. Coherent transients resulting from the interaction of electromagnetic radiation with resonant systems were first studied for nuclear and paramagnetic spin systems at radio and microwave frequencies. Analogous studies in the optical regime were initiated by the pioneering work of Hartman and coworkers using the photon-echo experiments[99]. Since that time there have been extensive studies of coherent effects in both the optical and infrared regimes using nonlinear optical effects.[40,100] while many of these phenomena are analogs of effects first observed in spin resonance, some of them do not have a spin-resonance counterpart because of electromagnetic propagation effects. In fact, there are still many interesting and intriguing effects in a multilevel system with multiple pulse excitations using femtosecond laser pulses and THz radiation in biology, chemistry and physics. Recently, there is an interested in torsional motions in complex biological molecules such as tryptophan and proteins. Recently, coherent transients for only simple "symmetric molecules" such as N_2O, CH_3Cl, CH_3Br, and CH_3F have been studied and pioneered by Grischkowsky and his co-workers using terahertz time-domain spectroscopy (THz-TDS).[101] An emission was observed in the form of a coherent THz transient pulses occurring from periodic rephrasing of ensemble of coherent excited

rotational levels with commensurate transition frequencies. A sequence of pulses was observed after a single pulse excitation and described in terms of commensurate radiations. An alternative explanation for the generation of a sequence of pulses is proposed in the present work arising from locking process the frequencies of the large number of rotational levels in methanol and its isotopes arising from the absorption of a broad band ultra fast THz pulse of a number of correlated rotational levels, analogous to mode – locking. So far, no coherent transients have been observed in THz region for large molecules.

In this experiment, we have direct observation of coherent transients excited by a broadband THz pulse from large complex "asymmetric molecules" of methanol (CH_3OH) and its isotopes (CH_3OD, and CD_3OD) giving fundamental information on the dephasing and decoupling of an ensemble of coupled rotational levels. A series of strong coherent commensurate pulses attributed to the initial excitation of ensembles of well-spaced rotational levels for these complex molecules are observed and attributed to periodic dephasing and rephasing of an initial excited ensemble of commensurate rotational levels. The frequency-dependent absorption and dispersion of the sample were obtained from commensurate pulses in the 0.2 – 2.0THz range. Up to this time, no study on the coherent transients for complex asymmetric large molecules such as methanol and its isotopes have been reported or even expected. The THz-TDS setup used for this experiment is shown in Fig. 2.7b.

The accuracy of the measurements depends upon the relatively long-term changes in the laser pulses and the consequent changes in the input terahertz pulses. In order to estimate uncertainties of the measurements, the following sequence of the measurements was performed: first the reference terahertz pulse (empty cell without sample) was measured, and then measured the terahertz pulse transmitted through the sample, and finally the reference pulse with the sample removed was measured. This sequence was repeated several times to obtain good statistics. Typically, the amplitude ratio of subsequent THz pulses transmitted is ± 2%. In the same manner, the delay time of subsequent reference pulses varies by ± 0.05*ps*. The liquid methyl alcohol (methanol) and its isotopes (Merck, Spectroscopic grade) samples were used without further purification. The measurements were performed mostly at room temperature

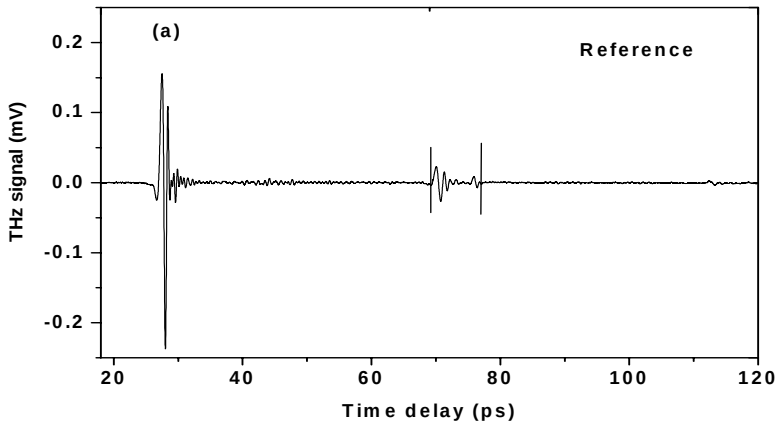

Figure 5.1 (a) Transmitted THz pulse profile without CH_3OH in the cell and with N_2 purged

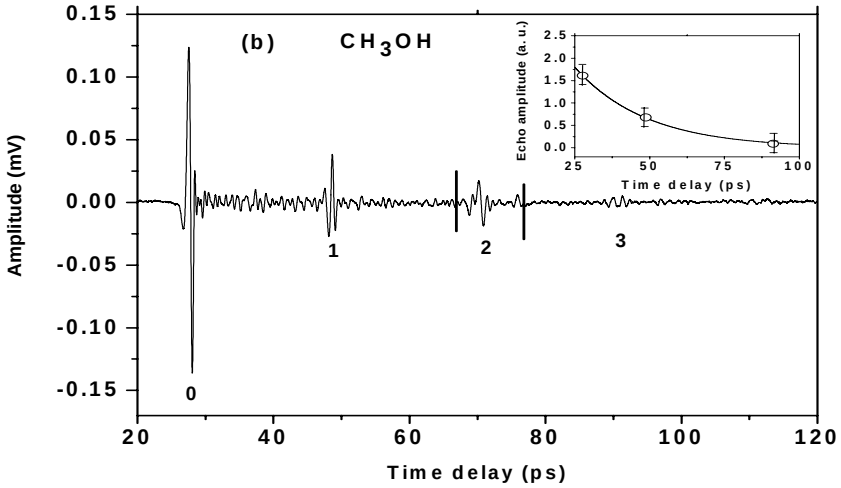

Figure 5.1 (b) Measured THz pulse profile with one atmosphere CH_3OH. The decay of the commensurate pulse amplitude is shown in the insert of (b), fit to ~ e^{-t/T_2} (T_2 = 23*ps*) (fitting, o experimental data). Each error bar corresponds to the average of three points.

on methanol vapor within a temperature controlled 9.5-*cm*-long cell having 2-*cm*-thick, 6.5-*cm*-diam windows of polyethylene windows.

The profile of the output amplitude of terahertz pulse from an empty cell as function of relative delay time shown in Fig. 5.1a is used for reference. In addition to the main pulse at ~ 28*ps*, a reflected pulse from the ZnTe crystal is observed at ~ 68*ps*. When the cell is filled with vapor, the output profile of pulse changes and is shown in Fig. 5.1b. The output pulse is followed by a series of commensurate coherent transients appearing every ~ 21*ps*, which rapidly decay in intensity because of the strong collisional broadening. In Fig.5.1 (b) one can see the transmitted excitation

pulse followed by several commensurate coherent transients (labeled as 0 to 3) emitted from a multilevel system due to multi-photon excitations by THz pulses.

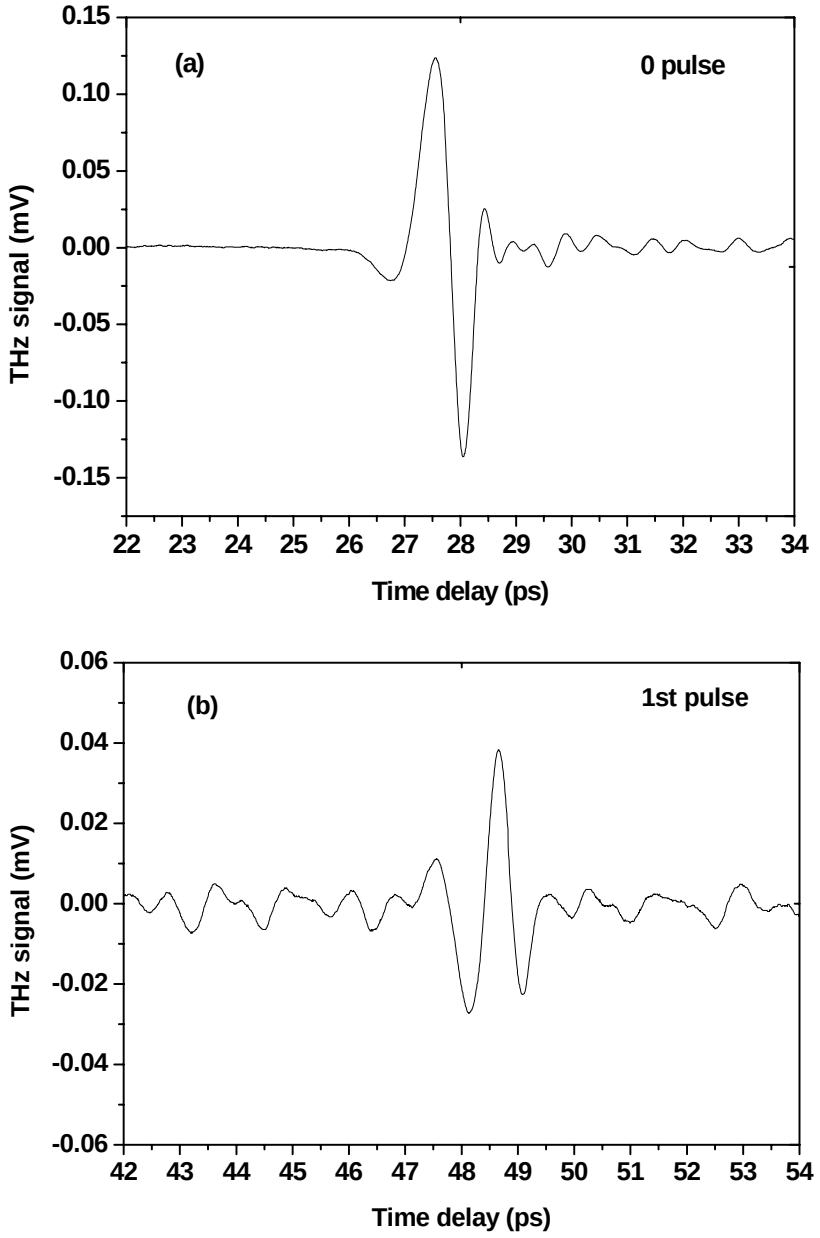

Figure 5.2 Transmitted THz pulse profile of signal of (a, b, c) 0, 1st , 3rd pulses on magnified time scale for one atm methanol vapor data presented in Fig.5.1 (b).

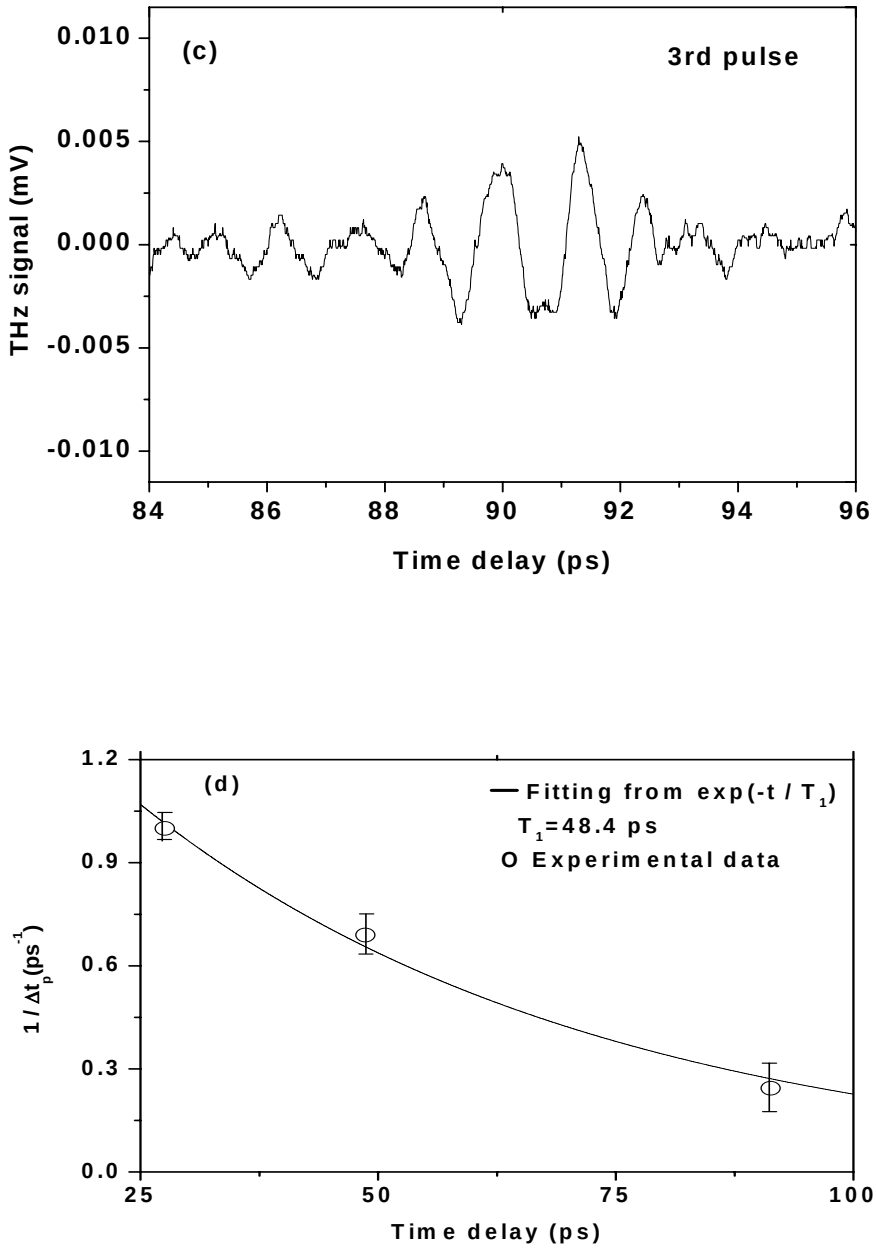

Figure 5.2-Continued (d) the duration of the sequence pulses versus delay time. Δt_p is the duration of the sequence pulses, fit to $\sim e^{-t/T_1}$ ($T_1 = 48.4ps$) (fitting, o, experimental data). Each error bar corresponds to the average of three points.

Fig.5.2 displays the pulse shape of free decay of original pulse, the first, and third pulses on a magnified time scale for one *atm* methanol vapor for data presented in Fig. 5.1(b). The relative amplitude of the first transient is 1/2.5 that of the excitation pulse of 2ps duration. The decay of the sequent pulse amplitudes provides information on the average collisional dephasing time T_2 associated with the linewidth of rotational levels, $\Delta\nu^{-1}$ (discussed later). From above observations, $T_2 = 23 \pm 0.5ps$ was directly determined from the amplitude of the sequence pulses for CH_3OH gas at $296K$ (see insert Fig. 5.1 (b)). An exponential decay ($\sim e^{-t/T_2}$) was used to fit the experimental data of the amplitude of the sequence pulses as shown in the insert Fig.5.1 (b). Under the same experimental condition, we measured the coherent transients for CH_3OD and CD_3OD gases. The temporal spacing of coherent transient occurs at ~21, ~22 and ~26ps (corresponding to the inverse frequency spacing of rotational level for transition $\Delta J = \pm 1$ of approximately $\Delta\nu_R$ ~48, 45 and 38 *GHz*, respectively)[102,103,104] between the first coherent transient and excitation pulse for CH_3OH, CH_3OD and CD_3OD were observed, respectively. The measurement shows the spacing between the free induction decay pulses increases with increasing mass of the molecule, corresponding to the closer rotational line spacing in the frequency domain. These results agree with rotational energies and transitions from on microwave measurements. This observation indicates that within the broad spectral range covered by the THz pulses the methanol molecules have a manifold of modes of pure rotational absorption lines, which are simultaneously excited by the THz pulse. These rotational levels are populated at $t = 0$. The molecules respond to this excitation

by radiating a free decay signal, which decays because of relaxation, reemission, interference and propagation effects. The pulses arise from emission from the excited rotational ensemble at $t = 0$. Because the methanol molecules and its isotopes possess an almost constant frequency spacing between the rotational levels, a periodic dephasing and rephasing of the entire ensembles of the more than thirty excited transitions ($N \geq 30$) is observed in the 0.2 to 2.0 THz frequency range. This observation is in contrast to that of ethanol (C_2H_5OH), water vapor (H_2O), deuterate water vapor (D_2O), CS_2 and other complex molecules studied earlier by THz time-domain spectroscopy where no periodic pulses or coherent effects were observed.[31] These molecules do not possess commensurate well-spaced rotational resonance levels to produce coherent response. CH_3OH and its isotopes possess a set of levels at constant frequency spacing between rotational levels in the maze of levels. The dephasing and rephasing of excited ensembles can occur resulting in a periodic pulse trains separated by the inverse of frequency separation between adjacent rotational levels ($\Delta\nu_R$). This ensemble of rotational levels are excited at $t = 0$. The ensemble dephases as time process ($\phi_m = \omega_m t$) and after time of ~1 / $\Delta\nu_R$ rephrases to emit another pulse like in mode locking, which produces a pulse train. The time duration (Δt_p) of the sequence pulses (0, 1, 3) increases due to the decoupling among the rotational levels at time T_1, and the centrifugal dephasing towards equilibrium (see Fig. 5.2 (a), (b) and (c)). Fig.5.2 (d) shows the change of the pulse duration of sequence pulses versus the delay time. From the increase in duration of these pulses, a value of depopulation time T_1 for N levels is estimated to be $T_1 = 48 \pm 0.5$ps using the

relationship of $\Delta t_p^{-1} \sim N$, where N is number of coupled rotational levels after a time t. The origin of repetition pulses is a periodic rephasing of a coherent ensemble of N excited rotational levels from a 200fs pulse with commensurate transition frequencies between the rotational level $\Delta J = \pm 1$, which becomes less at time increases. Because of the repetition of the free induction decay pulses and because the frequencies are numerical multiple of the fundamental frequency, equal to the spacing between adjacent rotational lines, the periodic pulses have been called "THz commensurate echoes".

The sequence of signals show significant reshaping and pulse broadening with increasing pulse number (0, 1, 3) which is caused by small derivations from the rigid-rotator model of the CH_3OH molecules (see Figs. 5.2 (a), (b) and (c)); and as mentioned, the broadening of the pulse duration is mostly caused by decoupling of N rotational levels with time. The centrifugal forces can lead dephasing for symmetric molecules. The centrifugal distortion is more important in the microwave spectral region for asymmetric rotators than in the spectrum of symmetric tops. Microwave transitions occur in asymmetric rotors between states of large angular momentum and of very large rotational energies. As for "asymmetric" molecules of CH_3OH, the centrifugal can increase the moment of inertia of a rotating molecule which leads the frequency spacing between adjacent rotational lines is not constant but decreases slightly with increasing rotational quantum number J. Each rotational line further consists of a series of transitions associated with the quantum number K, representing the projection of the angular momentum on the molecular symmetry axis. Due to the

centrifugal stretching perpendicular to this axis, the degeneracy of the K transitions is relaxed, and an additional small line shift with increasing K is observed. This anharmonicity causes a gradual dephasing of the individual transitions and manifests itself as a change in the pulse shape with time. Analogous to Doppler dephasing, where there is an induced polarization in the gas and the commensurate signal is washed out due to frequency shifts resulting from the motion of the molecules, we assign this broadening phenomenon to centrifugal dephasing and depopulation of N rotational levels. This is first time that this type of dephasing has been observed directly for asymmetric complex large molecules like methanol and its isotopes in the In conclusion, coherent transients for the methanol and its isotopes are directly observed in the time domain. These coherent transients arise from the excitation of an ensemble of coherent rotational levels via resonant absorption by a ~ 200fs THz pulse. These THz pulse spans the rotational levels for the asymmetric molecules. The emission from these excited rotational states form a sequence of pulses separated by inverse of rotational level, $\Delta\nu_R^{-1}$, from dephasing and rephasing of the ensemble of the excited rotational molecules in time. The signal amplitude of pulses decreases with relaxation time $T_2 = 23 \pm 0.5ps$ associated with dephasing of the ensemble of rotational levels. The decay of the pulse amplitude agrees well with T_2 inferred from the linewidth of the rotational transition $\Delta\nu$. This agreement is explained by large numbers of rotational transitions that are coupled and almost exactly equidistant at $\Delta\nu_R$. These large numbers of coupled rotational levels, N, resulted in completed superposition of the emitted electric fields at the second and subsequent pulses. This

effect is unusual for a large molecule like methanol and its isotopes. The duration of sequence pulses increases due to decoupling of rotational levels at time $T_1 = 48 \pm 0.5ps$ and centrifugal dephasing effects.

Chapter-6 Tryptophan

6.1 Torsional Vibrational Modes of Tryptophan Studied by Terahertz Time-Domain Spectroscopy

There is an increasing interest in understanding the molecular dynamics associated with the vibrational, rotational, and torsional modes of biomolecules during photodynamical and structural changes. The dynamics of molecular components of proteins involves low-frequency collective modes of particular subunits. Molecules excited up to the vibrational ladder can cross the transitional energy barriers[105] The dynamics of the collective modes generally occur via anharmonic interactions with other normal molecular modes, leading to energy exchange. It is believed that the lowfrequency collective modes are responsible for the directed flow of conformational energy for a variety of biological processes, ranging from primary photoisomerization events of vision to enzyme action. [106,107] The motions of molecular subunits within proteins are associated with different functions. Photo-induced isomerization in the primary stages and absorption changes during structural changes in different stages of the photo-cycles of some proteins are associated with collective motions. These processes involve well-defined torsional modes along one of the C=C bonds of the polythene chain. Knowledge of the relaxation lifetimes of these modes is important to improve these processes as well as to obtain a better understanding of the theory. Tryptophan, an essential amino acid found in proteins and present in foods, affects our daily life. Tryptophan is one of the key biological photoactive fingerprint molecules

used in cancer and bacteria detection using fluorescence spectroscopy. Far-infrared (FIR) studies of materials have been limited due to the weak sources and low signal/noise ratios, especially below $100cm^{-1}$. Recently, pulsed terahertz time-domain spectroscopy (THz-TDS) has been used to overcome these difficulties and have become a versatile tool for spectroscopy on a wide variety of samples in the FIR. Most recently, the THz technique has been applied to examine DNA and some other bio-molecules. [108,109,110] THz-TDS relies on coherent generation and detection of an ultra short pulse with a large signal/noise ratio of 8000–10,000 over a large bandwidth.

In this study, the THz absorption, index of refraction, and dispersion of a tryptophan film and pressed powders were measured and analyzed to determine the main torsional modes and representations of the subunits in the frequency range 0.2–2.0 *THz* (6.6–66 cm^{-1}).

Tryptophan films were prepared by mixing tryptophan powders with methyl alcohol. Tryptophan powders were purchased from Sigma-Aldrich (St.Louis, MO; No. T-941) and were used without further purification and stored in the dark below 58°C. The molecular structure, subunits, and the diagram of a tryptophan sample are shown in Fig.6.1. Films from 0.2 to 1.2*mm* thickness were prepared by applying an approximate pressure of 100 $kg\ cm^{-1}$ to the mixture on a polyethylene substrate with thicknesses of 2.0 and 4.0*mm*. The thicknesses of 2.0 and 4.0*mm* for polyethylene windows were chosen to eliminate etalon spectral oscillations from the substrate. The thickness of the film was measured using a micrometer (Accuaro Gold, Phillipsburg,

NJ) with an accuracy of 60.01 *mm*. Pressed powders were also used as samples with different window thicknesses.

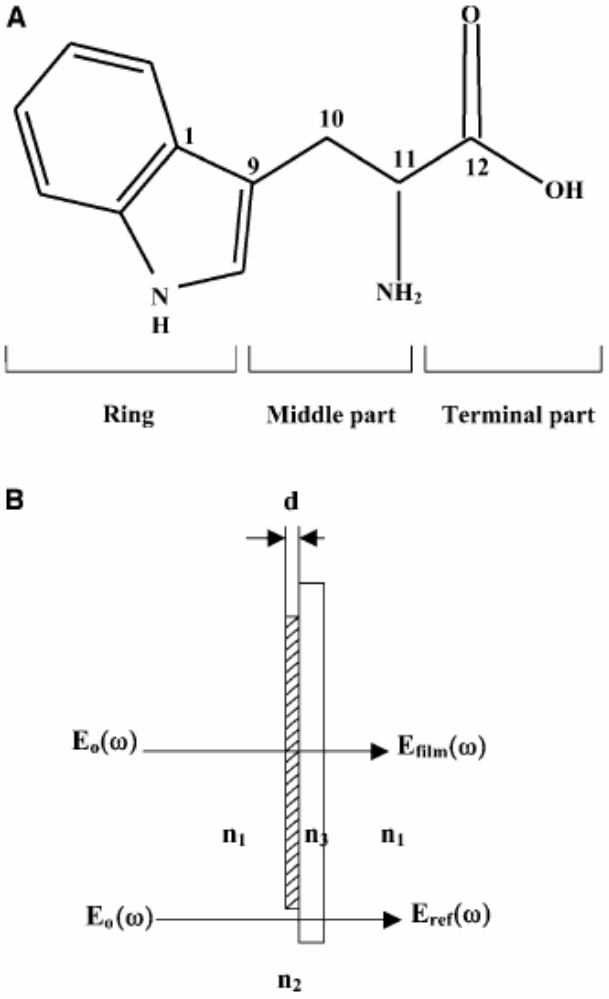

Figure 6.1 (a) Structure and subunits of the tryptophan molecule and (b) diagram of the tryptophan sample. n_1, n_2, and n_3 are the refractive indices of air, the tryptophan film, and the polyethylene substrate, respectively.

The THz-TDS system used for the measurement was shown in Fig.2.7b.

The THz temporal profiles after transmission through a pure polyethylene substrate alone (reference) and a tryptophan film (thickness 0.82 *mm*) with substrate are shown in Fig.6.2. The analysis of the absorption and index of refraction of the tryptophan film are performed by alternating measurements of the transmission three times at normal incidence through the tryptophan film with substrate, and through only the pure polyethylene substrate as a reference. To avoid complications from multiple reflections from the substrate, the maximal recorded delay was limited to 12 *ps* by the translation stage. A distinct temporal shift of about Δt = 492 *fs* can be seen between the peaks of Fig.6.2 *a* and *b*, which is related to the thickness of the sample d and its group index n_g. Using the relationship of group delay $\Delta t = (n_g - 1)\, d/c$, where *c* is the velocity of light in free space, n_g = 1.18 is obtained (d =0.82*mm*). A fast Fourier transform of the temporal profiles (Fig.6.2) was performed, and the resultant power is shown in Fig.6.3 for both the substrate and the film on the substrate. The power spectrum signal-to-noise ratio was better than 104:1 on semilog *P(n)* plots (inset of Fig.6.3). The absolute frequency scale is calibrated using the known positions of water vapor absorption lines. Weak, discrete absorption lines due to water vapor are visible as dips in the frequency spectrum and small oscillations after the main pulse in the time-domain signal. Different THz waveforms in shape and magnitude shown in Fig.6.3 indicate some absorption in the tryptophan film. From the Fourier transforms (power spectra and phase shifts), we can determine the frequency-dependent absorption and index of refraction for the film.

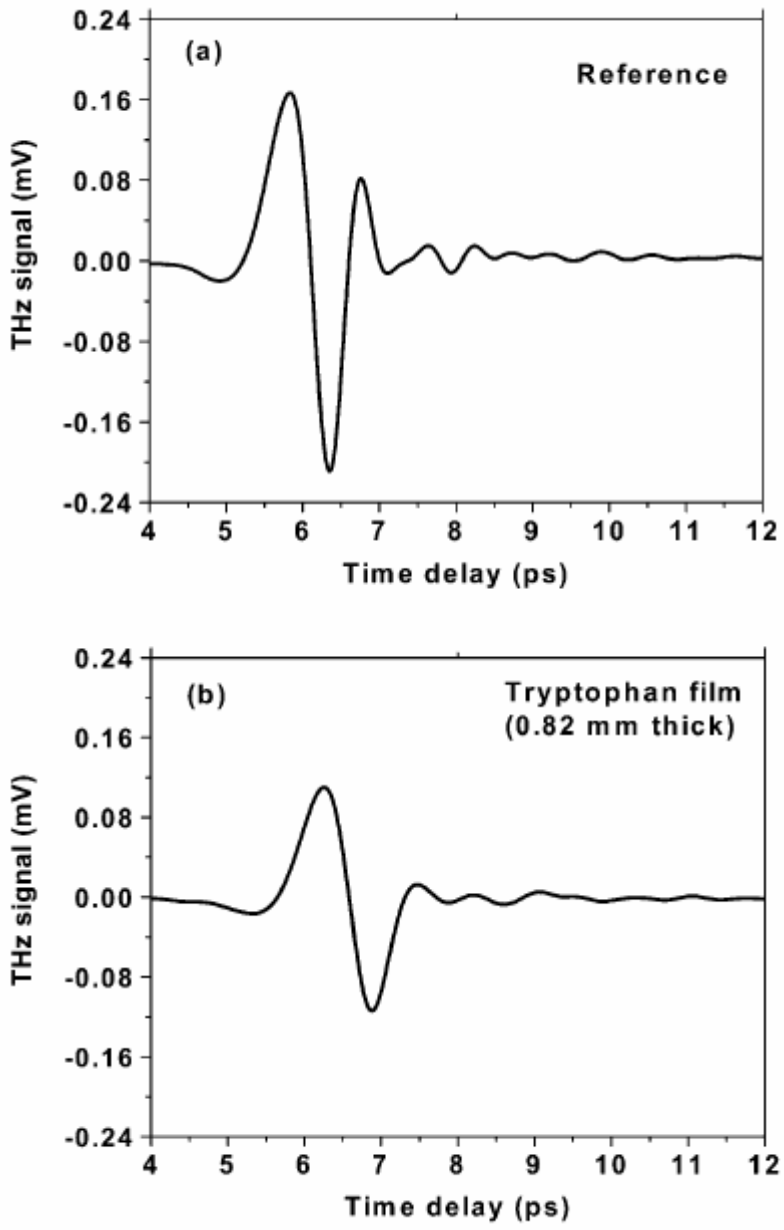

Figure 6.2 Measured THz temporal profiles for (a) the polyethylene substrate alone and (b) the tryptophan film with a thickness of 0.82 *mm* on a 4-*mm*-thick polyethylene substrate.

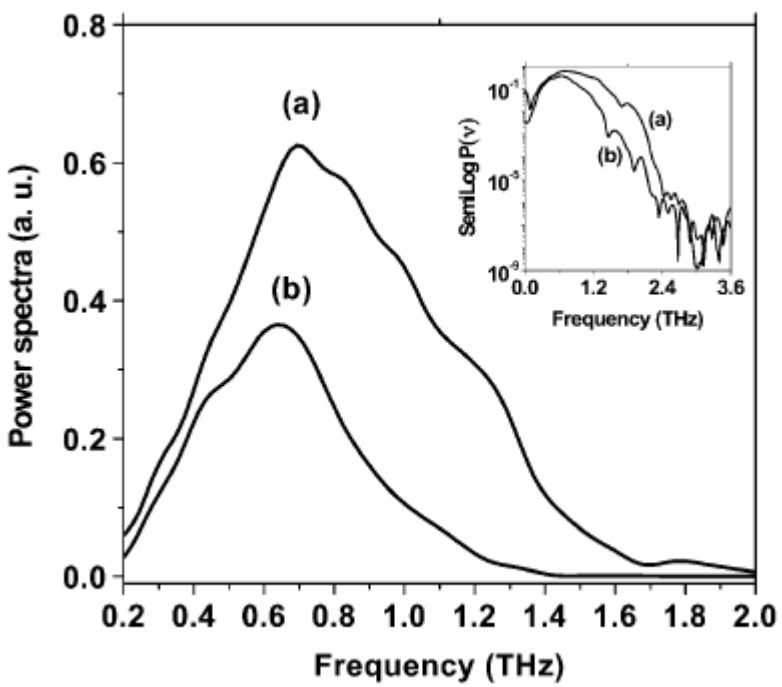

Figure 6.3 Power spectra of (a) the polyethylene substrate alone and (b) the tryptophan film covered on the polyethylene substrate. The logarithm dependence of the power spectra on frequency (n) is shown in the inset.

For our experimental situation with a relatively small total absorption and a thin sample, multiple reflections of the THz pulse occur between the two surfaces of the sample (tryptophan film). When we consider the effects of the multiple reflections (Fabry-Perot effect) and the reflection losses from the interfaces of air/film and film/substrate (Fig.6.1b), the field $E_{film}(\omega)$ after the film has the form[111] :

$$E_{Film}(\omega) = \frac{\eta(\omega) t_{12} t_{23} \exp\left[-i \frac{\hat{n}_2 \omega d}{c}\right]}{1 + r_{12} r_{23} \exp\left[-2i \frac{\hat{n}_2 \omega d}{c}\right]} E_0(\omega) \qquad \textbf{(6.1)}$$

The reference field $E_{ref}(\omega)$ without the sample is given by:

$$E_{ref}(\omega) = \eta(\omega) t_{13} \exp\left[-i \frac{\hat{n}_2 \omega d}{c}\right] E_0(\omega) \qquad \textbf{(6.2)}$$

where $E_0(\omega)$ is the incident field, and $E_{ref}(\omega)$ and $E_{film}(\omega)$ are the reference (without the film) and signals (with the film) respectively. All the reflection, transmission, and propagation coefficients in media 1 and 3 are included in term $\eta(\omega)$ where the echoes of the terahertz wave created in media 1 and 3 are negligible or occur in a timescale different from that corresponding to the signal of interest.

The t_{12} and r_{12} are the complex Fresnel transmission and reflection coefficients from air into the sample of thickness d; t_{23} and r_{23} are the transmission and reflection coefficients from the sample into the substrate; and t_{13} is the transmission coefficient from the air into the substrate. The complex refractive index is $\hat{n} = n - i\kappa$, where $\kappa = c\alpha / 2\omega$. With THz-TDS we can measure the magnitude and phase difference of the complex transmission amplitude. The complex spectrum $E_{ref}(\omega)$ of the reference THz pulse is related to the complex spectrum $E_{film}(\omega)$ of the output THz pulse by the equation:

$$E_{Film}(\omega)/E_{ref}(\omega) = |t(\omega)|\exp[-i\Delta\phi(\omega)] \quad \textbf{(6.3)}$$

where the term $\Delta\phi(\omega)$ is the phase shift between $E_{film}(\omega)$ and $Eref(\omega)$. Using the Fabry-Perot analysis[112] of Eq. 6.1 and the measured ratio of $E_{film}(\omega)/Eref(\omega)$, we numerically remove the multiple reflection effects from our measured data and determine the power ($P(\nu) = E^2(\nu)$) absorption coefficient $\alpha(\nu)$ and the refractive index $n(\nu)$ as shown in Fig. 6.4 a and b, respectively. Two dominated modes occur at 1.435 THz and 1.842 THz. Under the same measurement conditions, we measured the absorption and refractive index for two additional samples with the thicknesses of 0.4 and 1.2*mm*. The similar absorption coefficient peaks were obtained. The results indicate the origin of the absorption peaks that we observed comes from the tryptophan molecules.

To clarify and support the above results on the films, pure powders of tryptophan were pressed between two polyethylene windows instead of onto just one window. Two dominated absorption peaks at around 1.481 and 1.819 THz were still observed. The peak delay of 0.63ps for the powder sample with a thickness of 0.705*mm* was obtained which leads a group refractive index of 1.27 (see Fig.6.4). The refractive index of pressed powders is larger than that of the tryptophan film (~1.18). Liquid CS2 sealed in a 2-*mm*-thick quartz cell was used as reference sample. A 4.1*ps* shift in the time domain was obtained, leading to the group index of refraction of n_g = 1.62, which agrees well with the previous report (see Fig. 5.8)**Error! Bookmark not defined.**.

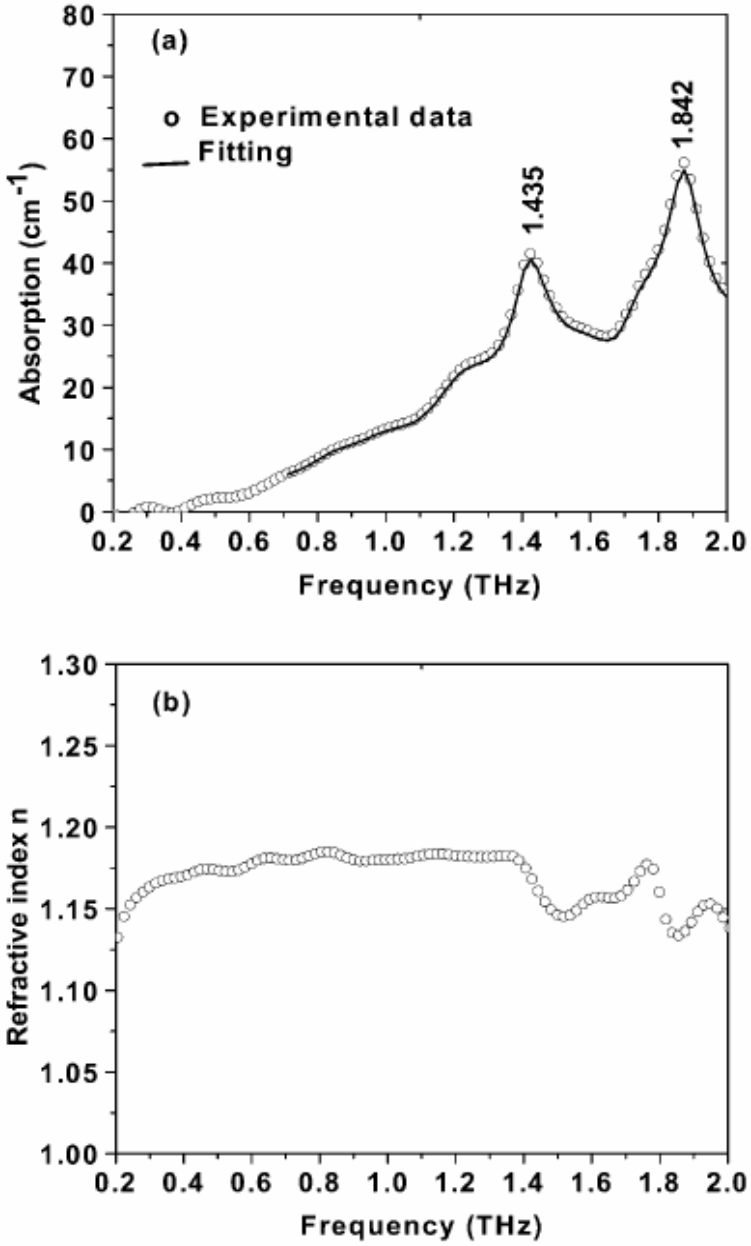

Figure 6.4 (a) Absorbance of the tryptophan film versus frequency (ν). A good fit between 0.7 and 2.0THz (solid line) was achieved using the parameters given in Table 6.1. (b) Refractive index of the tryptophan film versus frequency (ν).

Using the standard expression for Lorentzian oscillators, it is possible to extract the center frequencies ν_j, the linewidths Γ_j and the oscillator strengths S_j of the several different modes for film samples which have small inhomogeneous broadening. For the sample of pressed powder, the inhomogeneous broadening cannot be ruled out, and therefore Lorentzian oscillators cannot be used to describe the mode profiles directly. The relaxation lifetime (τ) of the mode can also be extracted for Lorentzian using the relationship of $\tau\Gamma = 0.2$.[113] The Lorentzian oscillator model offers a simple description of the complex refractive index across the band profile. It is of crucial importance for the accuracy of the fitting procedure that our method permits simultaneous determination of both absorption and refractive index data. The frequency-dependent complex dielectric function used is:[110,114]

$$\hat{\varepsilon}(\nu) = \varepsilon_\infty + \sum_{j=1}^{\infty} \frac{S_j \nu_j}{\nu_j^2 - \nu^2 - i\nu\Gamma_j} = (n - i\kappa)^2 \qquad \textbf{(6.4)}$$

where the sum is taken over the different oscillators. The high-frequency contribution to the dielectric function is denoted by ε_∞. The absorption coefficient and refractive index from 0.2 to 2.0*THz* were fitted to two oscillators. The center frequency, line width, oscillator strength, and mode lifetimes were extracted from the fits. The results are listed in Table6.1.

The vibrational frequencies of the tryptophan modes are distributed from 3700 *cm⁻1* (O-H stretching) to a few *cm ⁻1* (collective modes of the entire protein) in the

mid- to FIR regions. Strong force constants and small masses result in high vibrational frequencies, such as for O-H, N-H, and C-H stretching. The concerted motions of a large number of atoms in these low frequencies appear to be mainly from bending, deformation, and torsional motions involving changes in bond angles. To back up the conclusions above, the low-frequency motions of the modes were calculated using density functional theory (DFT) with software package Gaussian 98 using B3LYP theory and the 6–13G basis set[115]. The absorption spectrum and refractive index were calculated by assuming that each resonance mode can be described as a damped oscillator, resulting in a characteristic absorption and refractive index profile described by Eq. 6.1.The results are shown in Table6.1. The major observed modes for the film sample agree fairly well with the calculated results. In addition, in accordance with the analysis for the low-frequency torsional modes for all-trans-retinal reported by Walther et al. (2000) and Gervasio et al. (1998), the modes at 1.435 *THz* are assigned to C11-C12 torsional motions and the mode at 1.842 *THz* is localized at the ring C1-C9 (Fig.6.1).

Table 6.1 Molecular parameters extracted from the fit of the absorption data based on Eq.6.1 and mode assignments in the frequency range of 0.2–2.0 THz

	Tryptophan	Calculated by DFT	Mode assignment
ν_1	1.435 THz (47.4 cm^{-1})	1.492 THz	C11-C12
Γ_1	0.2060		Chain, terminal part
S_1	0.0170		
τ_1	0.9709 ps		
ν_2	1.842 THz (60.8 cm^{-1})	1.80 THz	C1-C9
Γ_2	0.1820 THz		Ring
S_2	0.0123		
τ_2	1.0989 ps		

The curve in Fig. 6.4a shows two broad bands of THz absorbance for the film sample centered at 1.435 *THz* (47.4$cm^{-}1$) and 1.842 *THz* (60.8 $cm^{-}1$). The full-width half maximums (FWHM) of these bands are 0.2060 and 0.1820, respectively. The refractive index as a function of frequency is shown in Fig. 6.4 b, where $n(\nu)$ =1.14 to 1.2 is obtained over the 0.2–2.0 *THz* (6.6–66 $cm^{-}1$) region and is consistent with the calculated value of n_g. The oscillation $n(\nu)$ is consistent with absorption results.

Since localized twisting motions of nonpolar groups show a weak THz absorption, we estimate that the THz absorbance band in tryptophan is mainly due to many low frequency modes, which are collective modes. Because of the dense manifold of torsional states in tryptophan in the THz region and the short relaxation lifetime of these modes, the spectrum appears as a broad continuum of states. The fits to bands are Lorentzian and satisfy the fundamental relationship $\tau\Gamma = 0.2$, which connects the linewidth Γ and the relaxation lifetime τ. The relaxation lifetimes of torsional modes are on the order of picoseconds to subpicoseconds.

In summary, THz-TDS was used to measure several of the FIR low- frequency torsional vibrational modes and their relaxational times of tryptophan. The dominated modes are at 1.435 THz for C11-C12 torsional motion and 1.842 *THz* for C1-C9 ring torsional motion. The broadband FIR absorption is due to a large density of low-frequency torsional modes with picosecond to subpicosecond relaxation lifetimes. The refractive index of tryptophan is determined to be n ~1.18 for film and 1.27 for powders in the 0.2–2.0 *THz* region. This work has important implications for

biomolecular dynamics in the fundamental physics of biomolecular low-frequency vibrations.

Summary

The inter/intra-molecular dynamics in liquid and gases have been studied through measurement of the absorption coefficient, index of refraction and dielectric function in the far-infrared region of the electromagnetic spectrum. These absorption modes are well described by using Terahertz Time-domain Spectroscopy (THz-TDS) based techniques. By using this technique through both conventional time-resolved THz generation methods (amplified Ti: Sapphire laser) and novel sources (mode-locked Erbium doped fiber laser) the low frequency modes in liquids (water and mixtures), gases (water, heavy water, methanol), and biological materials (tryptophan) were well characterized. The motivation for this work is to obtain a better understanding of the low-frequency modes in gases and liquids. This is important in biologically understanding the molecular structures. Below are a summary for important conclusions that have been reached for each of the materials stated in previous chapters:

Liquids

Using THz-TDS, the far-infrared absorption properties of liquid H_2O were measured. An absorption peak was observed at 1.56THz ($53 cm^{-1}$), which is attributed to the hydrogen bond bending motion in the liquid H_2O cage. The absorption and index of refraction curves are described by the Double Debye dielectric model to yield the low-frequency dielectric ($0.4 – 2.0 THz$) relaxation time of ~ $0.2 ps$ (fast) and ~ $9 ps$ (slow). The absorption due to large scale dynamics between molecules were further examined

using mixtures, where the absorption level from 0.5*M* KCl solutions is found to be above that from pure liquid water. This is due to the fact that both K^+ and Cl^- are considered to be strong "structure breakers". They affect the hydrogen bond network by breaking the bond to destroy the structure, making more "free" like water molecules available such that the absorption mode from the ring structures weaker or even disappear, while at the same time the absorption level increases. Our experimental result shows that the overall absorption level is higher than that from pure liquid water which agrees well with the "structure breaking" property of KCl as proposed in theory.

Gases

The rotational absorption modes in water vapor were measured in 0.2-2.2THz range, which are due to the pure rotation of water molecules at room temperature. The experimental results show that water molecules that undergo *ortho* level rotational transitions increase then decrease in absorption strength with increasing humidity, while most *para* transitions simply increase as expected for higher concentrations in the THz beam path. In terms of nuclear spin statistics, the *ortho* levels possess populations three times larger than the *para* levels at room temperature due to the presence of two symmetric hydrogen nuclei. Furthermore, *para-*H_2O adsorbs onto aluminum and silica surfaces preferentially due to its non-rotational ground state. The condensation of *para* molecules results in an abundance of *ortho-*H_2O. At higher humidity levels, *ortho* molecules are involved in interactions between neighboring

molecules more than *para* molecules. These interactions can be explained by dimerization and energy-coupling processes between dimers and monomers; however the dominant interaction that contributes to the decrease in absorption of *ortho* level transitions arises from interactions between molecules in the vapor phase which coalesce around liquid droplets either in the terahertz beam path or on surfaces.

Coherent transients for the methanol vapor and its isotopes are directly observed in the time domain THz pulse profile. These coherent transients arise from the excitation of an ensemble of coherent rotational levels via resonant absorption of THz pulse. These THz pulse spans the rotational levels for the asymmetric molecules. The emission from these excited rotational states form a sequence of pulses separated by inverse of rotational level, $\Delta\nu_R^{-1}$, from dephasing and rephasing of the ensemble of the excited rotational molecules in time. The signal amplitude of pulses decreases with relaxation time T_2 = 23 ± 0.5ps associated with dephasing of the ensemble of rotational levels. In addition, the duration of sequence pulses increases due to decoupling of rotational levels at time T_1 = 48 ± 0.5ps and centrifugal dephasing effects.

Biological Materials

Tryptophan is an amino acid and essential in human nutrition. THz-TDS was used to measure several of the FIR low- frequency torsional vibrational modes and the relaxational times of tryptophan. The dominated modes are at 1.435 THz for C11-C12

torsional motion and 1.842 THz for C1-C9 ring torsional motion. The broadband FIR absorption is due to a large density of low-frequency torsional modes with picosecond to subpicosecond relaxation lifetimes. The refractive index of tryptophan is determined to be n ~1.18 for film and 1.27 for powders in the 0.2–2.0 THz region.

Terahertz applications

Spanning a special frequency region in the Electromagnetic spectrum, the THz frequency is finding more and more applications in many areas such as chemistry, biology, medical industry, cosmetics industry, astronomy and even communications. Under decades of efforts from terahertz groups all over the world, it is coming to a new THz era! Some solid state terahertz sources (CW)[116] are more being used in THz applications. The following is a list of some currently exciting THz applications in industries and other area such as anti-terrorism.

The THz applications in the medical and pharmaceutical industries:

- Pharmaceutical analysis using THz spectroscopy: discriminate the polymorphs of the finished pharmaceutical product[117].
- Identify the counterfeit drugs using their spectral features in the THz range[118]
- Detect skin cancer using a reflection based THz-pulsed imaging system.[119]
- Tooth decay (caries) detection using the THz-pulsed imaging technique.[120]

The THz applications in cosmetics industry:

- Possible partnership with cosmetics manufactures: water has a lot of absorption modes in THz range. Most skin-care products such as moisturizers act to increase the retained water content of outmost layer of the skin to enhance its appearance. THz spectroscopy can then be used by the cosmetics industry to characterize and compare the effectiveness of their products by measuring the water content.

Other applications:

- Gas detection: to identify the constituents of the upper atmosphere using terahertz remote sensing from a satellite.[121]
- Anti-terrorism: detection of concealed weapon[122] and contraband.[123]

The work in this thesis is based on the following publications:

1. X. Xin, H. Altan, A. Saint, D. Matten, and R. R. Alfano, "Terahertz absorption spectrum of para and ortho water vapors at different humidities at room tmeperature", *J. Appl. Phys.* 100, 094905 (2005).

2. B. L. Yu, Y. Yang, F. Zeng, X. Xin, R. R. Alfano, "Reorientation of the H_2O cage studied by terahertz time-domain spectroscopy," *Applied Physics Letters 86, 061912 (2005).*

3. B. L. Yu, Y. Yang, F. Zeng, X. Xin, R. R. Alfano, "Terahertz absorption spectrum of D_2O vapor," *Optics Communications 258 (2006) 256-263.*

4. B. L. Yu, Y. Yang, F. Zeng, X. Xin, R. R. Alfano, "Direct observation of coherent rotational excitation, dephasing and depopulation of methanol and its isotopes using THz pulse radiation," *Applied Physics Letters 86, 101108 (2005).*

5. B. L. Yu, F. Zeng, Y. Yang, Q. Xing, A. Chechin, X. Xin, I. Zeylikovich, and R.R. Alfano, "Torsional vibrational modes of tryptophan studied by terahertz time-domain Spectroscopy,"*Biophysical Journal, Volume 86, March 2004, 1649-1654.*

References

[1] C. N. R. Rao, *Theory of hydrogen bonding in water*, in *Water A comprehensive treatise*, Vol. 1, Ed. F. Franks (Plenum Press, New York, 1972) pp. 93-114.

[2] N. Goldman, R. S. Fellers, C. Leforestier, R. J. Saykally, *J. Phys. Chem. A*, 105, 515 (2001).

3 L. Pauling, *The Nature of the Chemical Bond*, 2nd ed. (Cornell University Press, New York., 1948).

[4] G. E. Walrafen, *J. Chem. Phys.* 44, 1546 (1967).

[5] G. E. Walrafen, *J. Chem. Phys.* 47, 114 (1967).

[6] H. S. Frank, *Desalination Research Conference Proceedings*, *Nat. Acad. Sci., Nat. Res. Council Publ*. 942 (1963), p. 141.

[7] T. T. Waall and D. F. Hornig, *J. Chem. Phys.* 43. 2079 (1965).

[8] G. E. Walrafen, *J. Chem. Phys.* 48, 244 (1968).

[9] K.E. Larsson and U. Dahlborg, *Reactor Sci. Tech.* (*J. Nucl. Energy*) 16, 81 (1962)

[10] G. J. Safford, P. S. Leung, A.W. Naumann, and P.C. Schaffer, *J. Chem. Phys.* 50, 4444 (1969).

[11] B. L. Yu, Y. Yang, F. Zeng, X. Xin, R. R. Alfano, *Applied Physics Letters* 86, 061912 (2005).

[12] T. Jimbo, V. L. Caplan, Q. X. Li, Q. Z. Wang, P. P. Ho and R. R. Alfano, *Optics Letters,* Vol.12, No.7, 477 (1987).

[13] B.L. Yu, Y. Yang, F. Zeng, X. Xin, R. R. Alfano, *Optics Communications*, 258 (2006), 256-263.

[14] X. Xin, H. Altan, A. Saint, D. Matten, and R. R. Alfano, *J. Appl. Phys. 1*00, 094905 (2006).

[15] C. H. Townes, and A. L. Schawlow, *Microwave Spectroscopy*, Dover Publications, New York, p104 (1975).

[16] H. Mocker, R. Collins, *Appl. Phys. Lett.* 7, 270 (1965).

[17] C. Rullière (Ed.), *Springer-Verlag*, Berlin-Heidelberg, 1998.

[18] D. H. Auston, K. P. Cheung, J. A. Valdmanis, and D. A. Kleinman, *Phys. Rev. Lett.* 53, 1555 (1984).

[19] M. B. Ketchen, D. Grischkowsky, T. C. Chen, C-C. Chi, I. N. Duling, III, N. J. Halas, J-M. Halbout, J. A. Kash and G. P. Li, *Applied Physics Letters*, Vol.48, 751-753 (1986).

[20] B. B. Hu, X. -C. Zhang and D. H. Auston, *Phys. Rev. Lett.* 67, 2709 (1991).

[21] M. C. Nuss, P. M. Mankiewich, M. L. O' Malley, E. H. Westerwich, and P. B. Littlewood, *Phys. Rev. Lett* .66, 3305(1991).

[22] M. C. Nuss and J. Orenstein, *Millimeter and Submillimeter Wave Spectroscopy in Solids,* edited by G. Grüner (Topics in *Applied Physics;* v.74, Springer-Verlag, Berlin Heidelberg New York, 1998), pp. 7-109.

[23] D. M. Mittleman, R. H. Jakobsen, R. Needlamani, R. G. Baraniuk, and M. C. Nuss, *Appl. Phys. B* 67, 379(1998).

[24] R. A. Cheville and D. Grischkowsky, *J. Opt. Soc. Am. B* 16, 317 (1999).

[25] D. M. Mittleman, M. Gupta, R. Neelamani, R. G. Baraniuk, J.V. Rudd, M. Koch, *Appl. Phys. B* 68, 1085 (1999).

[26] B. L. Yu, F. Zeng, Q. Xing, and R. R. Alfano, *Applied Physics Letters*, 82(26), 4633(2003).

[27] B. L. Yu, F. Zeng, Y. Yang, Q. Xing, A. Chechin, X. Xin, I. Zeylikovich and R.R. Alfano, *Biophysical Journal* 86:1649-1654 (2004).

[28] B. L. Yu, Y. Yang, F. Zeng, X. Xin, R. R. Alfano, *Applied Physics Letters* 86,101108 (2005).

[29] H. Altan, Dissertation, *Characteristics of nanocomposites and semiconductor heterostructure wafers using THz spectroscopy*, Jan. 2005. *http://www.library.njit.edu/etd/2000s/2005/njit-etd2005-018/njit-etd2005-018.html*

[30] T. Shih, K. Reimann, M. Woerner, T. Elsaesser, I. Waldmüller, A. Knorr, R. Hey, and K. H. Ploog, *Phys. Rew.* 72, 195338 2005.

[31] J. T. Kindt and C. A. Schumttenmaer, *J. Phys. Chem.* 1996, 100, 10373-10379.

[32] Q. Chen and X. -C. Zhang, *Appl. Phys. Lett.*74, 3435 (1999).

[33] D. H. Auston, and M. C. Nuss, *IEEE J. Quantum Electron* 24, 184 (1988).

[34] P.Y. Han, M. Tani, F. Pan, X. -C. Zhang, *Opt. Lett.* 25, 675 (2000).

[35] Kai Liu, Jingzhou Xu , and X.-C. Zhang, *Applied Physics Letters*, **85**, 863 (2004).

[36] A Krotkus1, K Bertulis, Kai Liu, J Xu and X-C Zhang, *Semicond. Sci. Technol.* 19 (2004) S452–S453.

[37] B. B. Hu, X.-C. Zhang and D. H. Auston, *Phys. Rev. Lett.* **67**, 2709 (1991).

[38] Y. Cai, I. Brener, J. Lopata, J. Wynn, L. Pteitter and J. B. Stark, Q. Wu, and X. C. Zhang, J. F. Federici, *Appl. Phys. Lett.* Vol. 73, No. 4 (1998).

[39] M. Bass, P. A. Franken, J. F. Ward, and G. Weinreich, *Phys. Rev. Lett.* Vol.9, No.11, p. 446 (1962).

[40] Y. R. Shen, *The Principles of Nonlinear Optics,* p.67, John Wiley & Sons, 1984.

[41] P. Y. Han and X. -C Zhang, *Meas. Sci. Technol.* 12 (2001) 1747-1756.

[42] A. G. Stepanov, J. Hebling, J. Kuhl, *Appl. Phys. B* 81, 23-26 (2005).

[43] Nazarov M. M., Sapozhnikov D. A., Shkelnyuk S. A., Shuvaev A. V. and Shkurinov A.P., *THz Technology, Ultrafast Systems and Measurements,* P1.30, 359.

[44] Jacob B. Khurgin, *J. Opt. Soc. Am.B*, Vol. 11, No. 12, 2492(1994).

[45] P. P. Ho, R. R. Alfano, *Physical Review A,* Vol. 20, NO. 5, 2170 (1979).

[46] J. A. Valdmanis, G. A. Mourou, and C. W. Gabel, *IEEE J. Quant. El. QE*-19, 664 (1983).

[47] P. U. Jepsen, C. Winnewisser, M. Schall, V. Schyja, S. R. Keiding, and H. Heim, *Phys. Rev. E* 53, 3052 (1996).

[48] Q. Wu and X. -C. Zhang, *Appl. Phys. Lett.* 67, 3523 (1995).

[49] M. Brunken, H. Genz, P. Göttlicher, C. Hessler, M. Hüning, H. Loos, A. Richter, H. Schlarb, P. Schümser, S. Simrock, D. Suetterlin, M. Tonutti, D. Türke, *TESLA Report 2003-11*.

[50] B. E. A. Saleh and M. C. Teich, *Fundamentals of photonics*, by John Wilez & Sons, Inc., New York (1991).

[51] A. Yariv, *Optical electronics in Modern Communications*, Oxford University Press 1977.

[52] A. Rice, Y. Jin, X. F. Ma and X. -C. Zhang, D. Bliss, J. Larkin, M. Alexander, *Appl. Phys. Lett.* 64, 1324 (1994).

[53] A. Nahata, A. S. Weling, T. F. Heinz, *Appl. Phys. Lett.* 69, 2321 (1996).

[54] G. Gallot and D. Grischkowsky, *J. Opt. Soc. Am.* 16, 1204 (1999).

[55] J. R. Morris and Y. R. Shen, *Phys. Rev. A* 15, 1143 (1977).

[56] *Handbook of Chemistry and Physics,* Vol.74, edited by D.R. Lide (GRC Press, 1993-1994).

[57] NIELSEN, *Annu. Rep. Prog. Chem., Sec.* C90, 3(1993).

[58] NIELSEN, *Annu. Rep. Prog. Chem., Sec.* C93, 57(1996).

[59] S. Woutersen, U. Emmerichs, H. J. Bakker, *Science*, Vol. 278, 658 (1997).

[60] H.S. Frank, *Water A Comprehensive Treatise,* edited by Felix Franks, Vol.3, p211, by Ronald Ernest Verrall, Plenum Prses, New York-London, 1973.

[61] J. Barthel and R. Buchner, *Pure Appl. Chem.,* 63, 1473 (1991).

[62] J. Zhang and D. Grischkowsky, *Opt. Lett.* 29, 1031 (2004).

[63] C. Ronne, P. Astrand, and S. R. Keiding, *Phys. Rev. Lett*. 82, 2888 (1999).

[64] E. Pickwell, B. E. Cole, A. J. Fitzgerald, V. P. Wallace, and M. Pepper, *Appl. Phys. Lett.* p P84, 2190 (2004).

---

[65] G. E. Walrafen, *The Journal of Chemical Physics,* Vol.40, No.11 (1964).

[66] O. A. Simpson, B. L. Bean, and S. Perkowitz, *J. Opt. Soc. Am*. 69, 1723 (1979).

[67] J. B. Hasted, S. K. Husain, F. A. M. Frescura, and J. R. Birch, *Chem. Phys. Lett.* 118, (1985).

[68] G. E. Walrafen, *in Water: A Comprehensive Treatise*, edited by F. Franks (Pelnum, New York, 1972), Vol.1, p. 151.

[69] K. Liu, M. G. Brown, J. D. Cruzan, R. J. Saykally, *Science* 271 (1996) 62.

[70] Frank N. Keutsch & Richardd J. Saykally, *PNAS* 98 (2001) 10533.

[71] K. N. Woods, H. Wiedemann, *Chem.Phys.Lett.* 393 (2004) 159-165.

[72] G. R. Choppin and K. Buijis, *J. Chem. Phys.* 39, 2042 (1963).

[73] D. A. Draegert, D. Williams, *J. Chem. Phys.* 48, 401 (1968).

[74] H. S. Frank and M.W. Evans, *J. Chem. Phys.* 13, 507(1945).

[75] H. S. Frank and W. Y. Wen, *Disc. Faraday Soc.* 24, 133 (1957).

[76] F. Franks, *Water: A Comprehensive Treatise*, Vol.3 "*Aqueous solutions of simple electrolytes*", - Ronald Ernest Verrall, page226, Plenum Press, New York-London, 1973.

[77] D. Hadži and S. Bratos, in *Hydrogen Bond*, (Elsevier, Amsterdam, 1976), Vol.2, Chap.12.

[78] V. I. Tikhonov and A. A. Volkov, *Science* 296, 2363 (2002).

[79] S. Maruyama, S. Matsumoto, A. Ogita, *Ther. Sci. & Eng.* 2, 1 (1994).

[80] T. Oka, *Adv. At. Mol. Phys.* 9, 127 (1973).

[81] S. A. Potekhin, and R. S. Khusainova, *Biophys. Chem.* 118, 84 (2005).

[82] J. M. Calo, *J. of Chem. Phys.* 62, 4904 (1975).

[83] L. B. Braly, K. Liu, M. G. Brown, F. N. Keutsch, R. S. Fellers, R. J. Saykally, *J. of Chem. Phys.* 112, 10314 (2000).

[84] L. B. Braly, J. D. Cruzan, K. Liu, R. S. Fellers, R. J. Saykally, *J. of Chem. Phys.* 112, 10293 (2000).

[85] K. Pfeilsticker, A. Lotter, C. Peters, H. Bösch, *Science* 300, 2078 (2003).

[86] L. A. Curtiss, D. J. Frurip, M. Blander, *Chem.l Phys. Lett.* 54, 575 (1978).

[87] N. Goldman, C. Leforestier, R. J. Saykally, *J. Phys. Chem. A,* 108, 787 (2004).

[88] J. R. Reimers and R. O. Watts, *Chem. Phys.* 85, 83 (1984).

[89] H. Zaghloul and H. A. Buckmaster, *J. Phys. D* ***18*** (1985) 2109-2118.

[90] G. S. Kell, *J. Chem. Eng. Data* **12** (1967) 66-69.

[91] F. Franks (Ed.), *Water: A comprehensive treatise*, Plenum Press, New York, 1972-1981, Vols. 1-7.

[92] G. Herzberg, *Molecular Spectra and Molecular Structure: II Infrared and Raman Spectra*, Van Nostrantd, Princeton, N. J., 1945.

[93] P. S. Ormsby, K. Narahari Rao, M. Winnewisser, B. P. Winnewisser, O. V. Naumenko, A. D. Bykov, and L. N. Sinitsa, *J. Mol. Spectrosc.* 180(1993) 109 –130.

[94] R. A. Toth, *J. Mol. Spectrosc*. 195 (1999) 98-122.

[95] C. C. Amy-Peypet, J. M. Flaud, A. Mahmoudi, G. Guelachvili, and J. W. C. Johns, *Int. Infrared Millimeter Waves* 6 (1985) 199.

[96] J. M. Flaud, C. C. Amy-Peyret, and R. A. Toth, *Water vapor line parameters from microwave to medium infrared,* Vol. 19 of *International Table of Selected Constants*, Pergamon, Oxford, 1981.

[97] H. M. Pickett, R. L. Poynter, and E. A. Cohen, *Submillimeter, Millimeter, and Microwave Spectral Line Catalog,* accessed via World Wide Web (http:// spec.jpl.nasa.gov) from the Jet Propulsion Laboratory, Pasadena, California.

[98] R. Gamache and L. Sothman, *J. Mol. Spectrosc.* 128 (1998) 360-369.

[99] N. A. Kurnit, I. D. Abella, and S. R. Hartman, *Phys. Rev. Lett.* 13, 567 (1964).

[100] N. Bloembergen, *Nonlinear Optics* (W. A. Benjamin, Inc., New York, 1965).

[101] H. Harde, S. Keiding, and D. Grischkowsky, *Phys. Rev. lett.* 66, 1834 (1991); *J. Opt. Soc. Am B* 11, 1018 (1994).

[102] G. Moruzzi, Brenda P. Winnewisser, M. Winnewisser, I. Mukhopadhyay, and F. Strumia, *Microwave, Infrared and Laser Transitions of Methanol* (CRC Press, New York, 1995). A complete list 1680 transitions can be found in Table 9.1. These transitions needed for coupling are not apparent from the numerous transitions presented in this table. The observed transitions in the spectral region connect the rotational levels within the ground vibrational state for CH_3OH, CH_3OD, and CD_3OD molecules. The transitions in the microwave region are those for which, (1)$\Delta J = \pm 1$, $\Delta K\pm=0$ $\Delta n=0$; (2) $\Delta J=0$, $\Delta K\pm= \pm 1$, $\Delta n=0$; and (3) $\Delta J= \pm 1$,$\Delta K\pm= \pm 1$, $\Delta n=0$. Many of these transitions occur in the microwave spectrum which overlaps over THz pulse spectrum (0.2–2.2 THz) for CH_3OH, CH_3OD, and CD_3OD gases. The transitions between two separate rotational are leveled sequences labeled by the quantum numbers (J"K"$\pm$ n")$\leftrightarrow$($J'K'\pm$ n'). For example, for CH_3OH, the transition frequencies for (12 1 0)$\leftrightarrow$(11 1 0) and (11 1 0)$\leftrightarrow$(10 1 0) are 0.5848 and 0.5362 THz, respectively. The frequency separation between adjacent lines is 0.0486 THz, which corresponds to the inverse time spacing ~21ps. [$\Delta J= \pm 1$ transitions occur from J'=11 to 2$\leftrightarrow J''$=12 to 3 for $K'=K''$=1; J'=11 to 5$\leftrightarrow J''$=12 to 6 for K'=6 and K''=5; and J'=10 to 4$\leftrightarrow J''$=11 to 5 for K''=5 and K' =4, all have inverse time spacing of 21ps.] For CH_3OD, the transition frequencies for (0,0+,0)$\rightarrow$(1,0+,0) and (1,0+,0)$\rightarrow$(2,0+,0) are 0.0454 and 0.0907 THz, respectively. The frequency separation between adjacent lines is 0.0453 THz which corresponds to the inverse time spacing ,22ps. [$\Delta J= \pm 1$ transitions occur in J''=8 to 0$\leftrightarrow J'$=9 to 0 for $K''=K'$ =0; J''=8 to 1$\leftrightarrow J'$=9 to 2 for $K''=K'$=1+; J''=8 to 2$\leftrightarrow j''$=9 to 3 for $K''=K'$=2+; and J''=8 to 3$\leftrightarrow J'$=9 to 4 for $K''=K'$=3+, all have inverse time spacing of 22ps.] For CD_3OD, the transition frequencies for (0,0,0) $\rightarrow$(1,0,0) and (1,0,0) $\rightarrow$(2,0,0) are 0.0385 and 0.0.0769 THz, respectively. The frequency separation between adjacent lines is 0.0384 THz which corresponds to the inverse time spacing ~26ps. [$\Delta J = \pm 1$ transitions occur for J'=4 to 0$\leftrightarrow J''$=5 to 1 for $K'=K''$=0, all have inverse time spacing of 26ps.]

[103] Y. –B. Duan, I. Ozier, S. Tsunekawa, and K. Takagi, *J. Molecular Spectroscopy,* 218, 95 (2003). Table 2 lists transitions for CH_3OD.

[104] R. M. Lees, *J. Chem. Phys***.** 56, 5887 (1972). Table IV lists transitions for CD_3OD.

[105] Austin, R. H., M. K. Hong, C. Moser, and J. Plombon. 1991. *Chem. Phys*, 158:473–486.

[106] Austin, R., M. Roberson, and P. Mansky. 1989. *Phys. Rev. Lett.* 62:1912– 1915.

[107] Beratan, D. N., J. N. Betts, and J. N. Onuchic. 1992. *J. Phys. Chem.* 96:2852–2855.

[108] Markelz, A. G., A. Roitberg, and E. J. Heilweil. 2000. *Chem. Phys. Lett.* 320:42–48.

[109] Brucherseifer, M., M. Nagel, P. Haring, H. Kurz, A. Bosserhoff, and R.Buttner. 2000. *Appl. Phys. Lett.* 77:4049–4051.

[110] Walther, M., B. Fischer, M. Schall, H. Helm, and P. Jepsen. 2000. *Chem. Phys. Lett.* 332:389–395.

[111] Born, M., and E. Wolf. 1987. *Principles of Optics.* Pergamon, Oxford.

[112] Duvillaret, L., F. Garet, and J. L. Coutaz. 1996. *EEE J. Selected Topics in Quantum Electroni*cs 2:739–746.

[113] Xie, A., A. F. van der Meer, and R. H. Austin. 2002. *Phys. Rev. Lett.* 88:018102–018104.

[114] Moeller, K., and W. G. Rothschild. 1971. *Far-Infrared Spectroscopy,* Wiley, New York. 557–591.

[115] Frisch, M. J., G. W. Trucks, H. B. Schlegel, P. M. Gill, G. Johnson, M. A.Robb, J. R. Cheeseman, T. Keith, G. A. Petersson, J. A. Montgomery, K.Raghavachari, M. A. Al-Laham, V. G. Zakrzewski, J. V. Ortiz, J. B. Foresman, C. Y. Peng, P. Y. Ayala, W. Chen, M. W. Wong, J. L. Andres, E. S. Replogle, R. Gomperts, R. L. Martin, D. J. Fox, J. S. Binkley, D. J. Defrees, J. Baker, J. P. Stewart, M. Head-Gordon, C. Gonzalesz, and J. A. Pople. 1995. *Gaussian 94*, *Revision B.2*. Gaussian, Inc., Pittsburgh, PA.

[116] Thomas W. Crowe, William L. Bishop, David W. Porterfield, Jeffrey L. Hesler, and Robert M. Weikle , *IEEE JOURNAL OF SOLID-STATE CIRCUITS*, VOL. 40, NO. 10, OCTOBER 2005

[117] *TPI Spectra* 1000, AF#502E: http://www.brukeroptics.com/terahertz/index.html retrieved on Jan. 24th, 2007.

[118] TeraView Press releases: http://www.cambridgenetwork.co.uk/pooled/articles/BF_NEWSART/view.asp?Q=BF_NEWSART_227537#http://www.teraview.com, retrieved on Jan. 24th, 2007.

[119] Woodward, R.M., V.P. Wallace, R.J. Pye, et al. 2002. "Terahertz pulse imaging in reflection geometry of skin using time domain analysis techniques." *Proc. SPIE 4625*:160-169.

[120] Ciesla, C.M., D.D. Arnone, A. Corchia, et al. 2000. "Biomedical applications of Terahertz pulse imaging." *Proc. SPIE 3934*:73-81.

[121] J. R.Wang, P. Racette, J. D. Spinhime, K. F. Evans, andW. D. Hart, "Observations of cirrus clouds with airborne MIR, CLS, and MAS during SUCCESS," *Geophys. Res. Lett.*, vol. 25, pp. 1145–1148, 1998.

[122] J. C. Dickinson, T. M. Goyette, and J. Waldman, "High resolution imaging using 325 GHz and 1.5 THz transceivers," presented at *the 15th Int. Symp. Space Terahertz Technology, Northampton, MA,* 2004.

[123] Y. Ogawa, K. Kawase, M. Yamashita, and H. Inoue, "Non-destructive inspection techniques for illicit drugs using terahertz imaging," in *Proc.Conf. Lasers and Electro-Optics*, vol. 1, May 2004, p. 3.

Autobiographical Statement

Author: Xuying Xin

Degree: Doctor of Philosophy

Date: January 2007

Educations:

- Doctor of Philosophy in Electrical Engineering,

  The Graduate School and University Center of the City University of New York, *New York, NY,* 2007.

- Master of Philosophy in Engineering (Electrical Engineering)

  The Graduate School and University Center of the City University of New York, *New York, NY,* 2005.

- Bachelor Degree in Opto-electric Engineering, Chongqing University, Chongqing, Sichuan, China, 1999.

Publications:

- X. Xin, H. Altan, A. Saint, D. Matten, and R. R. Alfano, "Terahertz absorption spectrum of para and ortho water vapors at different humidities at room tmeperature", *J. Appl. Phys. 100, 094905 (2005)*

- H. Altan, X. Xin, D. Matten and R. R. Alfano, "Direct observation of the strength of plasmon-longitudinal optical phonon interaction in n-type GaAs", *Appl. Phys. Lett.*, 89, 052110(2006).

- B. L. Yu, Y. Yang, F. Zeng, X. Xin, R. R. Alfano, "Reorientation of the H_2O cage studied by terahertz time-domain spectroscopy," *Applied Physics Letters 86, 061912 (2005).*

- B. L. Yu, Y. Yang, F. Zeng, X. Xin, R. R. Alfano, "Terahertz absorption spectrum of D_2O vapor," *Optics Communications 258 (2006) 256-263.*

- B. L. Yu, Y.Yang, F. Zeng, X. Xin, R. R. Alfano, "Direct observation of coherent rotational excitation, dephasing and depopulation of methanol and its isotopes using THz pulse radiation," *Applied Physics Letters 86, 101108 (2005).*

- B. L. Yu, F. Zeng, Y.Yang, Q. Xing, A. Chechin, X. Xin, I. Zeylikovich, and R. R. Alfano, "Torsional vibrational modes of tryptophan studied by terahertz time-domain Spectroscopy," *Biophysical Journal, Volume 86, March 2004, 1649-1654.*